POLITECNICO DI MILANO

School of Industrial and Information Engineering
Master of Science in Electrical Engineering – Smart Grid

ANALYSIS AND CONTROL OF THREE-PHASE INVERTERS FEEDING UNBALANCED LOADS

Supervisor: Prof. Roberto Perini

Master of Science Thesis by:
Gianvito Francesco Nettis
Matr. 876782

Academic Year 2017-2018

Acknowledgments

I want to express my sincerest gratitude to my supervisor Professor Roberto Perini, for his continuous support during the last year of study and research, for his helpfulness and patience, and for always encouraging me to work better and harder whenever difficulties came out.

Thanks to Politecnico di Milano for letting me experience this university path and for giving me the possibility to grow up in an international context. Every moment spent in this university has been fundamental for the good progress of my studies.

Abstract

Nowadays microgrids are spreading more and more around territory, promoting the development of the distributed generation and the integration of RES with the existing distribution grid, towards a more sustainable future that aims at the reduction of CO_2 emissions, in favour of renewable energy sources and the so-called Smart Grids.

Among the critical issues about the generation by RES there is the use of interface static converters for the connection to the microgrid, which often need the implementation of specific control techniques to guarantee the regulation and the stability of the grid itself; in particular, the unbalance of loads, which is quite common in microgrids, has a negative impact on the entire system.

In this thesis work the analysis and control of three-phase inverters feeding unbalanced loads is presented.
One of the solutions studied for this kind of problem considers the use of a particular interface three-phase inverter, where an additional leg gives the connection point for the load's neutral point through the neutral conductor.

Two kinds of configuration are analysed: the first one considers the use of two series capacitors on the fourth leg, guaranteeing the stabilization of the nominal voltage across the load; the second one is characterized by a fourth leg identical to the others, which gives the controllability of the load's neutral point, bringing the system to balanced conditions.
The analysis about the former converter's topology is focused on the evaluation of the improvement given by inserting an inductance on the neutral conductor,

giving as result a symmetric and balanced load voltage system. The latter one concentrates on the inverter's control scheme and modulation technique, analysing two different PI regulators design methods.

The first modelling method is based on the traditional designing techniques for SISO systems; the search for a better system response has brought to a different view of the system itself, employing more complex design methods for MIMO systems. The analysis criterion has not completely given the desired results, laying foundations and questions for possible future developments.

Sintesi

Al giorno d'oggi le microreti stanno trovando sempre più diffusione sul territorio, favorendo la crescita della generazione distribuita e l'integrazione delle FER con la rete di distribuzione esistente, verso un futuro più sostenibile che punti alla riduzione delle emissioni di CO_2, a favore delle fonti energetiche rinnovabili e delle cosiddette Smart Grids.

Tra le criticità riguardanti la generazione da FER vi è l'impiego di convertitori statici di interfaccia con la microrete, che spesso richiedono lo sviluppo di specifiche tecniche di controllo per garantire la regolazione e la stabilità della rete stessa; in particolare, lo squilibrio dei carichi, che è abbastanza comune nelle microreti, ha un impatto negativo sull'intero sistema.

In questo lavoro di tesi viene presentata l'analisi e il controllo di inverter trifase che alimentano carichi squilibrati.
Una delle soluzioni pensata per questo tipo di problema prevede l'utilizzo di un particolare inverter trifase di interfaccia, dove vi è un quarto ramo addizionale che garantisce il punto di connessione del centro stella del carico attraverso il conduttore di neutro.

Si analizzano due tipi di configurazione: la prima soluzione prevede l'utilizzo di due condensatori in serie sul quarto ramo, garantendo la stabilizzazione della tensione nominale al carico; la seconda è caratterizzata da una quarta gamba identica alle altre tre, che permette il controllo del centro stella del carico, portando il sistema in condizioni bilanciate.
L'analisi della prima tipologia di convertitore è focalizzata sulla valutazione del miglioramento dato dall'inserzione di un'induttanza sul conduttore di neutro,

dando come risultato un sistema di tensioni al carico simmetrico ed equilibrato. La seconda si concentra sullo schema di controllo e la tecnica di modulazione dell'inverter, analizzando due diversi metodi per il dimensionamento dei regolatori PI.

Il primo metodo è basato sulle tradizionali tecniche di dimensionamento per sistemi SISO; la ricerca di una migliore risposta da parte del sistema ha portato a una valutazione differente del sistema stesso, adoperando tecniche di dimensionamento più complesse per sistemi MIMO. Il criterio di analisi non ha portato completamente ai risultati desiderati, ponendo le basi e gli interrogativi per possibili sviluppi futuri.

Contents

List of Figures

List of Tables

List of Acronyms

RES	Renewable Energy Source
FER	Fonte Energetica Rinnovabile
VSI	Voltage Source Inverter
PWM	Pulse Width Modulation
PV	Photovoltaic
PI	Proportional Integral
LPF	Low-Pass Filter
SCC	Symmetrical Component Calculator
SOGI	Second Order Generalized Integrator
FAE	Fictive Axis Emulation
SISO	Single Input Single Output
MIMO	Multiple Input Multiple Output
VUF	Voltage Unbalance Factor
DG	Distributed Generator

INTRODUCTION
STATE OF THE ART

The unbalance of loads in electrical grids is a case that occurs very frequently, due to the randomness that characterizes the connection and disconnection of users' equipment and devices. Therefore, there is a huge list of possible load configurations in the grid. The problem that arises from this situation is the consequent unbalance of the supplying voltages, which deviate from the nominal values damaging the connected loads themselves.

Microgrids are usually based on diesel power plants, since their technology is independent of the weather conditions, differently from RESs (Renewable Energy Sources). In such systems, the use of renewable energy sources and energy storage units can decrease the cost and environmental impact of electricity production. In the ideal scenario all diesel generators would be turned off, requiring a battery inverter to supply the grid, balancing active and reactive power. In this case the RESs would operate at their maximum power point [1].

Generally, electrical distribution systems include the neutral conductor, allowing loads and RESs to be connected either line-to-line or line-to-neutral, depending on their number of phases and power ratings.

Loads and sources in extended grids, like distribution ones, are usually arranged in order to result in a balanced configuration across the three phases, and in any case, since they are large in number, any unbalance results to be

very slight and easily manageable. On the other hand, in microgrids with a relatively small number of loads the unbalance is very common, leading to unequal voltage drops on the output filter of the interface inverter and unbalanced output voltages. This can result in increased losses as well as bad operating conditions of devices across the grid.
For these reasons, microgrids need that the interface inverter presents a suitable control scheme to supply balanced voltages to an unbalanced grid and with a fast-transient response to load variations.
There are different topologies of voltage source inverter (VSI) and solutions suitable to operate in three-phase four-wire systems:

- **The three-phase four-wire inverter with a split DC link capacitor** [2,3], it is the simplest configuration, which guarantees the voltage balancing through a capacitor divider connected to the neutral conductor;
- **The three-phase inverter with a Δ-Y transformer** [4-6], in which the zero-sequence current component would be forced to circulate in the Δ winding, and the control circuit of the inverter would only have to compensate for the voltage drops of the positive and negative sequence currents on the output filter of the inverter. However, the zero sequence currents will produce voltage drops in the Y-side of the transformer which the three-leg inverter cannot compensate [7];
- **The zig-zag winding** [8], which creates an accessible and stable neutral point;
- **The three-phase four-leg inverter**, which would provide the required means for the voltage balancing by controlling the neutral point through the 4^{th} leg [1], employing a carrier-based PWM modulation technique [9].

The first and the last topologies are investigated in this study.

CHAPTER 1
THREE-PHASE FOUR-WIRE INVERTER CONFIGURATION

In this chapter, unbalanced loads problem is managed through a **three-phase four-wire inverter**. The solution investigated is presented in theory, providing also a numerical example that will be tested in the chapter dedicated to simulations.

1.1 Physical System

The system in analysis is a three-phase four-wire hybrid stand-alone power system mainly supplied by a photovoltaic (PV) generator interfaced through a three-phase inverter with an additional leg constituted by two series capacitors, called **three-phase four-wire inverter**, which is a particular topology of voltage source inverter (VSI). This grid is characterized by highly unbalanced loads, which is a very common situation in such a power system.

Figure 1.1 represents the simplified scheme of the system, where the PV generator is modelled as a DC voltage source.

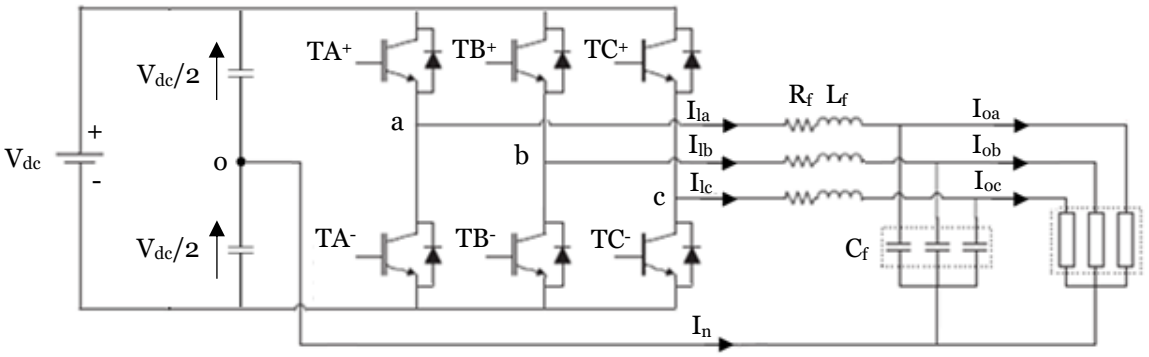

Figure 1.1 – Schematic diagram of the physical system

The inverter presents an **LC output filter**. Its use is effective to face harmonics problem coming out of the inverter output.

Finally, the neutral point of the unbalanced loads is connected to the midpoint of the voltage source's capacitor divider (node *o*) through the neutral conductor. According to the Ohm's law, in case of unbalanced loads:

$$\bar{I}_{oa} + \bar{I}_{ob} + \bar{I}_{oc} \neq 0 \tag{1.1}$$

1.1.1 Four-wire Inverter

Let's consider the case in which the three-phase inverter feeds a star connected three-phase **unbalanced load** with accessible neutral terminal. Due to the imbalance, the phase currents are not balanced so, if a transformer is not available, a connection to the neutral terminal should be provided by adding an extra wire to the inverter.

The loads neutral terminal can be connected to the inverter through two different topologies of scheme. The first is a **three-phase four-wire** topology (Figure 1.1), in which the neutral point is connected directly to the midpoint of the voltage sources by means of a capacitor divider. The other one will be discussed in the following chapter.

The three-phase four-wire configuration is the simplest solution, and in this case the three-phase inverter can be turned into three independent single-phase converters. Each load would be alternatively supplied by the voltages

$V_{dc}/2$ and $-V_{dc}/2$, becoming the entire system perfectly balanced. Despite this, there is a drawback that cannot be neglected, which is explained below.

Figure 1.2 shows the single-phase representation of one of the system's phases, which can be extended for the others. When the upper switch TA^+ is ON, the circuit is:

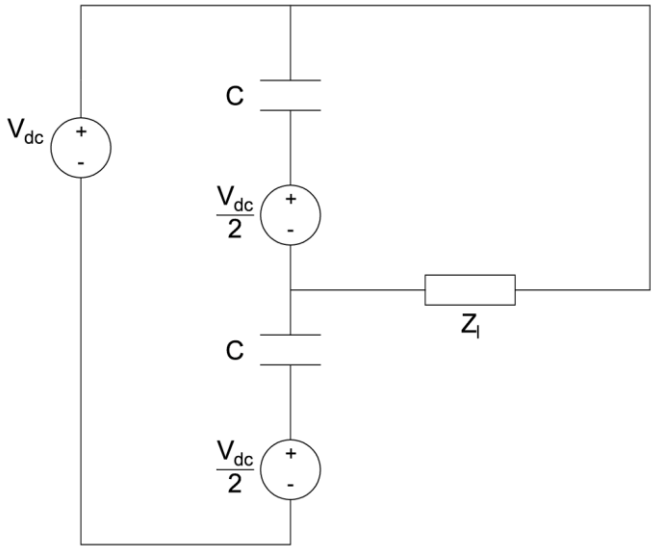

Figure 1.2 – Single-phase circuit representation (a)

where Z_l is the single-phase load, which usually is ohmic-inductive. The two capacitors are in parallel, therefore the scheme becomes:

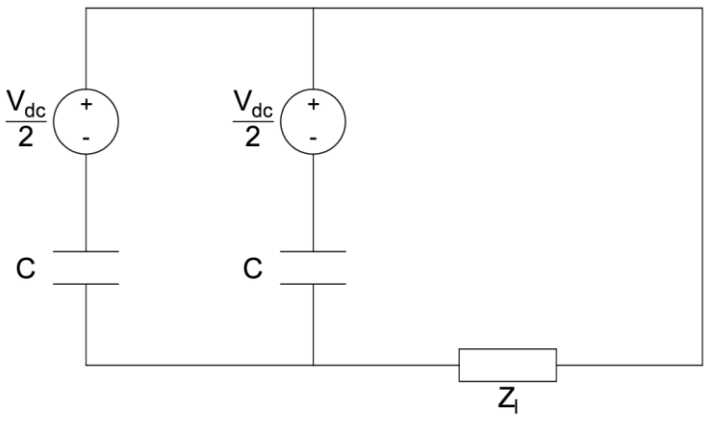

Figure 1.3 – Single-phase circuit representation (b)

and simplifying more:

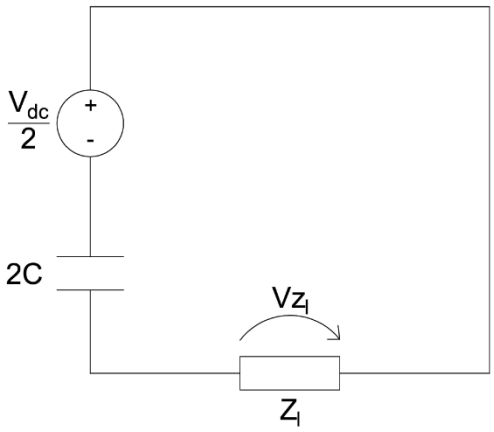

Figure 1.4 – Single-phase circuit representation (c)

The limitation of this topology is represented by the fact that the voltage drop across capacitors causes a reduction of the supply voltage V_{Z_l} across the loads. Reducing the capacitive impedance by using big capacitors would limit the voltage drop, but this solution is not cost-effective.

From electric power systems theory, the measure adopted to limit the inductive reactance on overhead lines is to use series capacitors, so that their associated reactance, which is negative, is subtracted to the lines' ones themselves [10]; using the same concept, the idea is to insert an inductance on the neutral conductor, which has the role to compensate the capacitive impedance, and making loads supplied by their nominal voltage.

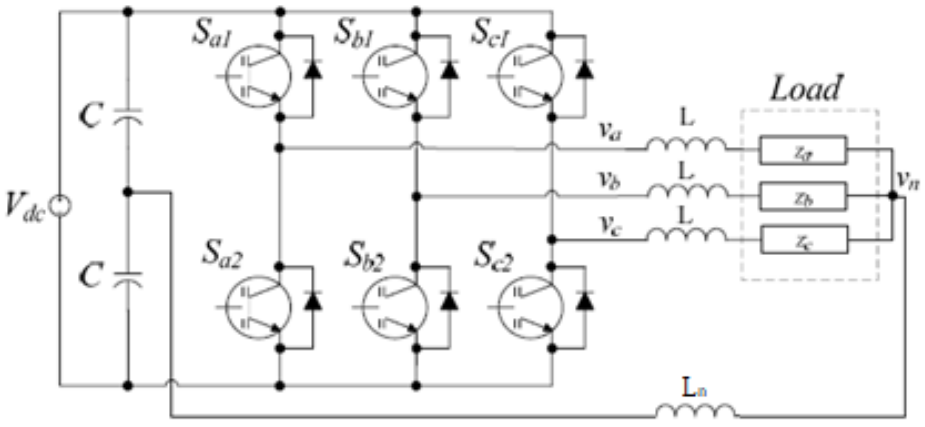

Figure 1.5 – Three-phase four-wire inverter with neutral inductance

The single-phase circuit becomes:

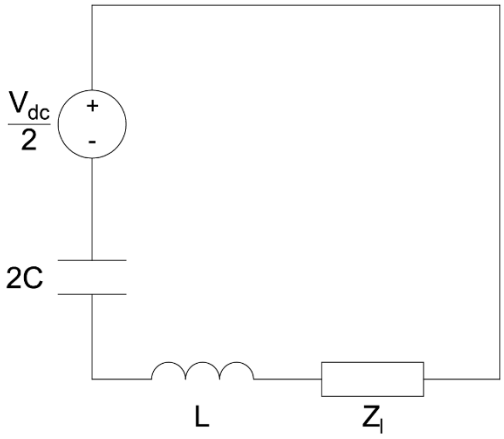

Figure 1.6 – Single-phase circuit representation (d)

Thanks to the inductor, the load Z_l is supplied by a voltage $V_{Z_l} = V_{dc}/2$.
The disadvantage of this solution is that the circuit could reach a resonance condition, which would cause the rise of overvoltages across the capacitive impedances damaging their insulation.

In Figure 1.7 the circuit configuration when the switch TA^- is ON is shown:

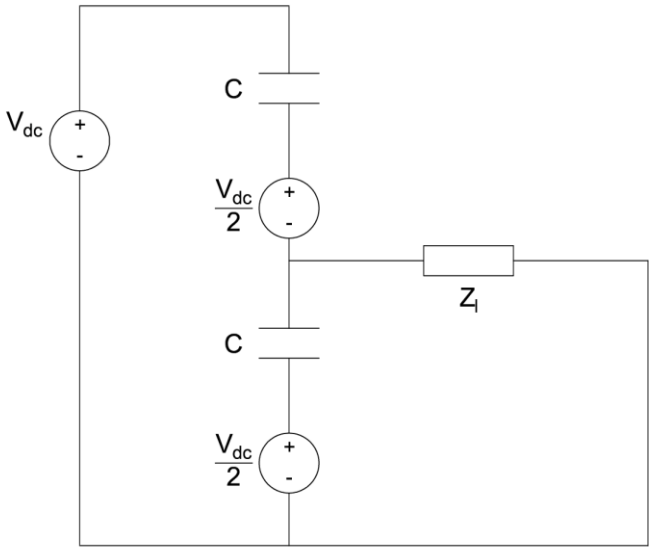

Figure 1.7 – Single-phase circuit representation (e)

Doing the same simplification described before:

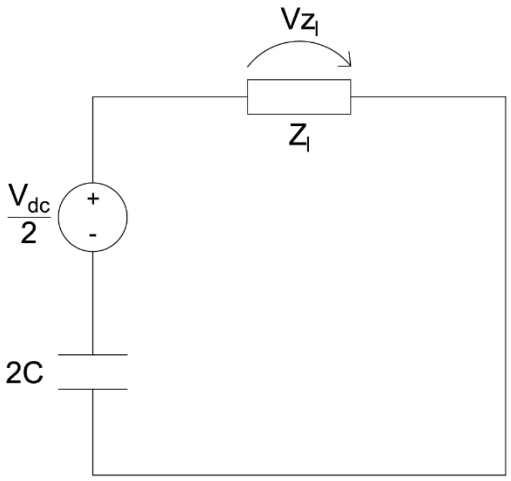

Figure 1.8 – Single-phase circuit representation (f)

Therefore, inserting the neutral inductor, the voltage across the load will be $V_{Z_l} = -V_{dc}/2$.

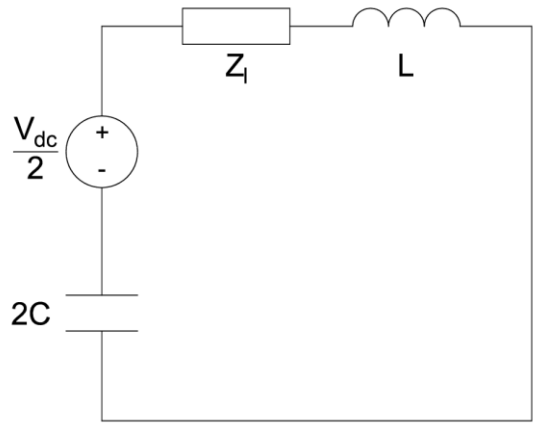

Figure 1.9 – Single-phase circuit representation (g)

1.1.2 Implemented system

Table 1.1 and the following computations summarize the choices for the design of the main elements of physical system:

Table 1.1 – Main system's input data

DC Bus voltage V_{DC}	400 V
Fourth leg's capacitors C_d	1 mF
Filter's inductance L_f	25 mH
Filter's resistance R_f	36.7 mΩ
Active power absorbed by each load P_l	2.7 kW
Load power factor cos φ	0.93
Rated AC side angular frequency ω_n	2π*50 rad/s

Active power and power factor are referred to the hypothetical condition of balanced load. In Chapter 4 the unbalanced load status will be introduced.

The correspondent load resistance and inductance are:

$R_l = 6.3\ \Omega$

$L_l = \ 10.4\ mH$

The neutral inductor L_n is dimensioned by compensating totally the capacitive reactance X_C as it follows:

$$X_C = X_L \tag{1.2}$$

Therefore:

$$\frac{1}{\omega_n 2C_d} = \omega_n L_n \tag{1.3}$$

The inductance is:

$$L_n = \frac{1}{{\omega_n}^2 2C_d} \approx 5\ mH \tag{1.4}$$

As it will be possible to see in simulation, the neutral wire in unbalanced load condition sustains a rms value of neutral current around 10 A.

The configuration described in this section is focused on the physical aspects of the solution proposed, verifying that the insertion of an inductance on the neutral conductor would improve the result that does not consider such a solution, making the three load voltages closer to a symmetric and balanced system.

Voltages and currents of the system are not involved in any kind of control; besides, the modulation technique adopted for the converter is a traditional PWM characterized by ideal carrier signals.

CHAPTER 2
THREE-PHASE FOUR-LEG INVERTER CONFIGURATION

In this chapter, the solution for the unbalanced loads is solved through a **three-phase four-leg inverter**. An overview of the physical system is given, and all the analytical relationships that connect the real world with the mathematics are described in detail. Then, the focus is centralized on the control scheme adopted and on the inverter's modulation technique.

2.1 Physical System

The system analyzed in this chapter is identical to the one of Chapter 1, apart from the converter topology: it is a three-phase inverter with an extra leg, properly named **three-phase four-leg inverter**. As in previous chapter, the grid is characterized by the presence of unbalanced loads.

In Figure 2.1 the scheme of the system is depicted. Note that the fourth-leg here is composed by two additional power switches, identically to the other three inverter's leg.

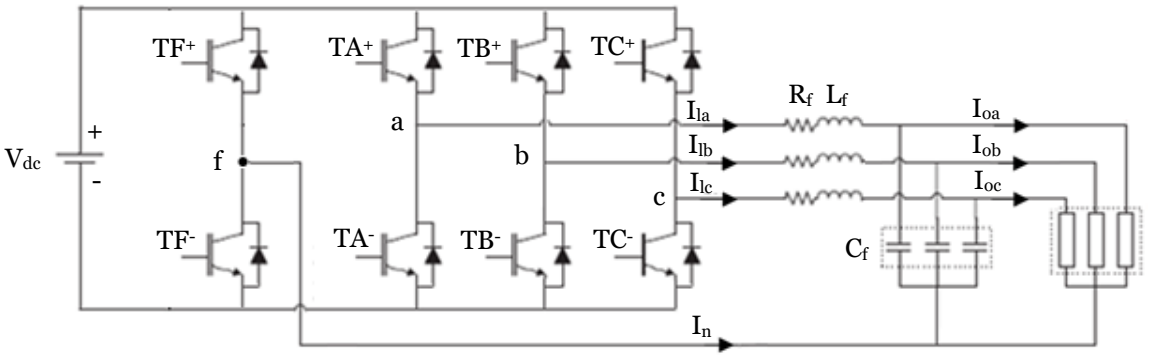

Figure 2.1 – Schematic diagram of the physical system

The neutral point of the unbalanced loads is connected to the 4th leg (node *f*) of the converter through the neutral conductor.

2.1.1 Four-leg Inverter

As already said, the converter used in this case is a **three-phase four-leg inverter** (Figure 2.2), adding a fourth leg to the inverter that permits to control the neutral point voltage.

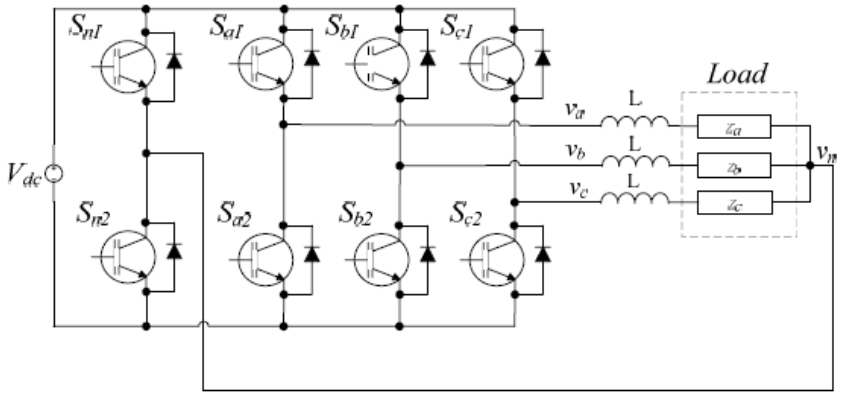

Figure 2.2 – Three-phase four-leg inverter

This configuration requires two additional power switches and a more complex control strategy, but it offers different advantages, among which the possibility of the **neutral point voltage control** [11].

2.1.2 Implemented system

The dissertation will be developed in parallel to a numerical example. An inverter, characterized by the following nominal data, is introduced:

Table 2.1 – Inverter's nominal input data

Rated Voltage (rms) V_{ph}	230 V
Rated Voltage (line-to-line) V_n	400 V
Rated power A_n	10 kVA

The output inverter's LC filter is designed starting from the input data below:

Table 2.2 – Filter's characterization input data

Max admissible voltage drop across filter's inductances ΔV_{Lf}	2% V_{ph}
Reactive power associated to filter's capacitances Q_C	5% A_n
Quality factor associated to filter's inductances Q	20 ÷ 100

The apparent power can be written as:

$$A_n = 3\, V_{ph} I_{ph} \tag{2.1}$$

Therefore:

$$I_{ph} = \frac{A_n}{3V_{ph}} \approx 14.5\ A \tag{2.2}$$

Where I_{ph} is the nominal inverter's phase-current.

The voltage drop across filter's inductance is:

$$\Delta V_{Lf} \approx Z_{Lf} I_{ph} \approx X_{Lf} I_{ph} \tag{2.3}$$

Therefore:

$$X_{Lf} \approx \frac{\Delta V_{Lf}}{I_{ph}} \approx 317\ m\Omega \tag{2.4}$$

The inductance is:

$$L_f = \frac{X_{Lf}}{\omega_n} \approx 1\ mH \tag{2.5}$$

And assuming $Q = 20$, the internal resistance is:

$$R_f = \frac{\omega_n L_f}{Q} \approx 15\ m\Omega \tag{2.6}$$

And the capacitance is:

$$C_f = \frac{Q_C}{2\pi f_n * {V_n}^2} \approx 10\ \mu F \tag{2.7}$$

Its series resistance is:

$$R_d = \frac{1}{3}\frac{1}{C_f\ \omega_{sw}} \approx 0.53\ \Omega \tag{2.8}$$

Where $f_{sw} = {\omega_{sw}}/{2\pi} = 10\ kHz$ is the inverter switching frequency.

2.2 Control System

The control system is the necessary mechanism adopted in order to make the electrical quantities, voltage and current, equal to the desired values that guarantee the correct and desired operation of the system.

2.2.1 Overview

The control scheme for balancing the output voltages of the four-leg inverter operating with unbalanced loads has to be chosen among a wide range of possibilities. Most are based on *dq* control, frequently employed in three-phase inverters: by converting AC into DC quantities, simple **PI controllers** can be used to obtain zero error in steady state condition and fast transient response. However, due to the unbalance, the quantities in the rotating *dq* frame are not pure DC anymore, because they contain a double line frequency component

due to the negative sequence components and a line frequency component due to the zero sequence components. These leads to non-zero steady-state errors when present at the output of the PI controllers [1].
This problem can be solved by employing a **Low-Pass Filter (LPF)**, but it introduces delays and slows down the dynamic response of the system.
Another approach consists of firstly obtaining the symmetrical components of the unbalanced signals and then applying the *abc* - *dq* transformation to obtain *dq* components that are pure DC quantities. However, since the **Symmetrical Components Calculators (SCCs)** are usually based on all-pass filters, they introduce delays too, which are difficult to include in a linearized model of the SCCs. Therefore, the control loops of such a system are designed with relatively low cross-over frequency which results in slow dynamic response.
In this thesis, an effective control approach for a three-phase four-leg inverter capable of supplying highly unbalanced loads is implemented, based on the use of a **Per-Phase *dq* Control**. With this kind of control technique, it is possible to avoid the use of the SCCs blocks, in favour of **Second Order Generalized Integrators (SOGIs)**, whose feature is to have a very fast response [1].

2.2.2 Per-phase *dq* Control

The **per-phase *dq* control** using **SOGIs** can provide balanced output voltages with faster dynamic response than the conventional three-phase *dq* control with symmetrical components calculator used in the traditional three-phase three-wire systems.
The fundamental component of the switched voltage of one phase of the inverter can be modelled as an ideal controlled voltage source E_{inv_i}, where i stand for the phase *(a, b, c)* considered. The inverter inductor current and capacitor voltage are I_{Li} and V_{Ci} respectively. In a similar way, the load connected to that phase of the inverter can be represented by a current source I_{oi} as shown in Figure 2.3:

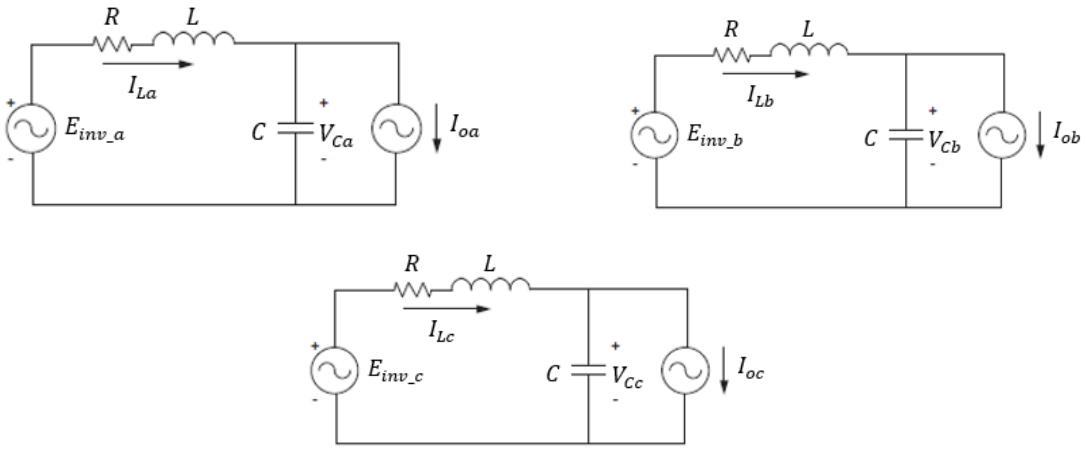

Figure 2.3 – Single-phase equivalent circuits

This representation does not consider the presence of the neutral conductor, which is characterized by a proper impedance that would affect the currents in the three phases.

For representing voltages and currents of a single-phase system in *dq* frame, it is first necessary to generate a two-phase system with orthogonal components. The α components are obtained from the real single-phase circuit representation as in Figure 2.3, while the β components are derived from a fictive circuit where all variables are phase-shifted by 90°, in steady state, with respect to real ones.

For each phase, its relative model circuit in Figure 2.3 is represented in $\alpha\beta$ frame through the following equations:

$$L_f \frac{d\bar{\imath}_{L\alpha\beta}}{dt} = \bar{e}_{inv\alpha\beta} - R_f \bar{\imath}_{L_{\alpha\beta}} - \bar{v}_{C_{\alpha\beta}} \tag{2.9}$$

$$C_f \frac{d\bar{v}_{C\alpha\beta}}{dt} = \bar{\imath}_{L\alpha\beta} - \bar{\imath}_{o_{\alpha\beta}} \tag{2.10}$$

By applying Park transformation, the system passes from a fixed reference frame $\alpha\beta$ to a rotating reference frame *dq* phase shifted of the angle θ as described in paragraph 2.2.5:

$$L_f \begin{bmatrix} \frac{di_d}{dt} \\ \frac{di_q}{dt} \end{bmatrix} = -R_f \begin{bmatrix} i_d \\ i_q \end{bmatrix} + \begin{bmatrix} e_d \\ e_q \end{bmatrix} - \begin{bmatrix} v_d \\ v_q \end{bmatrix} + \omega L_f \begin{bmatrix} i_q \\ -i_d \end{bmatrix} \tag{2.11}$$

$$C_f \begin{bmatrix} \frac{dv_d}{dt} \\ \frac{dv_q}{dt} \end{bmatrix} = \begin{bmatrix} i_d \\ i_q \end{bmatrix} - \begin{bmatrix} i_{od} \\ i_{oq} \end{bmatrix} + \omega C_f \begin{bmatrix} v_q \\ -v_d \end{bmatrix} \tag{2.12}$$

Which can be extended in the following form:

$$\begin{cases} L_f \frac{di_d}{dt} + R_f i_d = e_d - v_d + \omega L_f i_q \\ L_f \frac{di_q}{dt} + R_f i_q = e_q - v_q - \omega L_f i_d \end{cases} \tag{2.13}$$

$$\begin{cases} C_f \frac{dv_d}{dt} = i_d - i_{od} + \omega C_f v_q \\ C_f \frac{dv_q}{dt} = i_q - i_{oq} - \omega C_f v_d \end{cases} \tag{2.14}$$

A common approach for the use of the per-phase dq control with regulated output voltage is to use cascaded inner current and outer voltage loops (Figure 2.4).

The control scheme in Figure 2.4 is referred only to phase a, but it is equally designed for the other phases.

In the inner current loop, V_{Ca} and I_{oa} represent a phase voltage at the output filter, which corresponds to the phase voltage on the load, and the current in the output filter inductor, respectively. v_β is the orthogonal component to V_{Ca} (v_α), required for computing the dq components of the single-phase system. It is obtained with a SOGI, which is implemented in the "a to $\alpha\beta$" block shown in Figure 2.4, described in detail in the following paragraph.

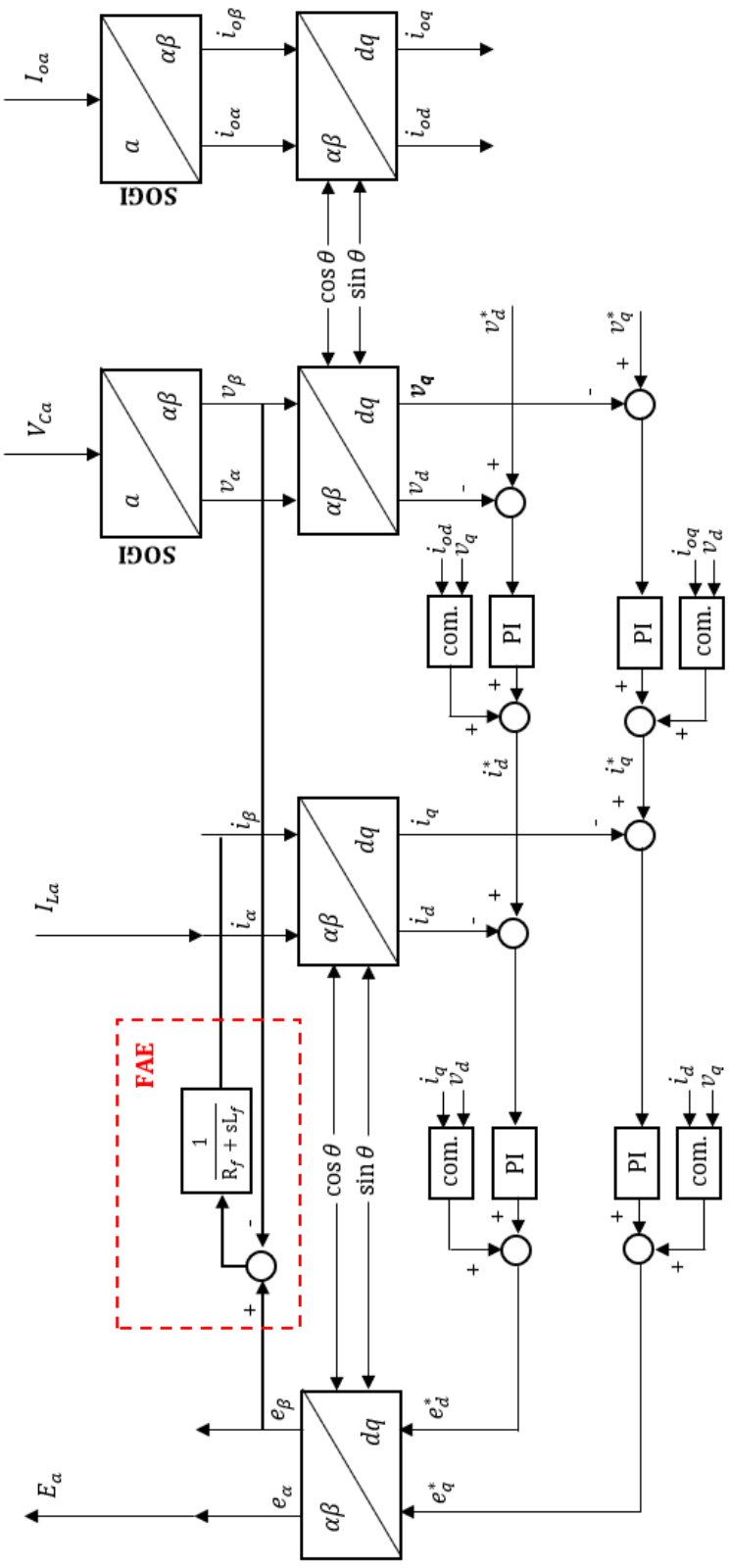

Figure 2.4 – Block diagram of the per-phase cascaded control system; the blocks "com" with their input quantities synthetize the compensation terms

2.2.3 Second Order Generalized Integrator

The **Second Order Generalized Integrator (SOGI)** is the system used to extract α and β components from a single-phase quantity. This method is a good alternative for generating orthogonal signals with respect to other different approaches, such as transport delay or Hilbert transform, whose main drawback is the frequency dependency [12]. The proposed method of creating an orthogonal system is depicted in Figure 2.5.

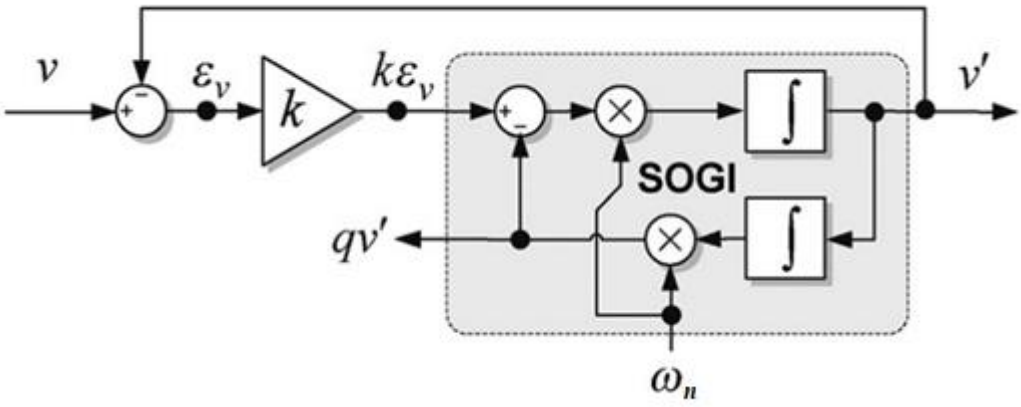

Figure 2.5 – Second Order Generalized Integrator

It has two output variables: v', which corresponds to α component, has the same magnitude and phase as the fundamental of the input signal v, while qv' is phase-shifted of 90°. The presented structure is defined as [13]:

$$SOGI(s) = \frac{v'}{k\varepsilon_v} = \frac{\omega_n s}{s^2 + {\omega_n}^2} \tag{2.15}$$

where ω_n represents the resonance angular frequency of the SOGI, assumed $f_n = {\omega_n}/{2\pi} = 50\ Hz$.

The closed loop transfer functions which relate the input with the outputs are:

$$D_{SOGI}(s) = \frac{v'}{v}(s) = \frac{k\omega_n s}{s^2 + k\omega_n s + {\omega_n}^2} \tag{2.16}$$

$$Q_{SOGI}(s) = \frac{qv'}{v}(s) = \frac{k{\omega_n}^2}{s^2 + k\omega_n s + {\omega_n}^2} \tag{2.17}$$

where k affects the bandwidth of the closed loop system.

Manipulating the transfer functions as it follows:

$$D_{SOGI}(s) = \frac{v'}{v}(s) = \frac{\frac{k}{\omega_n}s}{\frac{s^2}{{\omega_n}^2} + 2\left(\frac{k}{2\omega_n}\right)s + 1} = \frac{\frac{2}{\omega_n}\xi s}{\frac{s^2}{{\omega_n}^2} + \frac{2}{\omega_n}\xi s + 1} \tag{2.18}$$

$$Q_{SOGI}(s) = \frac{qv'}{v}(s) = \frac{k}{\frac{s^2}{{\omega_n}^2} + 2\left(\frac{k}{2\omega_n}\right)s + 1} = \frac{2\xi}{\frac{s^2}{{\omega_n}^2} + \frac{2}{\omega_n}\xi s + 1} \tag{2.19}$$

where $\xi = {k}/{2}$ is the damping factor, it is possible to draw the Bode diagrams for the magnitude and phase and analyse the frequency response of each transfer function for different values of k.

Below there are the real and asymptotic bode diagram for the magnitude and the phase with $k = 1$.

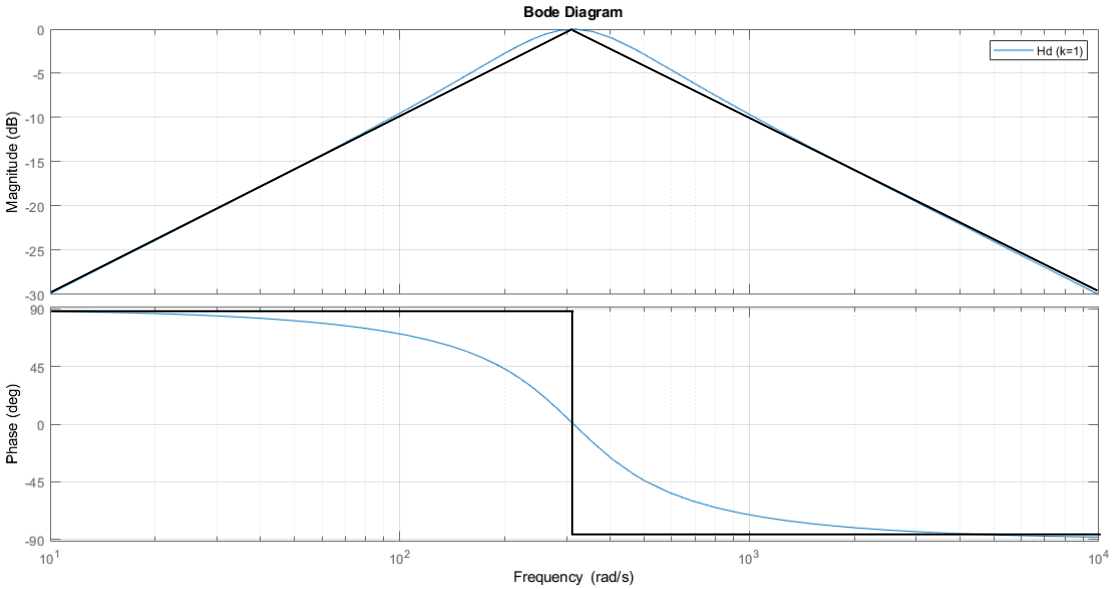

Figure 2.6 – Real and asymptotic bode diagrams of $D_{SOGI}(s)$ transfer function, k=1, $\omega_n=2\pi*50$ rad/s

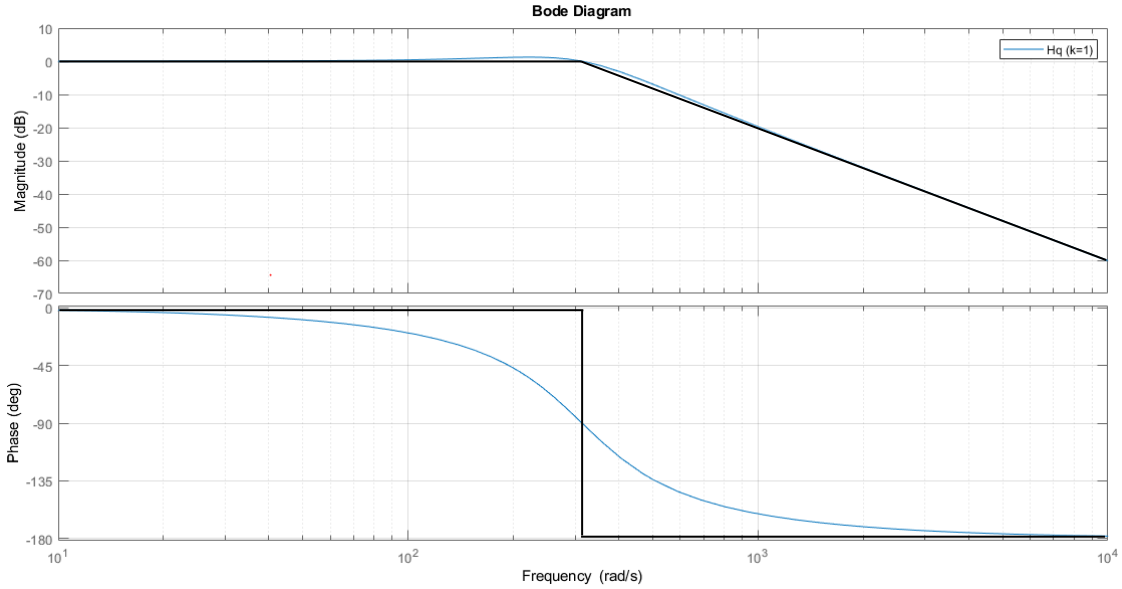

Figure 2.7 – Real and asymptotic diagrams of $Q_{SOGI}(s)$ transfer function, k=1

And for different values of k:

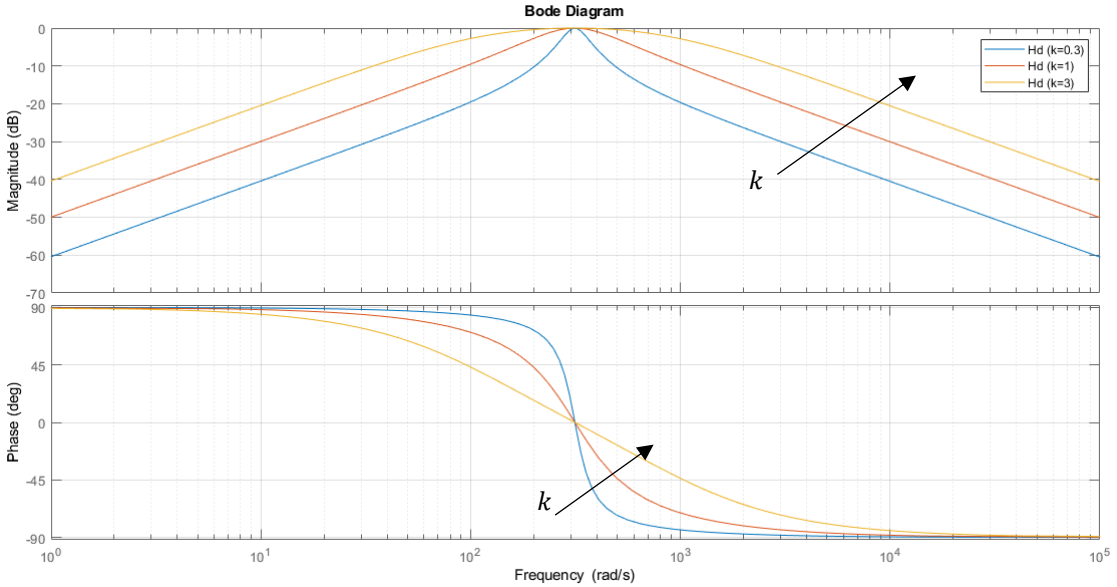

Figure 2.8 – Real bode diagrams of $D_{SOGI}(s)$ transfer function varying k

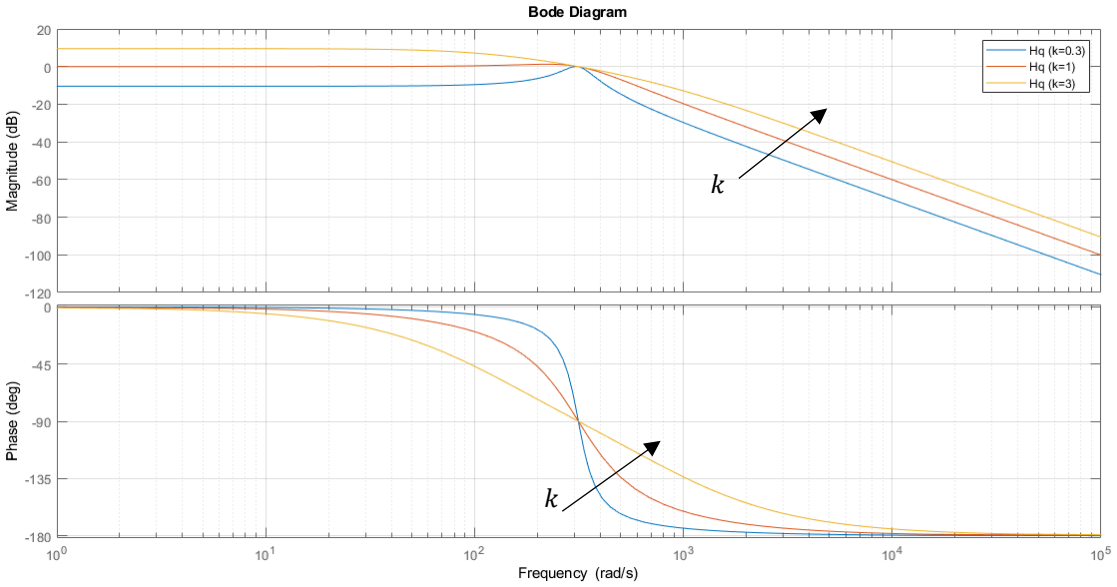

Figure 2.9 – Real bode diagrams of $Q_{SOGI}(s)$ transfer function varying k

The main advantage of the SOGI for the generation of orthogonal voltage (but in the same way for current) is that the input signal v (grid voltage) is filtered without delay resulting in two clean orthogonal voltages waveforms v' and qv', due to the resonance angular frequency of the SOGI at ω_n (grid nominal angular frequency). The level of filtering can be set from gain k as follows: if k

decreases the bandpass of the filter becomes narrower resulting in a heavy filtering, but at the same time the dynamic response of the system will become slower as it can be observed from Figure 2.10, which gives the step response of the transfer function $D_{SOGI}(s)$.

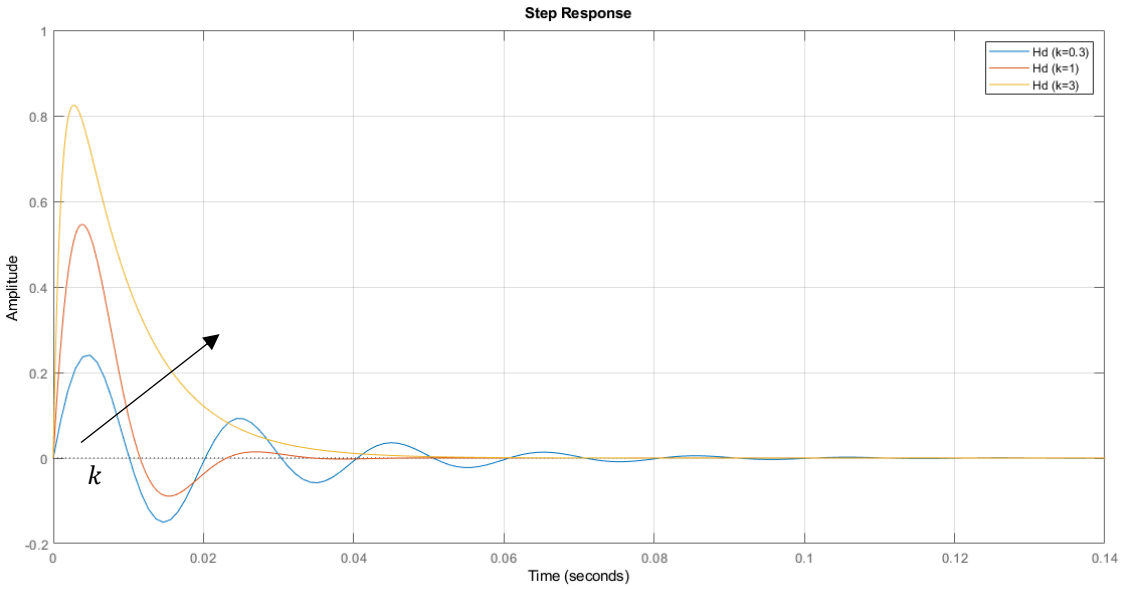

Figure 2.10 – Step response of DSOGI(s) transfer function varying k

It should be noted that this system is not the best choice to compute the β component of the output filter inductor current I_{La}, because this should be varied very fast in order to follow load current variations (caused by possible changes in the load connections) and keep the capacitor voltage regulated. Therefore, it would require a faster method, which is introduced in the following section.

2.2.4 Fictive Axis Emulator

As anticipated, the output filter inductor current components in $\alpha\beta$ frame need a faster system to be computed than the SOGI. The simplest is to generate the fictive orthogonal components by phase shifting the physical ones a quarter of fundamental period [14,15]. A structural diagram of the control scheme, where this method is implemented, is depicted in Figure 2.11. Neglect in the figure

the inverter's structure, which is characterized by the presence of MOSFETs, focusing the attention to the control circuit:

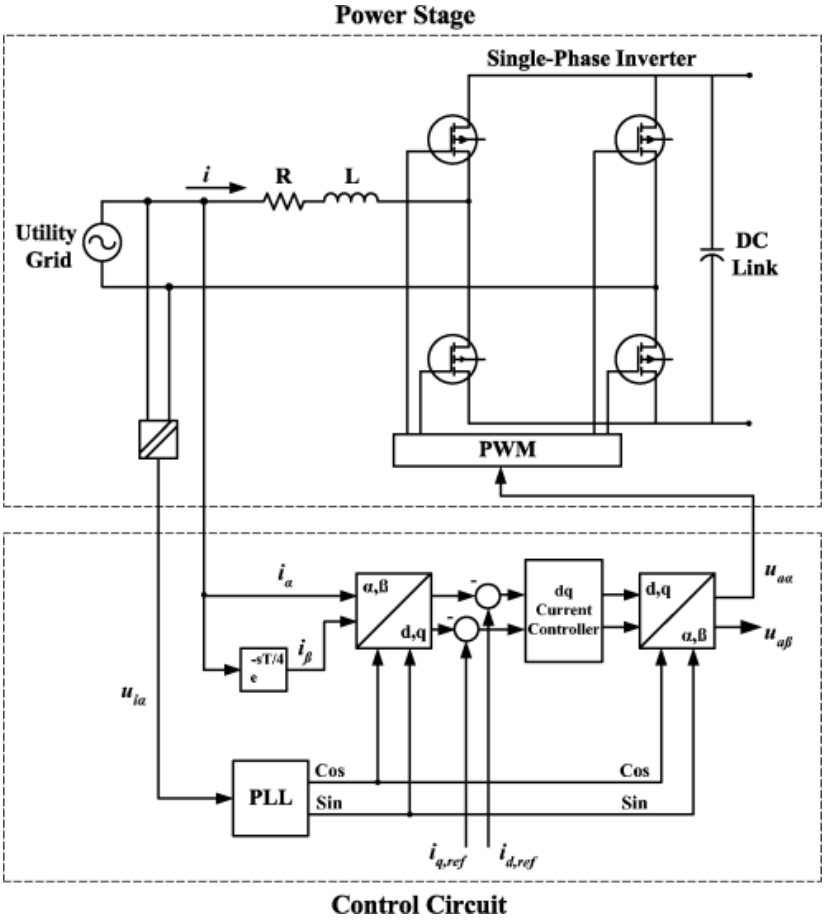

Figure 2.11 – Test system along with the conventional single-phase current-regulation scheme of a single-phase inverter

Note that the application in Figure 2.11 is referred to a single-phase system. As demonstrated in [15], phase shifting the current to create the required orthogonal signal deteriorates the dynamics of the system, because the physical and the orthogonal axes do not run concurrently. Indeed, any transient in the physical axis is also experienced in the orthogonal one, but a quarter of fundamental period later. Considering that the current is subjected to frequent changes, the delay that affects the orthogonal axis deteriorates the dynamics of the system making it slow and oscillatory.

To solve this shortcoming, the orthogonal component of the current must be generated simultaneously with the physical-axis current. This is possible by

emulating a fictive circuit, whose technique is named **FAE (Fictive Axis Emulation)**, as shown in Figure 2.12, which represents the subsequent step of the same case analysed in Figure 2.11:

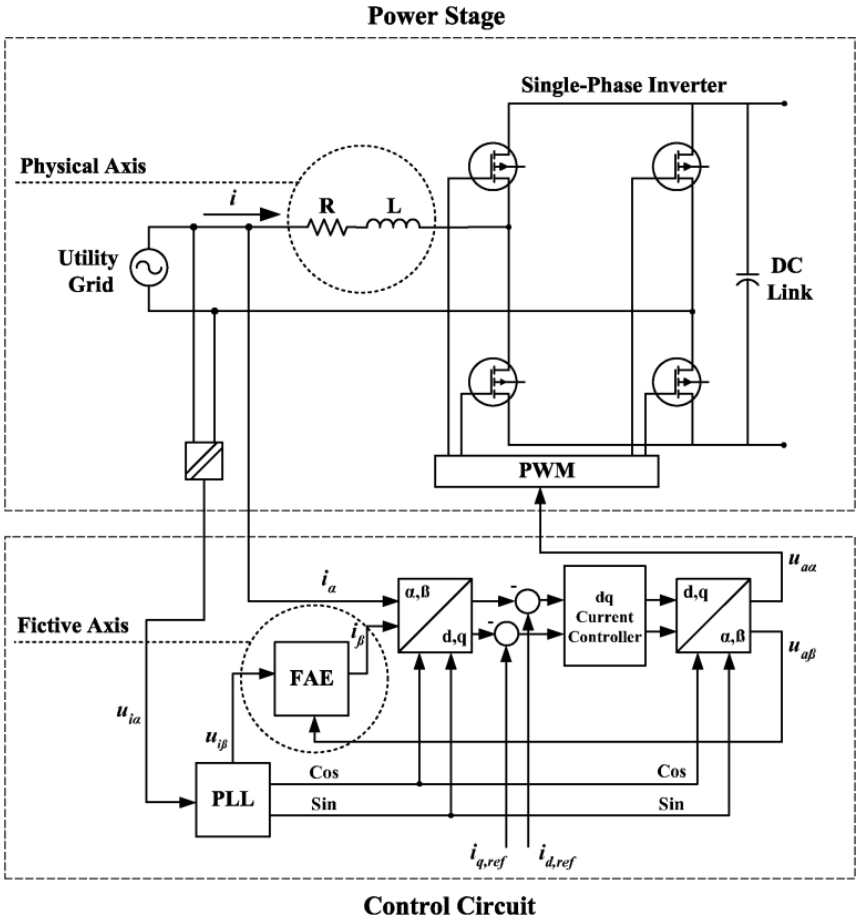

Figure 2.12 – Test system along with the proposed current-control scheme based on FAE

This method is applied in the case study of this thesis: the corresponding block is highlighted in red in Figure 2.4.

The orthogonal current component i_β is obtained using the β coordinate control signal e_β computed through the dq - $\alpha\beta$ transformation, the voltage v_β obtained before from the SOGI and the coupling impedance, R_f and L_f, of the real circuit in Figure 2.3.

The applied transfer function is:

$$G_{FAE}(s) = \frac{\frac{1}{R_f}}{1 + s\frac{L_f}{R_f}} \tag{2.20}$$

Therefore, the β component of the output filter inductor current is:

$$i_\beta = \frac{1}{R_f + sL_f}(e_\beta - v_\beta) \tag{2.21}$$

The detailed structural diagram of the **FAE** is represented in Figure 2.13:

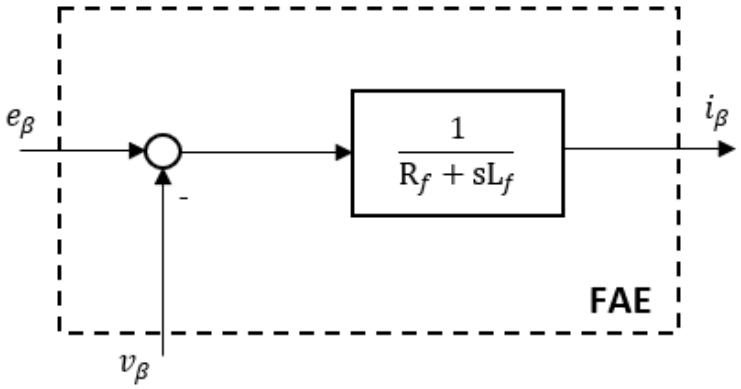

Figure 2.13 – Block diagram of the Fictive Axis Emulator (FAE)

2.2.5 θ angle – From stationary to rotating coordinates

In order to apply the Park and the inverse Park transformation, used in the control system as it can be seen in the overall scheme in Figure 2.4, it is necessary to determine the angle $\hat{\theta}$, which is the phase-shifting between $\alpha\beta$ stationary reference frame and dq rotating reference frame.
In Figure 2.14, the vector $\bar{v}_{\alpha\beta}$ is phase shifted of an angle θ with respect to α axis, and it rotates with angular frequency ω_n.

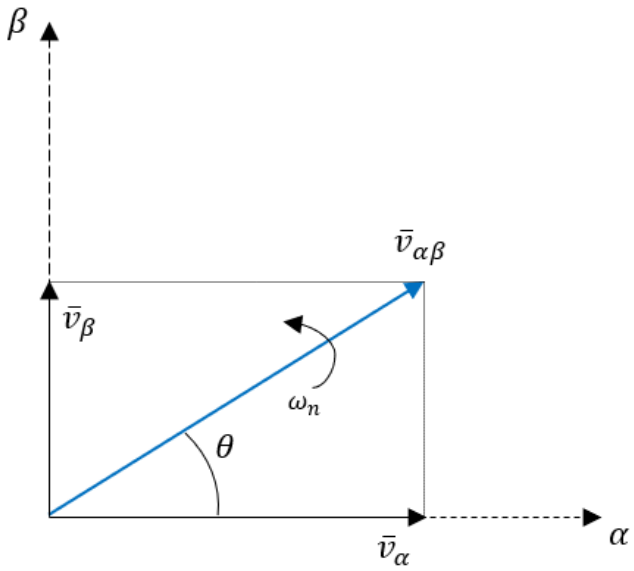

Figure 2.14 – $\alpha\beta$ fixed reference frame

The α and β components are written as it follows:

$$\begin{cases} v_\alpha = V_g \cos\theta \\ v_\beta = V_g \sin\theta \end{cases} \tag{2.22}$$

Introducing the dq rotating reference frame, which rotates at $\hat{\omega}$, we can apply the Park transformation:

$$\bar{v}_{dq} = \begin{bmatrix} v_d \\ v_q \end{bmatrix} = \begin{bmatrix} \cos\hat{\theta} & \sin\hat{\theta} \\ -\sin\hat{\theta} & \cos\hat{\theta} \end{bmatrix} \begin{bmatrix} v_\alpha \\ v_\beta \end{bmatrix} \tag{2.23}$$

Therefore:

$$\begin{cases} v_d = V_g \cos(\theta - \hat{\theta}) \\ v_q = V_g \sin(\theta - \hat{\theta}) \end{cases} \tag{2.24}$$

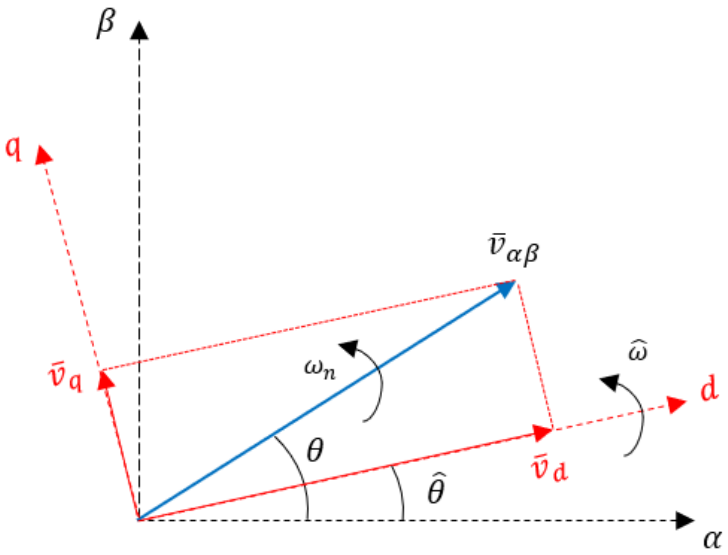

Figure 2.15 – *dq* rotating reference frame

In the control scheme applied for this case study, it is chosen to have v_q^* reference signal equal to zero; consequentially, $v_d^* = V_g$. Therefore, the condition that satisfies these input reference signals is:

$$\hat{\theta} = \theta \tag{2.25}$$

Obviously, in order to work with constant quantities, it is necessary that *dq* reference system rotates with the same angular frequency of the rotating vector $\bar{v}_{\alpha\beta}$, therefore:

$$\hat{\omega} = \omega_n \tag{2.26}$$

For a pure passive load, the angle necessary to apply the Park Transformation is simply:

$$\hat{\theta} = \theta = \tan^{-1}\frac{v_\beta}{v_\alpha} \tag{2.27}$$

2.3 Modulation technique

In this section the modulation technique adopted for the inverter is analysed. It is the method that allows the converter to correctly work in the entire system.

2.3.1 Overview

An unbalanced load in a three-phase four-wire system causes the appearance of a zero-sequence voltage and current, which are source of asymmetries. Several topologies for providing a neutral connection and controlling the zero-sequence voltage have been presented in literature. A three-phase VSI with a neutral leg, that is, a four-leg converter is able to provide zero-sequence voltage, in order to handle the neutral current caused by the unbalanced load. Indeed, several modulation methods for the four-leg inverter have been suggested. The most used is the **Three-Dimensional Space Vector Modulation (3-D SVM)**: it is an extension of the two-dimensional space vector PWM, provided by a 3rd dimension by the extra leg. This technique achieves the full utilization of converter capability such as maximum output voltage at given DC link voltage and minimum output harmonics current at given switching frequency. But the drawback of implementing this method is that it needs a bit of digital logic and high computational power [9].

2.3.2 Carrier-based Pulse Width Modulation

Carrier-based Pulse Width Modulation (PWM) is based on a **triangular carrier wave**. This method can be implemented with a single carrier by using an **"offset voltage"** concept, and it has been demonstrated to be equivalent to a 3-D SVM but with a lower computational power [9].
The addition of a common offset voltage e_{fo}, that is a kind of zero-sequence voltage, to the three-phase input reference voltages provides an optimum

switching sequence, which has some advantages, such as lower harmonic currents and higher available modulation index, compared with traditional sinusoidal PWM methods.

The block diagram of the carrier-based PWM is shown in Figure 2.16. Its inputs (e_{af}, e_{bf}, e_{cf}) are the α components of the three per-phase inverter voltages obtained from Figure 2.4 and required for computing the modulating voltage signals (e_{ao}, e_{bo}, e_{co}), that can be represented as:

$$\begin{cases} e_{ao} = e_{af} + e_{fo} \\ e_{bo} = e_{bf} + e_{fo} \\ e_{co} = e_{cf} + e_{fo} \end{cases} \tag{2.28}$$

Under the following constraints, due to the DC bus voltage:

$$\begin{cases} -V_{dc} \le e_{af}, e_{bf}, e_{cf} \le V_{dc} \\ -V_{dc}/2 \le e_{ao}, e_{bo}, e_{co} \le V_{dc}/2 \\ -V_{dc}/2 \le e_{fo} \le V_{dc}/2 \end{cases} \tag{2.29}$$

Where "*o*" stands for the fictive mid-point of the DC link voltage and e_{fo} is known as the **offset voltage**, calculated as:

$$e_{fo} = \begin{cases} -\dfrac{e_{max}}{2} & e_{min} > 0 \\ -\dfrac{e_{min}}{2} & e_{max} < 0 \\ -\dfrac{e_{max} + e_{min}}{2} & Otherwise \end{cases} \quad , \quad That\ is$$

$$e_{fo} = mid\left(-\frac{e_{max}}{2}, \quad -\frac{e_{min}}{2}, \quad -\frac{e_{max} + e_{min}}{2}\right) \tag{2.30}$$

Where the function "*max*", "*min*" and "*mid*" are applied on the voltages e_{af}, e_{bf} and e_{cf}.

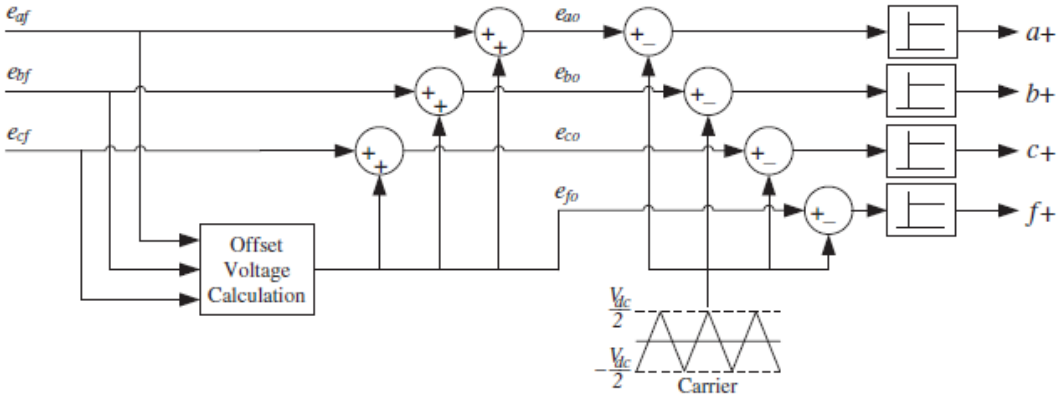

Figure 2.16 – Carrier-based PWM method scheme for four-leg VSI

The additional leg of the four-leg converter in this system topology provide not only a neutral connection but also the **controllability of the neutral point**. By using the offset voltage concept, the best switching sequence as a good compromise between switching losses and harmonic contents can be achieved [9].

The switch states of each leg are determined by comparing the determined modulating voltages e_{ao}, e_{bo} and e_{co} with a **triangular carrier wave**, which presents a period equal to $T_s = {}^{1}/_{f_s}$.

The values of the ON-times of the upper switch of respective legs can be obtained as below [9]:

$$\begin{cases} T_{a_{ON}} = \dfrac{T_s}{2} + \dfrac{e_{ao}}{V_{dc}} T_s \\ T_{b_{ON}} = \dfrac{T_s}{2} + \dfrac{e_{bo}}{V_{dc}} T_s \\ T_{c_{ON}} = \dfrac{T_s}{2} + \dfrac{e_{co}}{V_{dc}} T_s \\ T_{f_{ON}} = \dfrac{T_s}{2} + \dfrac{e_{fo}}{V_{dc}} T_s \end{cases} \tag{2.31}$$

CHAPTER 3
DESIGN TECHNIQUES FOR PI REGULATORS

In this chapter the different design criteria for modelling the PI regulators of the inner and outer control loops are described. Firstly, a simplified and conventional approach is adopted doing some hypotheses that do not consider the transformation from each single-phase quantity to $\alpha\beta$ stationary reference frame, which would introduce the passage from a SISO system to a MIMO system, and an alternative PI design method is developed.

3.1 Control loops on *d* and *q* axes

As it can be seen in the overall control scheme in Figure 2.4, some quantities are extracted and sent into a block named "*com.*". These are appropriate compensation terms used to compensate for the coupling between the *dq* equivalent circuits created by the output filter inductor in the actual AC circuit. Despite the great advantage of the *dq* control on synchronous reference frame to work with DC quantities and thus employing simple **PI-type controllers**, this method has a side effect which is the introduction of mutual coupling terms of ωL and ωC into the model equations, as it can be seen in (2.13) and (2.14). These coupling terms would affect the stabilization, static and dynamic characteristics of the system, therefore it is necessary to decouple the control

on *d* and *q* axis. The inner current and outer voltage control loops on *d* and *q* axes are designed in detail as represented in Figure 3.1 and Figure 3.2, where the compensation terms are adequately included.

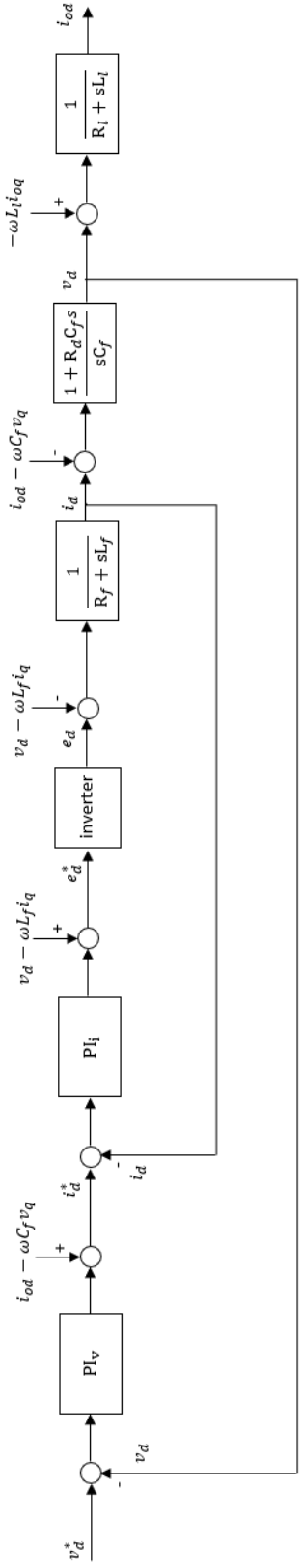

Figure 3.1 – Control loop on *d* axis

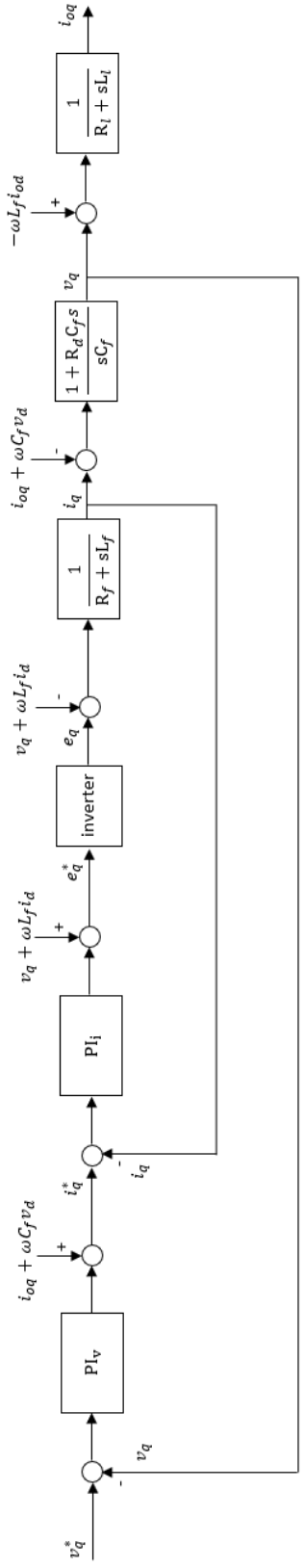

Figure 3.2 – Control loop on *q* axis

3.2 PI Modeling and design method for SISO systems

The first approach to design PI regulators is the conventional one, used for the majority of the control application, and described step by step in the next lines.

The design method is the same for the decoupled control loops of Figure 3.1 and Figure 3.1, which are **Single Input Single Output (SISO)** systems. The transfer function into the block *"inverter"* takes into account the delay introduced by the converter caused by its switching time, and it is modelled with the following transfer function:

$$F_{inv}(s) = \frac{1}{1 + sT_{sw}} \tag{3.1}$$

Which has a pole in $T_{sw}^{-1} = f_{sw} = 10^4\ rad/s$.
Inner and outer control loops are characterized by PI-type regulators, for regulating DC signals, with the outer PI_v regulator 7÷8 times slower than the inner current loop, in order to consider the inner control loop unitary.
The inner PI_i regulator itself is designed with a certain bandwidth, analysing the open loop transfer function $L_i(s)$.
The inner regulator's transfer function is:

$$G_{PI_i}(s) = k_{P_i} + \frac{k_{I_i}}{s} \tag{3.2}$$

Where k_{P_i} and k_{I_i} are the proportional and integral constant of the regulator respectively, and $T_i = k_{P_i}/k_{I_i}$. Therefore:

$$G_{PI_i}(s) = \frac{k_{I_i}}{s}(1 + sT_i) \tag{3.3}$$

The transfer function of the filter's inductance and series resistance is the following:

$$F_L(s) = \frac{1}{R_f + sL_f} = \frac{\frac{1}{R_f}}{1 + s\frac{L_f}{R_f}} = \frac{\frac{1}{R_f}}{1 + sT_f} \tag{3.4}$$

Now it is supposed that the **sampling frequency** f_s, which is the frequency at which each signal is sampled, is equal to the switching frequency f_{sw}.
Moreover, it is necessary to use a fourth order analogic filter, named **Butterworth filter,** because, operating with such a switching frequency, higher order harmonics appear. From the Sampling Theorem, the frequency of this filter must be equal or lower to half the switching frequency: we choose a value $f_B = {\omega_B}/{2\pi} = 5\ kHz$.
Its transfer function is:

$$F_B(s) = \frac{1}{\left(\frac{1}{{\omega_B}^2}\right)s^2 + \left(\frac{0.765}{\omega_B}\right)s + 1} \cdot \frac{1}{\left(\frac{1}{{\omega_B}^2}\right)s^2 + \left(\frac{1.848}{\omega_B}\right)s + 1} \tag{3.5}$$

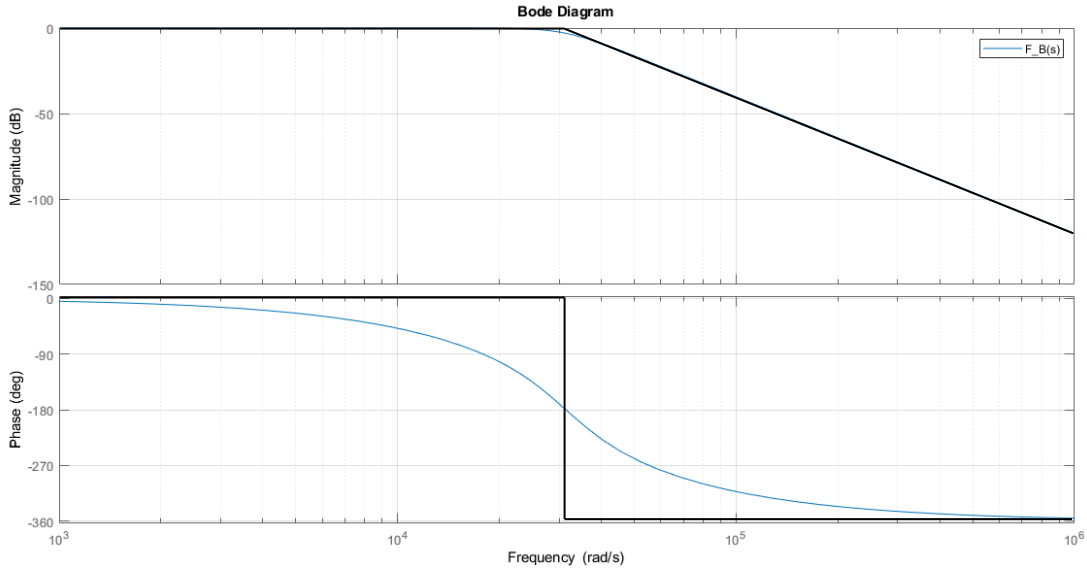

Figure 3.3 – Real and asymptotic Bode diagram of the analogic filter transfer function

Due to this, the PI_i is designed with a pass-band conventionally 10 times lower than the filter's one. It is chosen $f_i = 350\ Hz$.
Therefore, the cut-off angular frequency of the open loop transfer function is $\omega_{c_i} = 2\pi f_i = 2200\ rad/s$.

The open loop transfer function is:

$$L_i(s) = G_{PI_i}(s)\, F_{inv}(s)\, F_L(s)\, F_B(s) \tag{3.6}$$

The relative closed loop transfer function is:

$$K_i(s) = \frac{L_i(s)}{1 + L_i(s)} \tag{3.7}$$

The criteria adopted in order to compute the regulator's parameters is to impose the following conditions:

$$\begin{cases} \left|L_i(j\omega_{c_i})\right| = 1 \\ -\pi + \varphi_{m_i} = \sphericalangle L_i(j\omega_{c_i}) \end{cases} \tag{3.8}$$

That doing some analytical manipulations becomes:

$$\begin{cases} k_{P_i} = \dfrac{1}{\left|G_i(j\omega_{c_i})\right|} \cos\left[-\pi + \varphi_{m_i} - \sphericalangle G_i(j\omega_{c_i})\right] \\ -\dfrac{k_{I_i}}{\omega_{c_i}} = \dfrac{1}{\left|G_i(j\omega_{c_i})\right|} \sin\left[-\pi + \varphi_{m_i} - \sphericalangle G_i(j\omega_{c_i})\right] \end{cases} \tag{3.9}$$

Where $G_i(j\omega_{c_i}) = F_{inv}(j\omega_c)\, F_L(j\omega_{c_i})\, F_B(s)$ is the transfer function of the process and is represented in Figure 2.4. Imposing a phase margin $\varphi_{m_i} = 60°$, which in theory is a value that guarantees a good robustness of the system, from (3.9) and its terms found through Figure 3.4, we found that $k_{P_i} = 2.23\ \Omega$, $k_{I_i} = 646\ \Omega/s$.

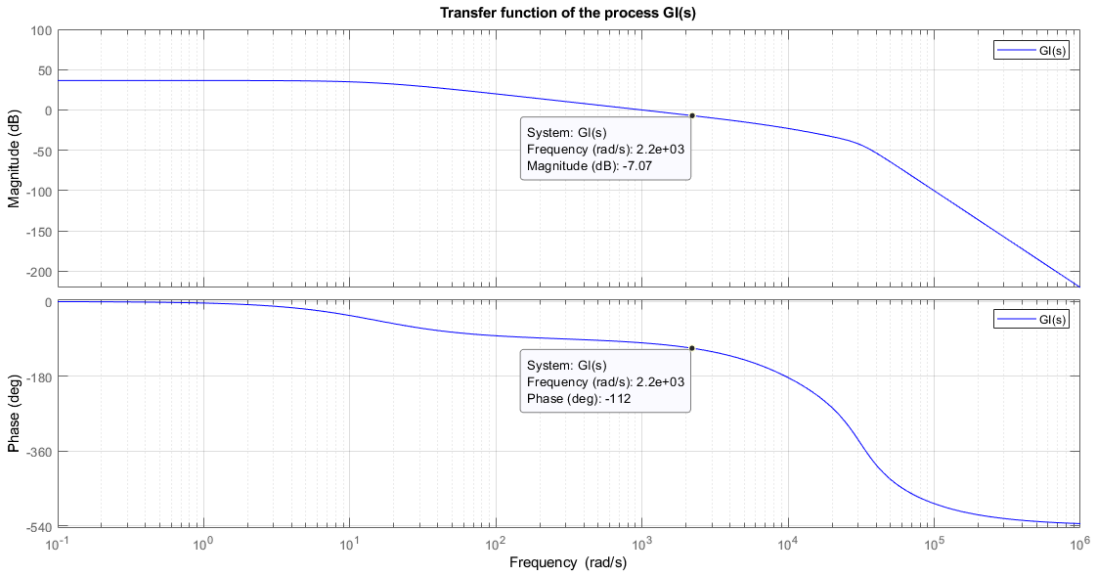

Figure 3.4 – Bode diagram of Gi(s) process' transfer function

The open loop and closed loop transfer functions are depicted below:

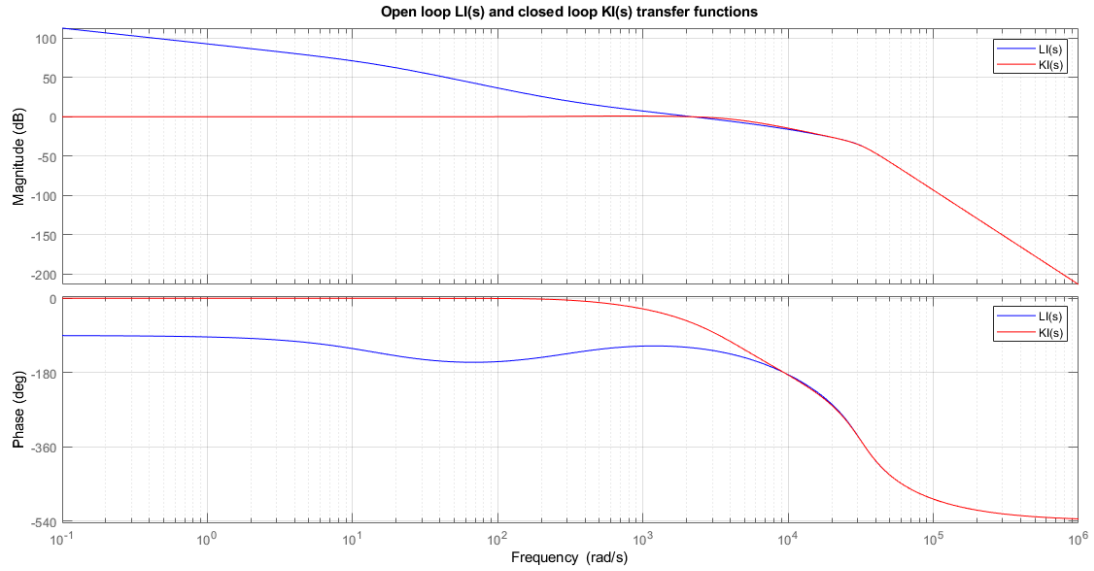

Figure 3.5 – Bode diagram of the open and closed loop transfer function of the inner loop

As usual, the **outer voltage control loop** must have a slower dynamic response with respect to the inner current control loop, therefore its pass-band is chosen as $f_v = 50\ Hz$, that is one seventh of f_i.

As for (3.3), the PI_v transfer function is:

$$G_{PI_v}(s) = \frac{k_{I_v}}{s}(1 + sT_v) \tag{3.10}$$

The transfer function of the filter's capacitance, taking into account its series resistance, is:

$$F_C(s) = \frac{1 + sR_dC_f}{sC_f} \tag{3.11}$$

For the voltage control loop the Butterworth filter of (3.5) is considered too. The new open loop transfer function is:

$$L_v(s) = G_{PI_v}(s)\, K_i(s)\, F_C(s)\, F_B(s) \tag{3.12}$$

The relative closed loop transfer function is:

$$K_v(s) = \frac{L_v(s)}{1 + L_v(s)} \tag{3.13}$$

Now we use the same expressions of (3.8) for the outer voltage control loop, where now the process' transfer function is:

$$G_v(j\omega_{c_v}) = K_i(j\omega_{c_v})\, F_C(j\omega_{c_v})\; F_B(j\omega_{c_v}) \tag{3.14}$$

considering a cut-off angular frequency $\omega_{c_v} = 2\pi f_v \approx 314\, rad/s$ and a phase margin $\varphi_{m_v} = 80°$.

$$\begin{cases} \left|L_v(j\omega_{c_v})\right| = 1 \\ -\pi + \varphi_{m_v} = \sphericalangle L_v(j\omega_{c_v}) \end{cases} \tag{3.15}$$

That becomes:

$$\begin{cases} k_{P_v} = \dfrac{1}{\left|G_v(j\omega_{c_v})\right|}\cos\left[-\pi + \varphi_{m_v} - \sphericalangle G_v(j\omega_{c_v})\right] \\ -\dfrac{k_{I_v}}{\omega_{c_v}} = \dfrac{1}{\left|G_v(j\omega_{c_v})\right|}\sin\left[-\pi + \varphi_{m_v} - \sphericalangle G_v(j\omega_{c_v})\right] \end{cases} \tag{3.16}$$

Therefore, the outer voltage loop's regulator's parameters are $k_{P_v} = 0.0029\ \Omega^{-1}$, $k_{I_v} = 0.0634\ \Omega^{-1}/s$.

In Figure 3.6 $G_v(j\omega)$ is represented:

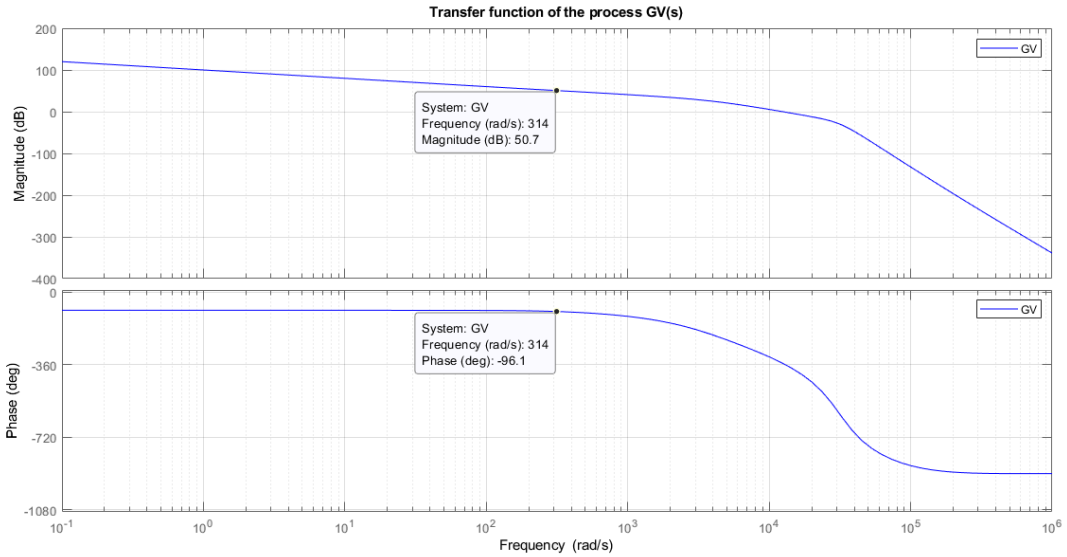

Figure 3.6 – Bode diagram of Gv(s) process' transfer function

The bode diagrams of the relative open loop and closed loop transfer functions are:

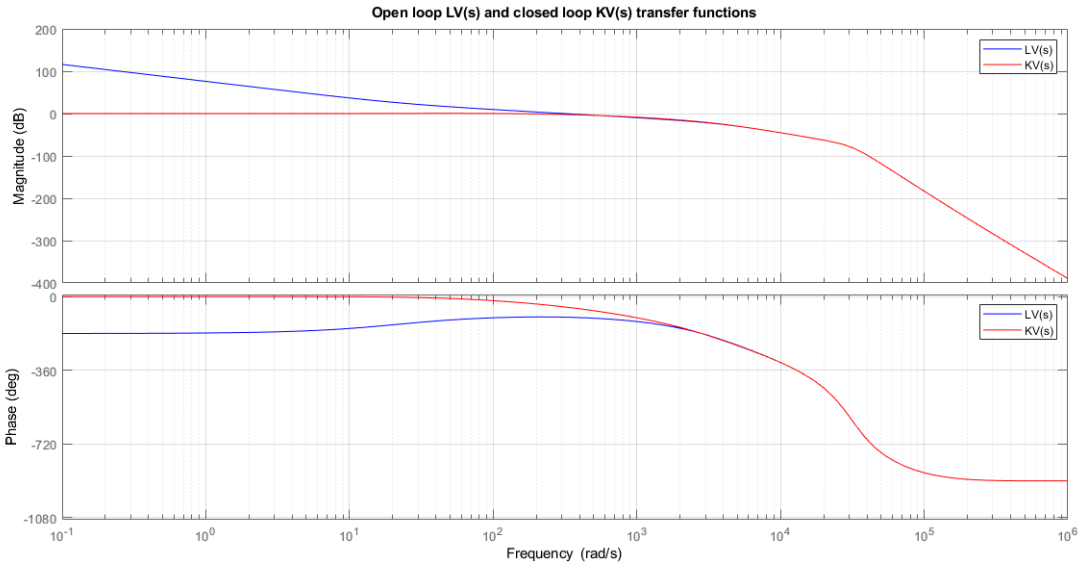

Figure 3.7 – Bode diagram of the open and closed loop transfer function of the outer loop

It is worth noticing that in the evaluation of the open loop transfer functions the compensation terms introduced in the control loops are neglected for simplification reasons.

As it is possible to see in Chapter 4 dedicated to simulations, the analytical computations and the results, obtained through this kind of PI conventional design technique, guarantee the system's stability in theory. Nevertheless, they are not satisfactory in terms of system response in simulation, which shows large and slow oscillation before reaching final conditions. Due to this problem, an alternative method to design PI regulators is investigated.

3.3 PI Modeling and design method for MIMO systems

The traditional approach to design PI regulators in the conventional way does not satisfy the dynamic of the system, resulting in an oscillatory response. The reasons of this drawback are supposed to lie in the approximations done in the design procedure, in particularly not considering the transfer functions (2.16) and (2.17) of the SOGI for passing from single phase quantities to the stationary reference frame $\alpha\beta$. Therefore, a different approach that contemplates this passage is applied. The intention is to use an "a posteriori" method, starting from the current regulator's parameters found with the first design method, expecting a lower phase margin that would justify the problems found in simulation.

Firstly, an attempt to study the new system on dq axes was made, without decoupling each component on two different control loops; finally, for simplicity of calculations reasons, the choice was to carry out the analysis on $\alpha\beta$ axes. These statements require us to see the system no longer as a SISO system, but as a **Multiple Input Multiple Output** (**MIMO)** system, and the transfer functions associated as **transfer matrices**.

3.3.1 MIMO systems analysis on *dq* axes

The new representation of the inner current control loop on *dq* axes is depicted below, neglecting the compensation terms as in the previous case:

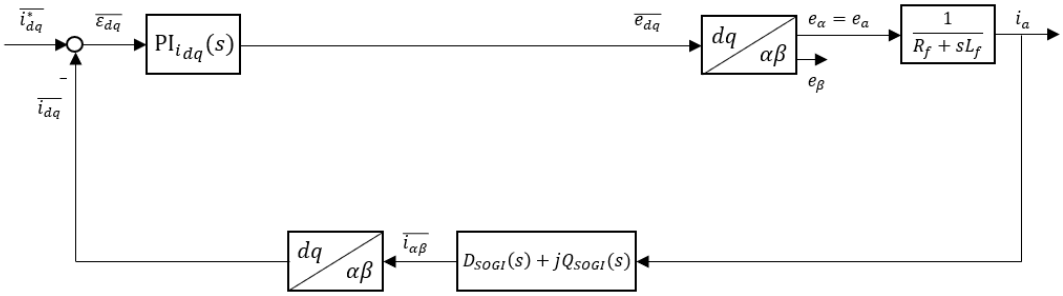

Figure 3.8 – Inner current control loop on *dq* axes (a)

Where $PI_{i_{dq}}(s)$ is the transfer matrix that represents the current regulator on *dq* rotating reference frame.

Moving the feedback loop, the control loop becomes:

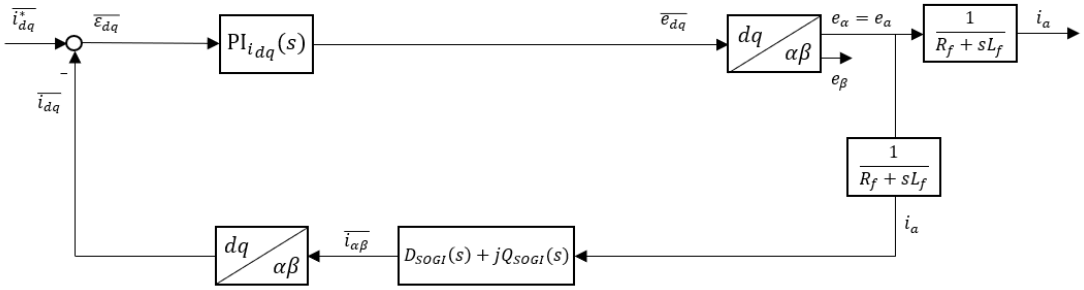

Figure 3.9 – Inner current control loop on *dq* axes (b)

And once again:

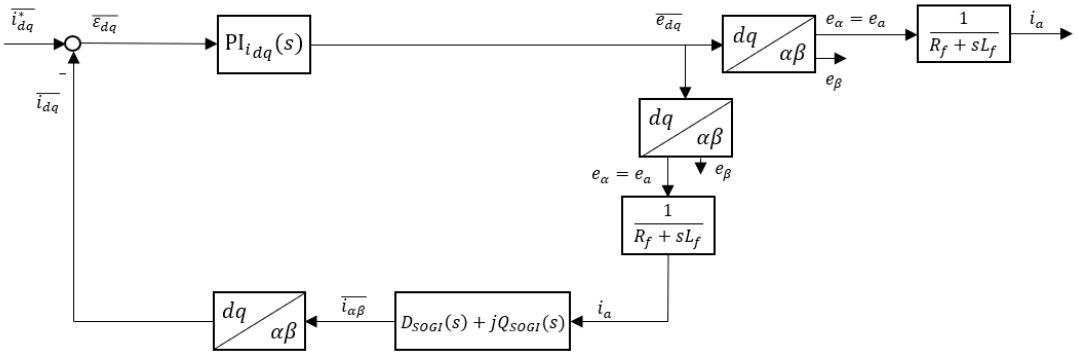

Figure 3.10 – Inner current control loop on dq axes (c)

Since computations based on this kind of system resulted to be very hard, the analysis on dq axes was discarded, preferring the one on $\alpha\beta$ axes.

3.3.2 MIMO systems analysis on $\alpha\beta$ axes

As for the analysis on dq axes, the compensation terms on $\alpha\beta$ axes are neglected too:

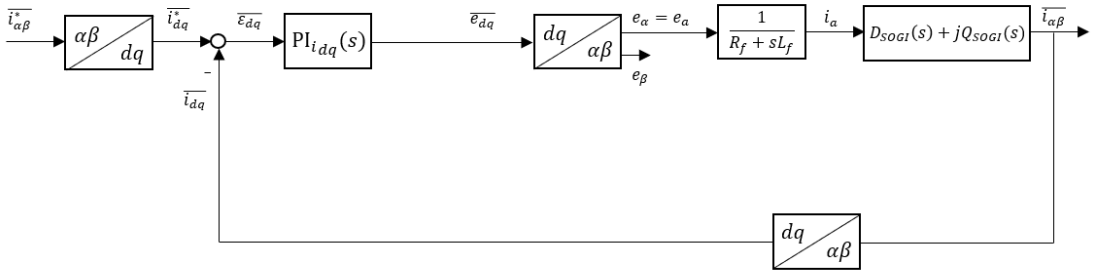

Figure 3.11 – Inner current control loop on $\alpha\beta$ axes (a)

Where $PI_{i_{dq}}(s)$ transfer matrix is [16]:

$$PI_{i_{dq}}(s) = \begin{bmatrix} k_{Pi} + \dfrac{k_{Ii}}{s} & 0 \\ 0 & k_{Pi} + \dfrac{k_{Ii}}{s} \end{bmatrix} \tag{3.17}$$

Doing some manipulations, the feedback loop is moved and the control loop becomes:

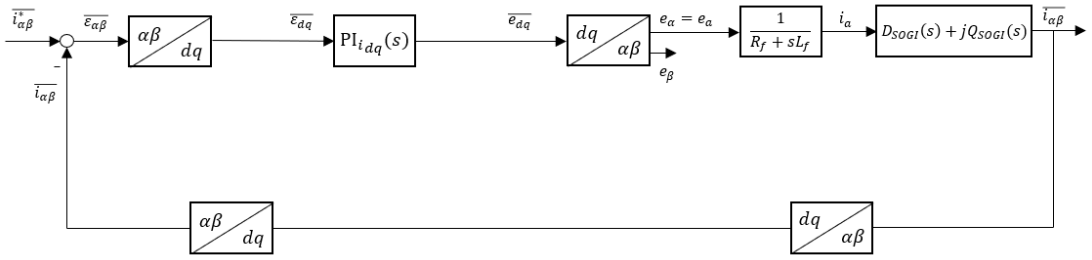

Figure 3.12 – Inner current control loop on $\alpha\beta$ axes (b)

and simplifying the blocks on the feedback loop, the system becomes:

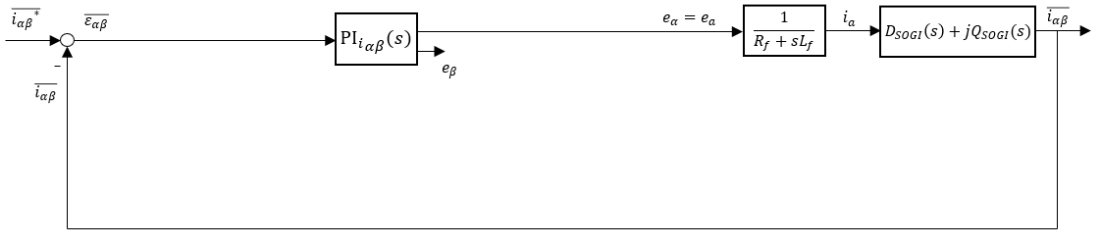

Figure 3.13 – Inner current control loop on $\alpha\beta$ axes (c)

where $PI_{i_{\alpha\beta}}(s)$ is the transfer matrix that represent the current regulator on $\alpha\beta$ rotating reference frame [16]:

$$PI_{i_{\alpha\beta}}(s) = \begin{bmatrix} k_{Pi} + \dfrac{k_{Ii}s}{s^2 + {\omega_n}^2} & \dfrac{k_{Ii}s}{s^2 + {\omega_n}^2} \\ -\dfrac{k_{Ii}s}{s^2 + {\omega_n}^2} & k_{Pi} + \dfrac{k_{Ii}s}{s^2 + {\omega_n}^2} \end{bmatrix} \tag{3.18}$$

The transfer matrix $D_{SOGI}(s) + jQ_{SOGI}(s)$ represents the SOGI, which transforms the single-phase current in $\alpha\beta$ components. Its representation as a transfer matrix is found as it follows.

Writing $\overline{i_{\alpha\beta}}$ as a column vector composed by its components α and β:

$$\overline{i_{\alpha\beta}} = \begin{bmatrix} i_\alpha \\ i_\beta \end{bmatrix} \tag{3.19}$$

It is equal to:

$$\begin{bmatrix} i_\alpha \\ i_\beta \end{bmatrix} = \begin{bmatrix} D_{SOGI}(s) \\ Q_{SOGI}(s) \end{bmatrix} i_a \tag{3.20}$$

Where $D_{SOGI}(s)$ and $Q_{SOGI}(s)$ are the SOGI transfer functions of (2.16) and (2.17).

The single-phase current is:

$$i_a = \frac{1}{R_f + sL_f} e_a \tag{3.21}$$

Therefore:

$$\begin{bmatrix} i_\alpha \\ i_\beta \end{bmatrix} = \frac{1}{R_f + sL_f} \begin{bmatrix} D_{SOGI}(s) \\ Q_{SOGI}(s) \end{bmatrix} e_a \tag{3.22}$$

Where $e_a = e_\alpha$.

Reporting the relationship between $\overline{\imath_{\alpha\beta}} = [i_\alpha \quad i_\beta]^T$ and $\overline{e_{\alpha\beta}} = [e_\alpha \quad e_\beta]^T$, it is necessary to add a null column vector to the expression of the SOGI in (3.22), in order to make the current vector independent from e_β:

$$\begin{bmatrix} i_\alpha \\ i_\beta \end{bmatrix} = \frac{1}{R_f + sL_f} \begin{bmatrix} D_{SOGI}(s) & 0 \\ Q_{SOGI}(s) & 0 \end{bmatrix} \begin{bmatrix} e_\alpha \\ e_\beta \end{bmatrix} \tag{3.23}$$

Therefore, the SOGI transfer matrix is:

$$D_{SOGI}(s) + jQ_{SOGI}(s) = \begin{bmatrix} D_{SOGI}(s) & 0 \\ Q_{SOGI}(s) & 0 \end{bmatrix} \tag{3.24}$$

At this point, the goal is to find the open loop expression to study, that will constitute the transfer matrix between the multiple input vector $\overline{\varepsilon_{\alpha\beta}} = [\varepsilon_\alpha \quad \varepsilon_\beta]^T$, which is the difference between the reference current $\overline{\imath_{\alpha\beta}{}^*}$ and the feedback $\overline{\imath_{\alpha\beta}}$, and the multiple output $\overline{\imath_{\alpha\beta}}$.

Considering that:

$$\begin{bmatrix} e_\alpha \\ e_\beta \end{bmatrix} = PI_{i_{\alpha\beta}}(s) \begin{bmatrix} \varepsilon_\alpha \\ \varepsilon_\beta \end{bmatrix} \tag{3.25}$$

Substituting (3.25) in (3.22):

$$\begin{bmatrix} i_\alpha \\ i_\beta \end{bmatrix} = \frac{1}{R_f + sL_f}[D_{SOGI}(s) + jQ_{SOGI}(s)]PI_{i_{\alpha\beta}}(s)\begin{bmatrix} \varepsilon_\alpha \\ \varepsilon_\beta \end{bmatrix} \tag{3.26}$$

Therefore, the open loop transfer matrix is:

$$L_{i_{\alpha\beta}}(s) = \frac{1}{R_f + sL_f}[D_{SOGI}(s) + jQ_{SOGI}(s)]PI_{i_{\alpha\beta}}(s) \tag{3.27}$$

Which in matrix representation is:

$$L_{i_{\alpha\beta}}(s) = \begin{bmatrix} \dfrac{D_{SOGI}(s)\left(k_{Pi} + \dfrac{k_{Ii}s}{s^2 + {\omega_n}^2}\right)}{R_f + sL_f} & \dfrac{D_{SOGI}(s)\left(\dfrac{k_{Ii}s}{s^2 + {\omega_n}^2}\right)}{R_f + sL_f} \\ \dfrac{Q_{SOGI}(s)\left(\dfrac{k_{Ii}s}{s^2 + {\omega_n}^2}\right)}{R_f + sL_f} & \dfrac{Q_{SOGI}(s)\left(k_{Pi} + \dfrac{k_{Ii}s}{s^2 + {\omega_n}^2}\right)}{R_f + sL_f} \end{bmatrix} \tag{3.28}$$

The closed loop transfer matrix is:

$$K_{i_{\alpha\beta}}(s) = \left[I + L_{i_{\alpha\beta}}(s)\right]^{-1} L_{i_{\alpha\beta}}(s) \tag{3.29}$$

The stability of the closed loop system can be analysed using the **Generalized Nyquist criterion** [17, 18], which is applied for MIMO systems.

Generalized Nyquist criterion:

Assuming the open loop transfer matrix:

$$L_{i_{\alpha\beta}}(s) = \begin{bmatrix} L_{i_{\alpha\beta}11}(s) & L_{i_{\alpha\beta}12}(s) \\ L_{i_{\alpha\beta}21}(s) & L_{i_{\alpha\beta}22}(s) \end{bmatrix} \tag{3.30}$$

has no right-half plane poles, the closed loop transfer matrix $K_{i_{\alpha\beta}}(s)$ is asymptotically stable if and only if the Nyquist curves for the eigenvalues $\lambda_{1,2}(s)$ of $L_{i_{\alpha\beta}}(s)$ taken together, do not encircle the critical point -1+j0 for $s = j\omega, -\infty < \omega < +\infty$ [18].

Application:

First of all, it is necessary to verify that the open loop transfer function has no right-half plane poles.

> *Definition:* The set of poles for a multivariable system, multiplicity included, coincides with the roots of the characteristic equation:
>
> $$\phi(s) = 0 \tag{3.31}$$
>
> where $\phi(s)$ it the characteristic polynomial of a system with transfer matrix $G(s)$ [19].
>
> *Theorem:* The characteristic polynomial $\phi(s)$ is equal to the lowest common denominator of all non-zero minors of all $G(s)$ transfer matrix's ranks [19].

Applying the definition of poles for multivariable systems, it is found that the characteristic polynomial is:

$$\phi(s) = \left(R_f + sL_f\right)(s^2 + k\omega_n s + {\omega_n}^2)(s^2 + {\omega_n}^2) = 0 \tag{3.32}$$

therefore, the set of the p_i poles is:

$$p_1 = -\frac{R_f}{L_f}$$

$$p_{2,3} = \frac{\omega_n}{2}\left(-1 \pm j\sqrt{3}\right)$$

$$p_{4,5} = \pm j\omega_n$$

None of the poles is in the right-half plane, therefore we can check the stability of the system.

The eigenvalues $\lambda_k(s)$, with $k = \{1,2\}$, of our transfer matrix $L_{i_{\alpha\beta}}(s)$ are defined according to the equation:

$$\left|\lambda_k(s)\, I \;-\; L_{i_{\alpha\beta}}(s)\right| = 0 \tag{3.33}$$

where I is the identity matrix.

Doing the analytical calculations, it is found that:

$$\lambda_{1,2}(s) = \frac{L_{i_{\alpha\beta}11}(s) + L_{i_{\alpha\beta}22}(s)}{2} \pm \sqrt{\left[\frac{L_{i_{\alpha\beta}11}(s) - L_{i_{\alpha\beta}22}(s)}{2}\right]^2 + L_{i_{\alpha\beta}21}(s) L_{i_{\alpha\beta}12}(s)} \tag{3.34}$$

The Nyquist diagrams of the eigenvalues $\lambda_{1,2}(s)$ are plotted in MATLAB, and shown in Figure 3.14 and 3.15:

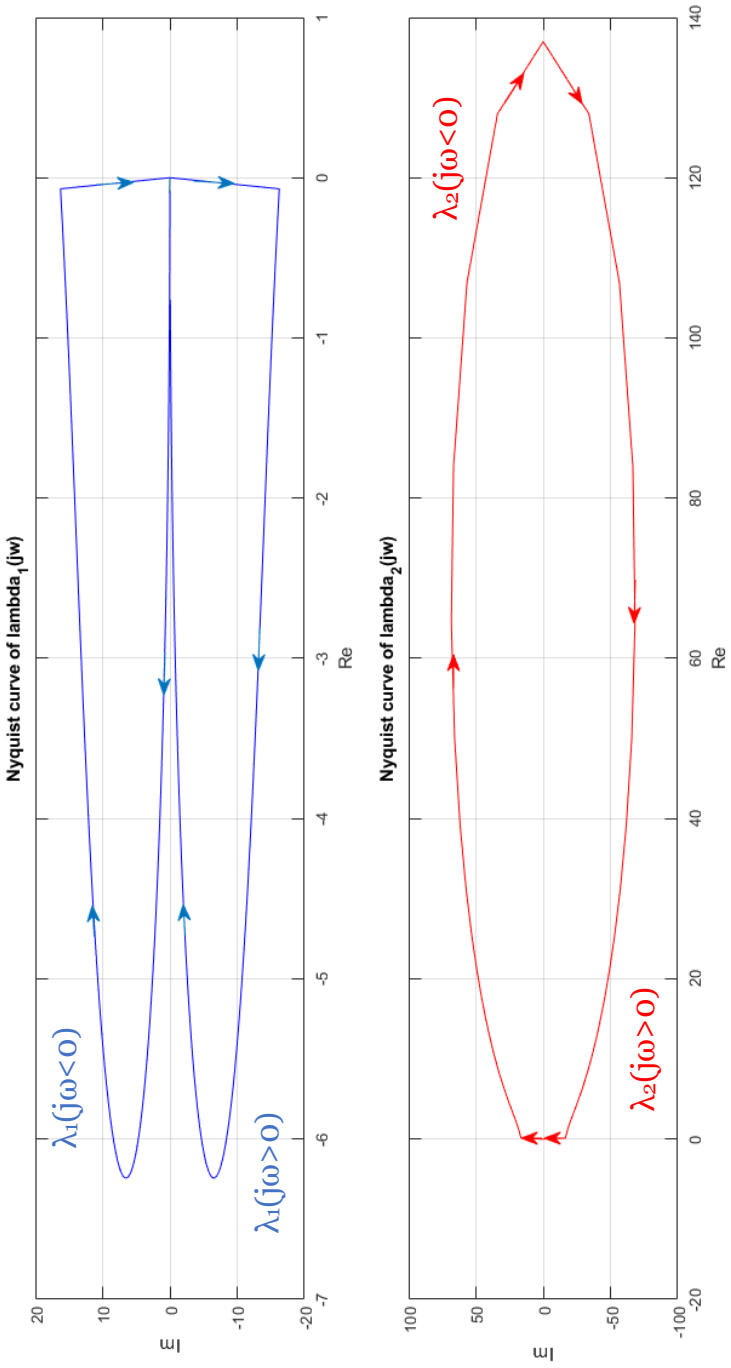

Figure 3.14 – Nyquist diagrams of the eigenvalues $\lambda_{1,2}(s)$

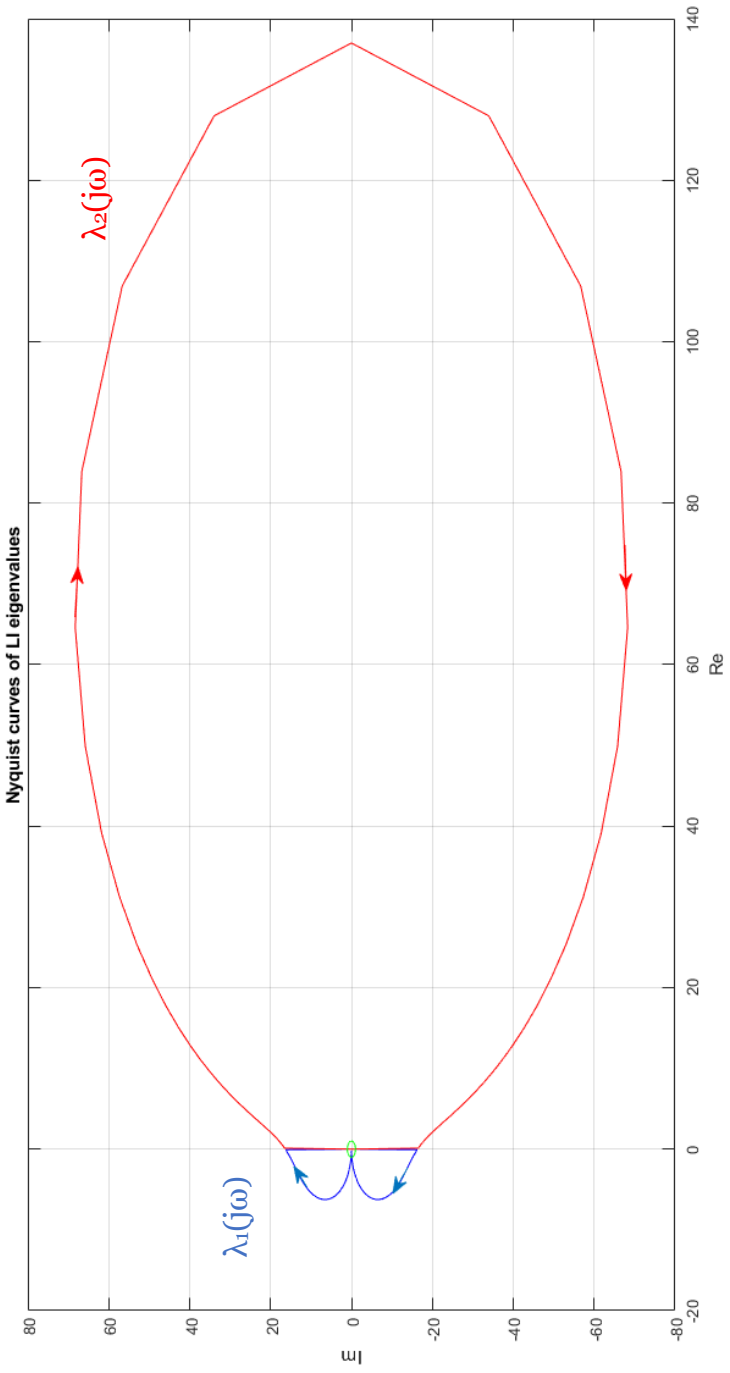

Figure 3.15 – Overall Nyquist diagram of the eigenvalues $\lambda_{1,2}(s)$

Zooming on the area that surrounds point -1+j0 :

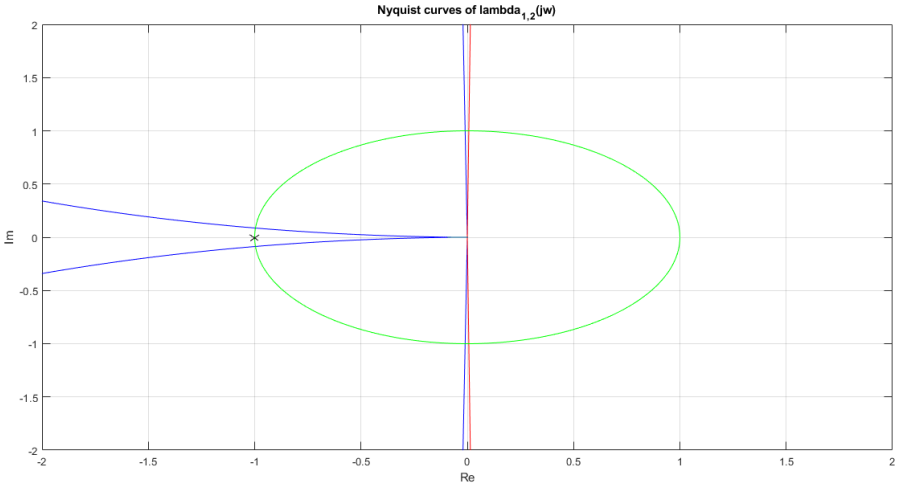

Figure 3.16 – Detailed Nyquist diagram of the eigenvalues $\lambda_{1,2}(s)$

It is possible to note that this critical point is not encircled by the Nyquist curves, therefore the Generalized Nyquist Criterion is verified, and the closed loop system is asymptotically stable.

Looking at Figure 3.16, we see also that the phase margin for the current regulator φ_{m_i}, defined as the angle between the negative real axis and the intersection closest to -1+j0 of the Nyquist curve with the unit circle, is very low.

It results exactly that $\varphi_{m_i} = 5.12°$, which is significantly lower than the value of 60° imposed in the traditional design method, as we expected.

In order to obtain a real phase margin of 60°, the regulators parameters $k_{P_i} = 2.23\ \Omega$, $k_{I_i} = 646\ \Omega/s$ are changed one by one:

Fixing $\boldsymbol{k_{P_i} = 2.23\ \Omega}$:

$k_{I_i} = 646\ \Omega/s \quad \rightarrow \quad \varphi_{m_i} = 5.12°$

$k_{I_i} = 300\ \Omega/s \quad \rightarrow \quad \varphi_{m_i} = 15.14°$

$k_{I_i} = 50\ \Omega/s \quad \rightarrow \quad \varphi_{m_i} = 22.80°$

$k_{I_i} = 10\ \Omega/s \quad \rightarrow \quad \varphi_{m_i} = 24.02°$

$\boldsymbol{k_{I_i} = 8.85\ \Omega/s \quad \rightarrow \quad \varphi_{m_i} = 24.05°}$

Fixing $\boldsymbol{k_{I_i} = 8.85\ \Omega/s}$:

$k_{P_i} = 2\ \Omega \quad \rightarrow \quad \varphi_{m_i} = 25.51°$

$k_{P_i} = 1.5\ \Omega \quad \rightarrow \quad \varphi_{m_i} = 29.97°$

$k_{P_i} = 1\ \Omega \quad \rightarrow \quad \varphi_{m_i} = 37.90°$

$k_{P_i} = 0.7\ \Omega \quad \rightarrow \quad \varphi_{m_i} = 47.42°$

$\boldsymbol{k_{P_i} = 0.5\ \Omega \quad \rightarrow \quad \varphi_{m_i} = 59.14°}$

Therefore, the new optimum values of the current regulator's parameters are $k_{P_i} = 0.5\ \Omega$ and $k_{I_i} = 8.85\ \Omega/s$, corresponding to a cut-off angular frequency of $\omega_{c_i} = 300 \div 400\ rad/s$.

The Nyquist diagram becomes:

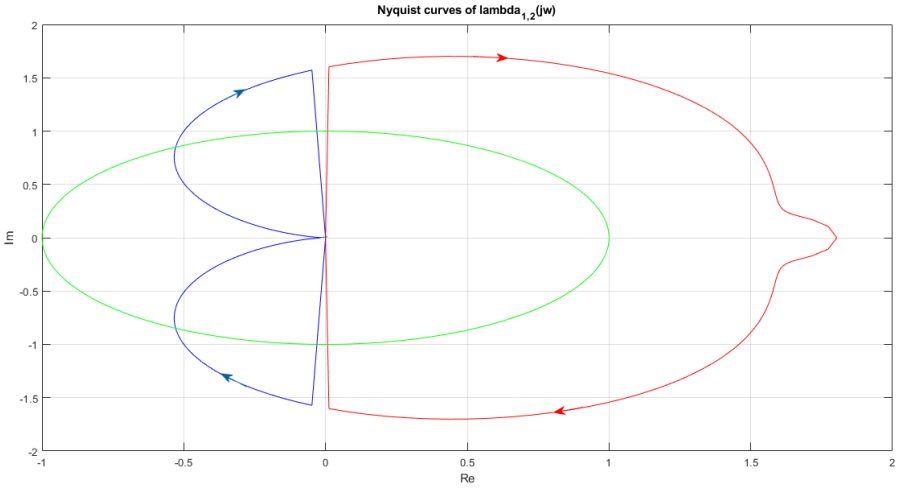

Figure 3.17 – Overall Nyquist diagram of the eigenvalues $\lambda_{1,2}(s)$ for φ_{mi}=60°

At this point, the **static and dynamic performances** of the feedback system are analysed.

For MIMO systems, the condition to evaluate the dynamic performance is [19]:

$$\overline{\sigma}(L_{i_{\alpha\beta}}(s)) \ll 1 \qquad (3.35)$$

For the static performance of the system:

$$\underline{\sigma}(L_{i_{\alpha\beta}}(s)) \gg 1 \tag{3.36}$$

where $\overline{\sigma}$ and $\underline{\sigma}$ are the **singular values** of the 2x2 transfer matrix $L_{i_{\alpha\beta}}(s)$. The rules to determine analytically the singular values are shown in Appendix C.

The Bode diagrams of the singular values corresponding to the inner regulator's parameter $k_{P_i} = 0.5\ \Omega$ and $k_{I_i} = 8.85\ \Omega/s$ are shown below:

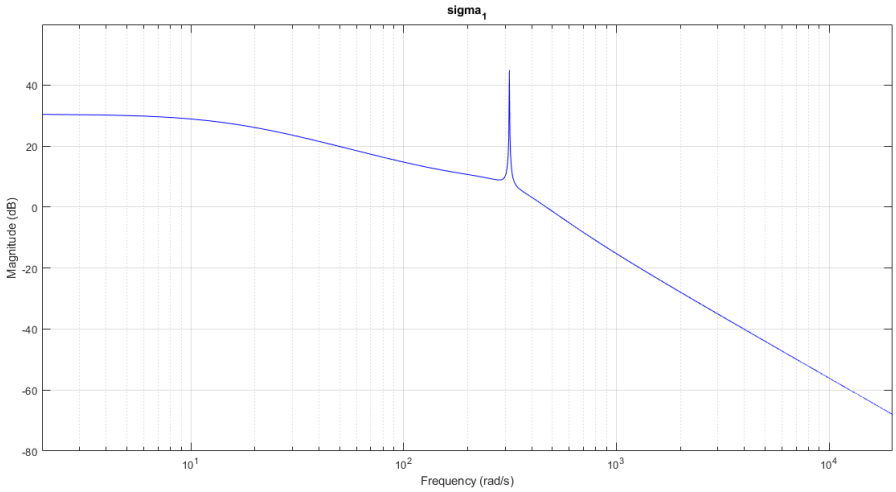

Figure 3.18 – Bode diagram of $\overline{\sigma}$ singular value

From Figure 3.18 it is possible to see that the critical angular frequency is exactly $\omega_{c_i} = 300 \div 400\ rad/s$, as found form the Nyquist diagram; condition (3.35) is verified only for angular frequencies considerably higher than ω_{c_i}.

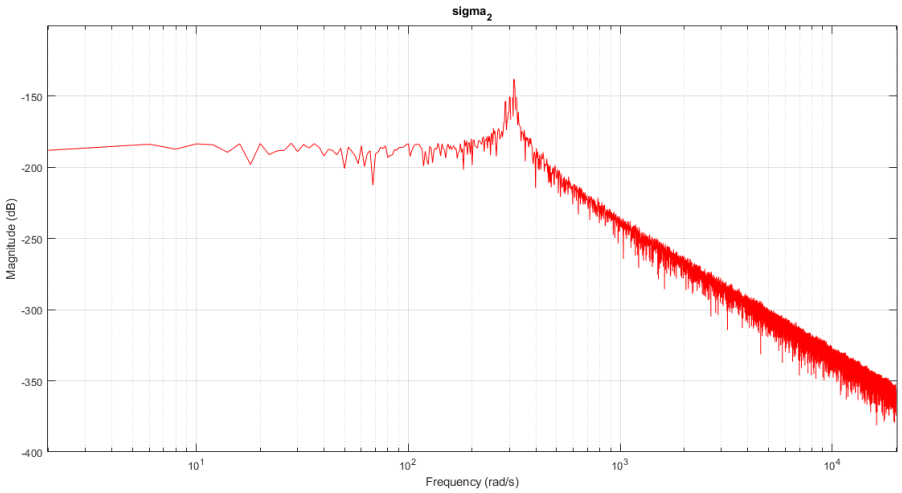

Figure 3.19 – Bode diagram of $\underline{\sigma}$ singular value

Condition (3.36) is not verified for any value of angular frequency: being $\underline{\sigma}(L_{i_{\alpha\beta}}(s)) \ll 1$, it means that the error at transitory finished is high.

From these results, we expected that in simulation of Chapter 4 the error processed by the regulator will not be zero in final conditions.

Now, using the same approach as for the inner current control loop, it is necessary to design the outer voltage control loop, in order to find its new k_{P_v} and k_{I_v} parameters.

Starting from the following representation of the control loop:

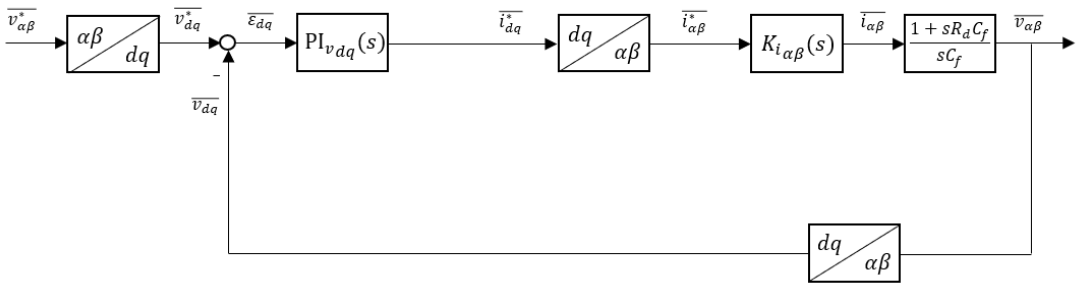

Figure 3.20 – Outer voltage control loop on $\alpha\beta$ axes (a)

which becomes:

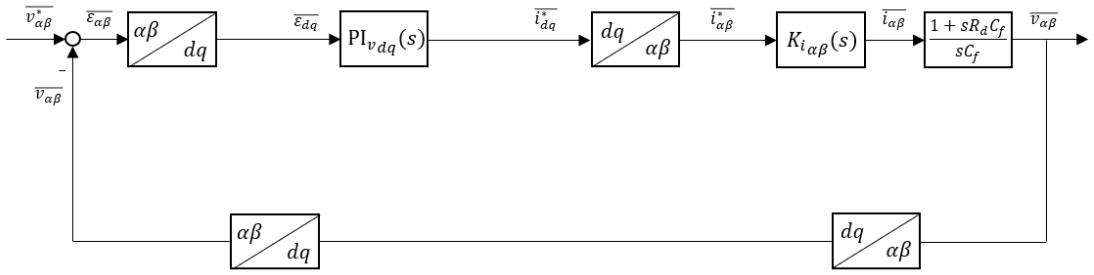

Figure 3.21 – Outer voltage control loop on $\alpha\beta$ axes (b)

Doing the same simplification adopted before, we consider the gain represented by the closed loop transfer matrix $K_{i_{\alpha\beta}}(s)$ unitary, supposing the outer voltage loop's bandwidth significantly lower than ω_{c_i}.

The final scheme is:

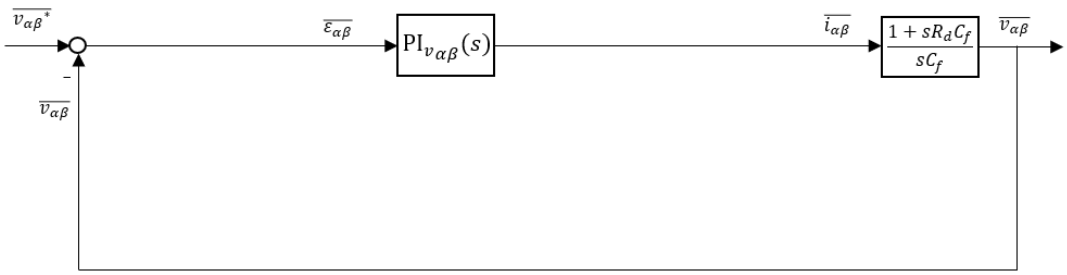

Figure 3.22 – Outer voltage control loop on $\alpha\beta$ axes (c)

where $PI_{v_{\alpha\beta}}(s)$ is the transfer matrix that represent the voltage regulator on $\alpha\beta$ rotating reference frame:

$$PI_{v_{\alpha\beta}}(s) = \begin{bmatrix} k_{Pv} + \dfrac{k_{Iv}s}{s^2 + {\omega_n}^2} & \dfrac{k_{Iv}s}{s^2 + {\omega_n}^2} \\ -\dfrac{k_{Iv}s}{s^2 + {\omega_n}^2} & k_{Pv} + \dfrac{k_{Iv}s}{s^2 + {\omega_n}^2} \end{bmatrix} \tag{3.37}$$

Therefore, the open loop transfer matrix of the voltage control loop is:

$$L_{v_{\alpha\beta}}(s) = \frac{1 + s\,R_dC_f}{sC_f} \begin{bmatrix} k_{Pv} + \dfrac{k_{Iv}s}{s^2 + {\omega_n}^2} & \dfrac{k_{Iv}s}{s^2 + {\omega_n}^2} \\ -\dfrac{k_{Iv}s}{s^2 + {\omega_n}^2} & k_{Pv} + \dfrac{k_{Iv}s}{s^2 + {\omega_n}^2} \end{bmatrix} \tag{3.38}$$

Applying the same procedure as for the inner current control loop, the eigenvalues $\lambda_{3,4}(s)$ associated to the open loop transfer matrix $L_{v_{\alpha\beta}}(s)$ give rise to the following Nyquist diagram:

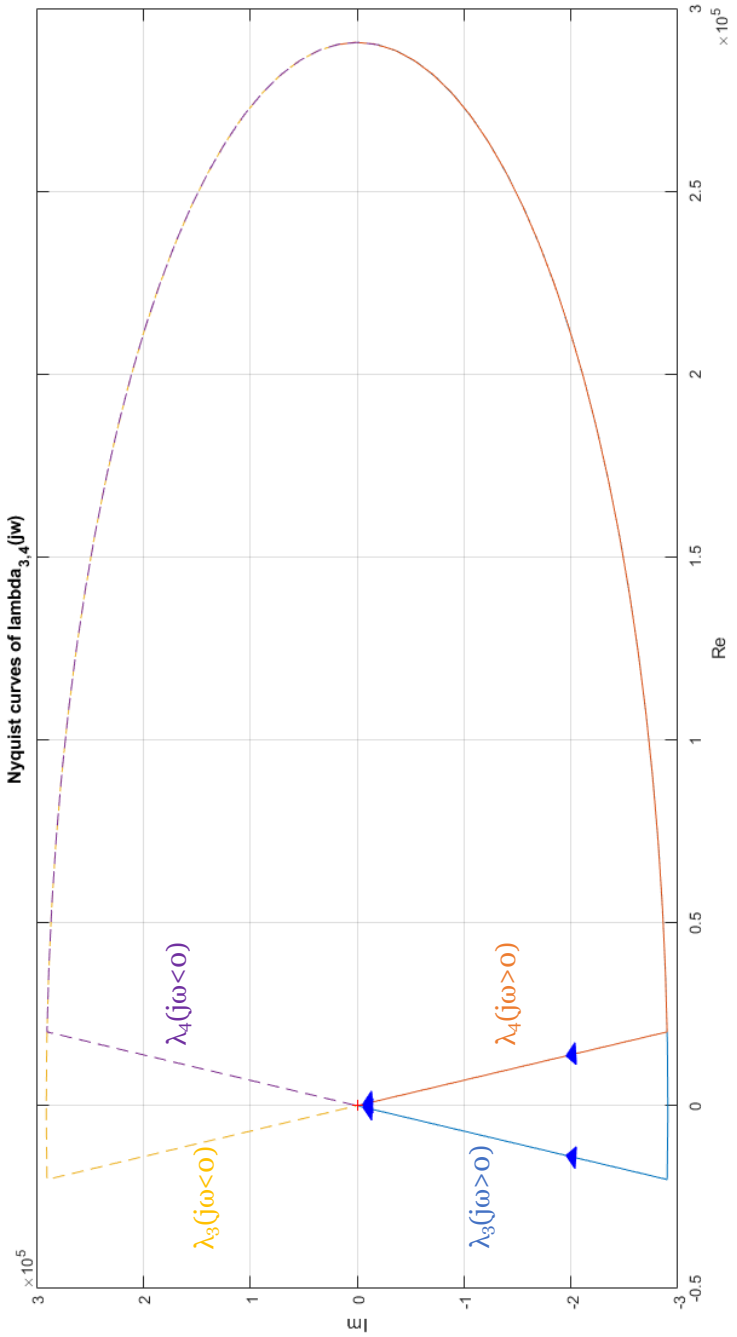

Figure 3.23 – Overall Nyquist diagram of the eigenvalues $\lambda_{3,4}(s)$

And zooming in the reduced region of interest:

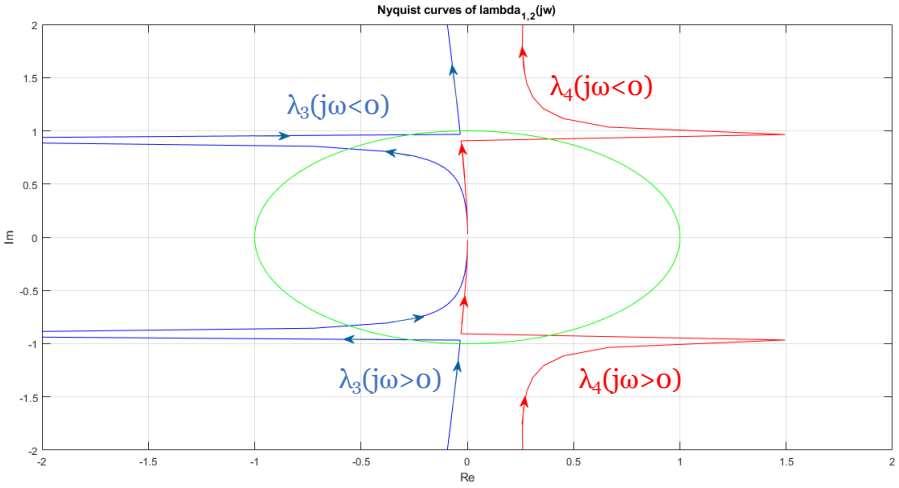

Figure 3.24 – Detailed Nyquist diagram of the eigenvalues $\lambda_{3,4}(s)$ (a)

Looking at Figure 3.24, it is possible to note that the phase margin for the voltage regulator φ_{m_v} is lower than 80°, which is the value chosen to design the regulator with the first method.

Adopting the same method as for the inner regulator, the real phase margin of 80° is obtained by changing the regulators parameters $k_{P_v} = 0.0029\ \Omega^{-1}$, $k_{I_v} = 0.0634\ \Omega^{-1}/s$.

The optimum values that increase the phase margin up to 80° are $k_{P_v} = 0.0032\ \Omega^{-1}$, $k_{I_v} = 0.006\ \Omega^{-1}/s$, corresponding to a cut-off angular frequency $\omega_{c_v} = 300 \div 400\ rad/s$.

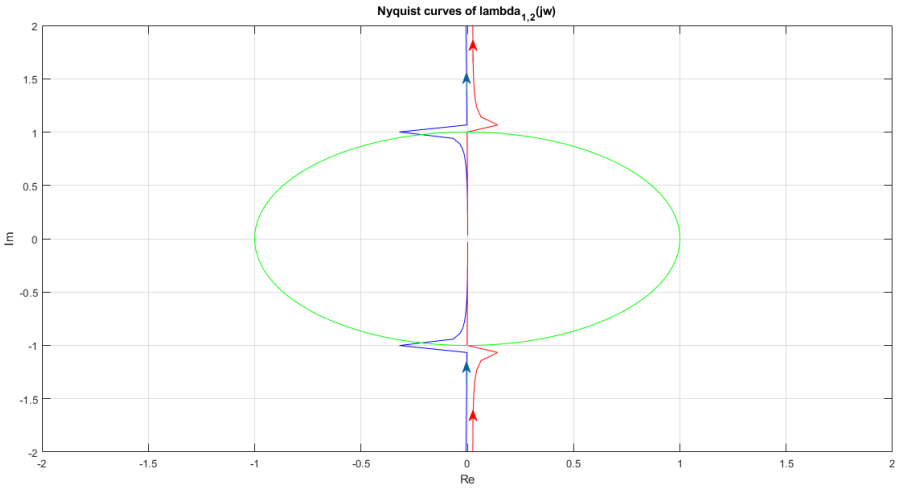

Figure 3.25 – Detailed Nyquist diagram of the eigenvalues $\lambda_{3,4}(s)$ (b)

The hypothesis of considering unitary the gain represented by the inner closed loop transfer matrix $K_{i_{\alpha\beta}}(s)$ results to be not valid: indeed, this approximation is reasonable only if the bandwidth of the inner control loop is significantly higher than the one of the outer control loop. In our case, it is found that $\omega_{c_i} \approx \omega_{c_v} = 300 \div 400\, rad/s$; besides, the parameters of the regulators are considerably lower with respect to the values found in SISO systems analysis. The effect of this choice is a high delay in the system response, as it will be demonstrated in the simulations of section 4.2.

Discarding the previous hypothesis, we try to evaluate the new expression of the outer open loop transfer matrix $L_{v_{\alpha\beta}}(s)$, considering $K_{i_{\alpha\beta}}(s)$ not unitary:

$$L_{v_{\alpha\beta}}(s) = \frac{1 + s\, R_d C_f}{sC_f} K_{i_{\alpha\beta}}(s) PI_{v_{\alpha\beta}}(s) \tag{3.39}$$

where $K_{i_{\alpha\beta}}(s) = \left[I + L_{i_{\alpha\beta}}(s)\right]^{-1} L_{i_{\alpha\beta}}(s)$ can be represented as:

$$K_{i_{\alpha\beta}}(s) = \begin{bmatrix} K_{i_{\alpha\beta}11}(s) & K_{i_{\alpha\beta}12}(s) \\ K_{i_{\alpha\beta}21}(s) & K_{i_{\alpha\beta}22}(s) \end{bmatrix} \tag{3.40}$$

Therefore:

$$L_{v_{\alpha\beta}}(s) = \frac{1 + s\,R_d C_f}{sC_f}\begin{bmatrix} K_{i_{\alpha\beta}11}(s) & K_{i_{\alpha\beta}12}(s) \\ K_{i_{\alpha\beta}21}(s) & K_{i_{\alpha\beta}22}(s) \end{bmatrix} PI_{v_{\alpha\beta}}(s) \tag{3.41}$$

The eigenvalues $\lambda_{3,4}(s)$ associated to the new representation open loop transfer matrix $L_{v_{\alpha\beta}}(s)$ give rise to a new Nyquist diagram, evaluated in the region of interest:

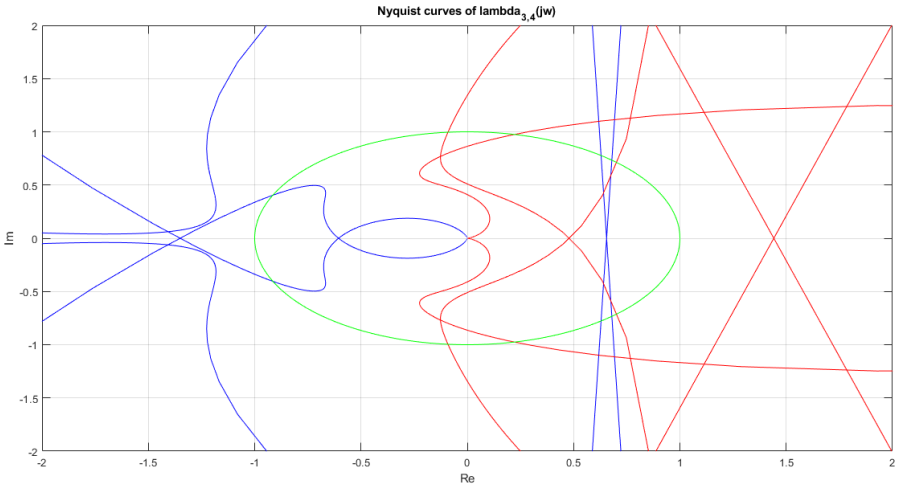

Figure 3.26 – Detailed Nyquist diagram of the eigenvalues $\lambda_{3,4}(s)$ (c)

The Nyquist diagram demonstrates the instability of the system, because the critical point -1+j0 is encircled many times. Therefore, in these conditions, it is not possible to evaluate the phase margin and the regulator's parameters associated.

CHAPTER 4
SIMULATIONS

In this chapter tests and simulations in MATLAB/Simulink environment about the systems described in the previous chapters are presented and commented, supporting what is written in theory.

4.1 Three-phase four-wire Inverter

The model of the system with the three-phase four-wire inverter of Chapter 1 is implemented in Simulink as shown in Figure 4.1:

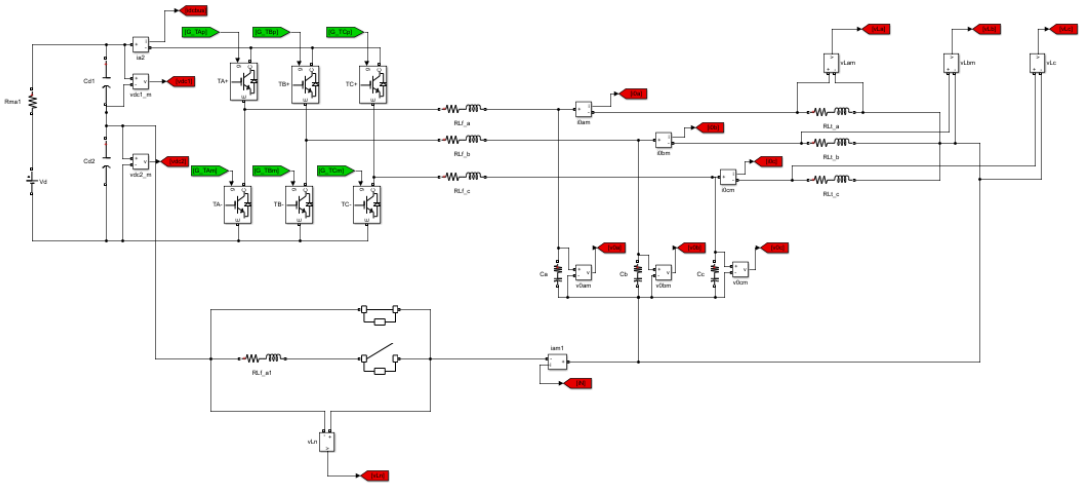

Figure 4.1 – Three-phase four-wire inverter configuration system's model in Simulink

As already said, for this case a simple PWM modulation with ideal carrier signals is adopted, focusing the attention on the role of the neutral inductance.

The three-phase unbalanced load is characterized by the following parameters, considering Table 1.1:

Phase a:

$R_{la} = 0.8 * R_l$

$L_{la} = 0.8 * L_l$

Phase b:

$R_{lb} = R_l$

$L_{lb} = L_l$

Phase c:

$R_{la} = 0.6 * R_l$

$L_{la} = 0.6 * L_l$

The most common index used to that defines the level of unbalance is the **Voltage Unbalance Factor (VUF)** by IEC [20], which is the ratio between the negative and the positive sequence voltage components, obtained by the well-known symmetrical component transformation introduced by Fortescue's Theorem.

$$\% VUF = \frac{|\bar{V}_n|}{|\bar{V}_p|} * 100 \tag{4.1}$$

Where:

$$\begin{cases} \bar{V}_p = \frac{1}{3}(\overline{V_{oa}} + \alpha\overline{V_{ob}} + \alpha^2\overline{V_{oc}}) \\ \bar{V}_n = \frac{1}{3}(\overline{V_{oa}} + \alpha^2\overline{V_{ob}} + \alpha\overline{V_{oc}}) \end{cases} \tag{4.2}$$

Whit $\alpha = e^{j\frac{2}{3}\pi}$.

IEC standards (the IEC 1000-3-x series) give limits for the unbalance ratio, defined by (4.1), to be less than 2% for Low and Medium voltage systems and less than 1% for high voltage systems measured as 10-minute values. An instantaneous maximum value of 4% is allowed [20].

Case 1:

In this case the inductor on the neutral wire is not present. The waveforms of the quantities analysed are reported in the following figures.

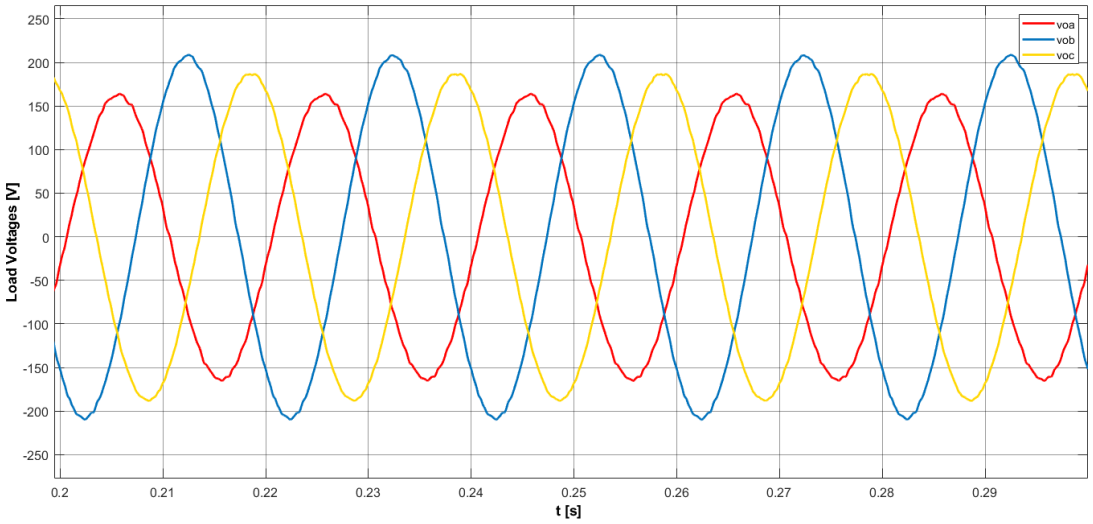

Figure 4.2 – Load voltages without neutral inductor (Case 1)

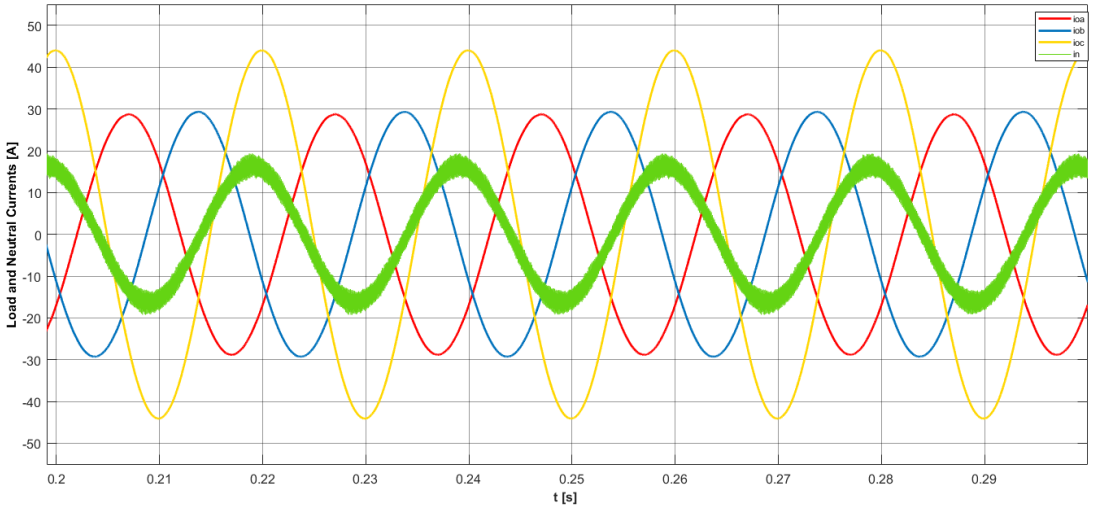

Figure 4.3 – Load and neutral currents without neutral inductor (Case 1)

As is possible to see, the unbalance involves both the voltage and current; the Voltage Unbalanced Factor is:

$$\% \, VUF = \frac{|\bar{V}_n|}{|\bar{V}_p|} * 100 = 2.2 \, \% \tag{4.3}$$

which is out of limits for Low and Medium voltage grids.

The block scheme implemented in Simulink to computer the VUF is reported in Figure 4.4:

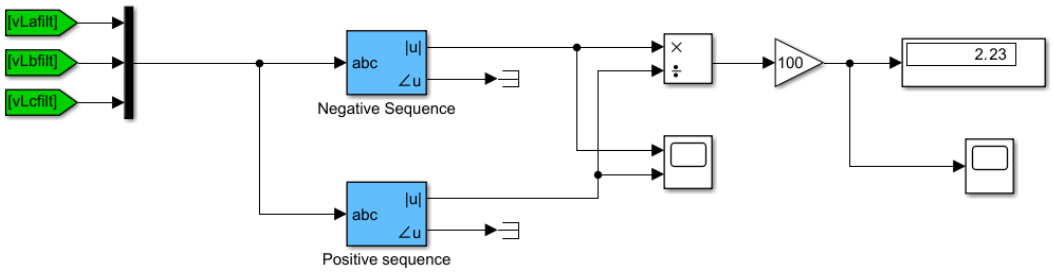

Figure 4.4 – Simulink block scheme for the computation of the VUF

Case 2:

In this case the inductor is present. The waveforms of the quantities analysed are reported in the following figures.

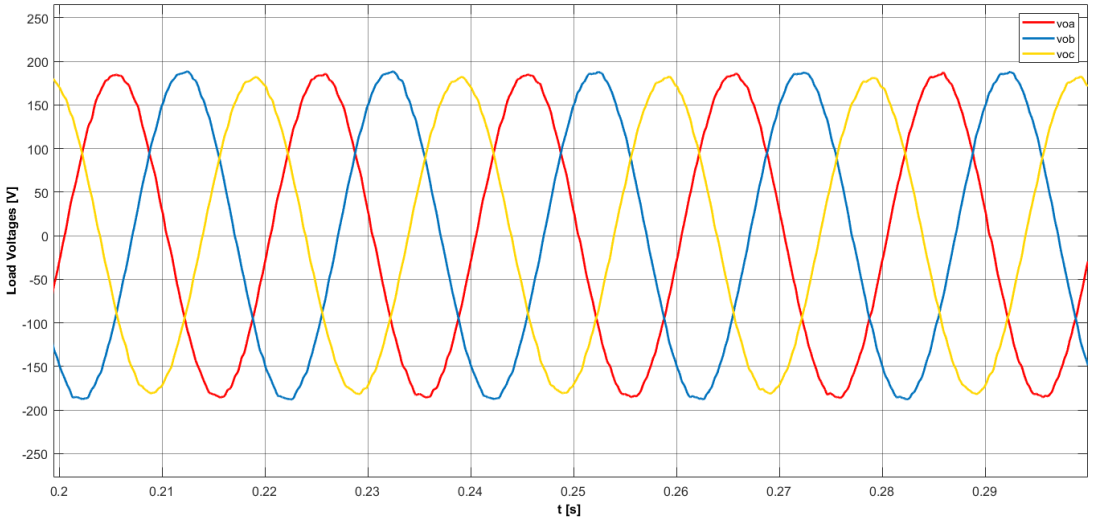

Figure 4.5 – Load voltages with neutral inductor (Case 2)

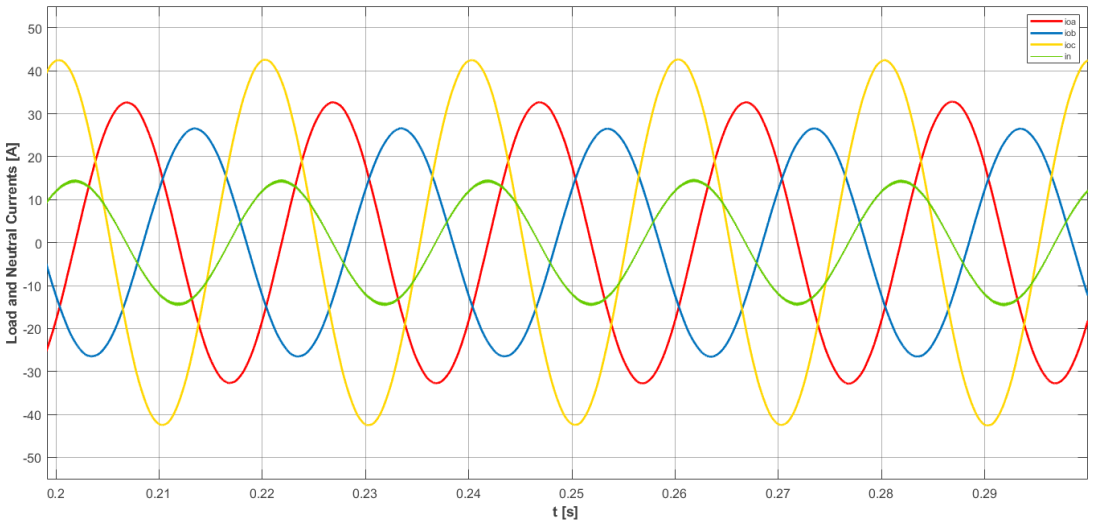

Figure 4.6 – Load and neutral currents with neutral inductor (Case 2)

In this case, the unbalance does not involve the load voltages: this means that the inductor on the neutral wire compensates the voltage drop across capacitors, making the three-phase load voltage system balanced. The Voltage Unbalance Factor is:

$$\%\, VUF = \frac{|\bar{V}_n|}{|\bar{V}_p|} * 100 = 1.8\,\% \tag{4.4}$$

which is within the limits defined by IEC standards.

Checking the waveforms of the voltages across the two capacitors C_{d1} and C_{d2} on the inverter's fourth wire:

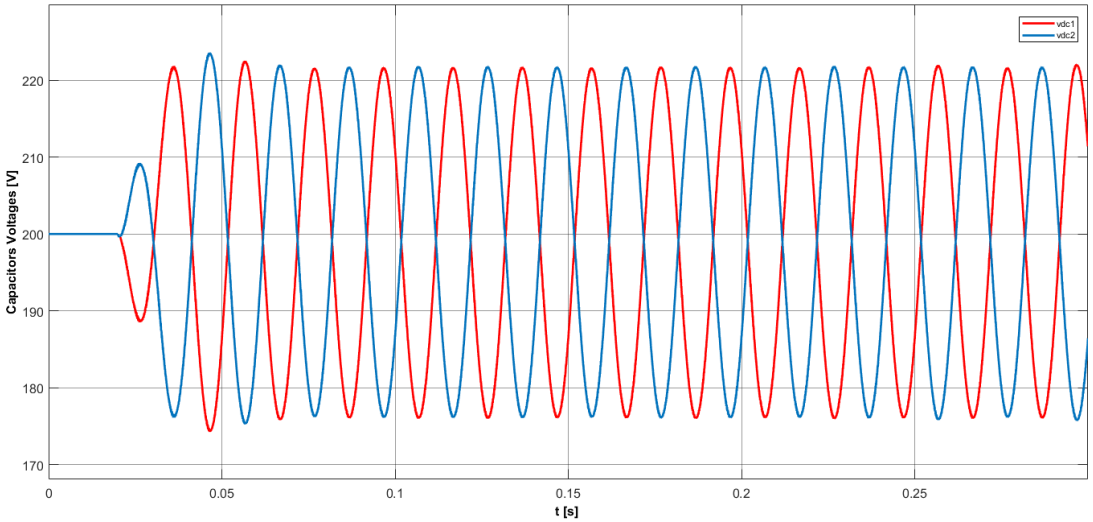

Figure 4.7 – Voltages across capacitors C_{d1} and C_{d2}

it is verified that the deviation from the supply voltage $V_{dc}/2 = 200\,V$ is of $\pm 10\,\%$, which is an acceptable result. Therefore, over voltages do not take place.

Case 3:

In this last example, the neutral wire topology shifts from the one of Case 1 to the one of Case 2, by means of breakers. The configuration can be seen in Figure 4.1, reported in detail below:

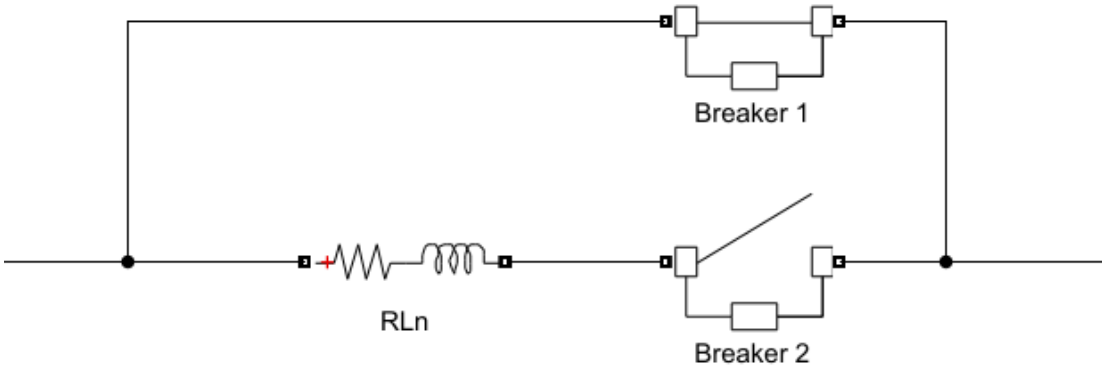

Figure 4.8 – Neutral wire detail (Case 3)

At $t = 0.15\,s$ Breaker 1 opens and Breaker 2 closes.

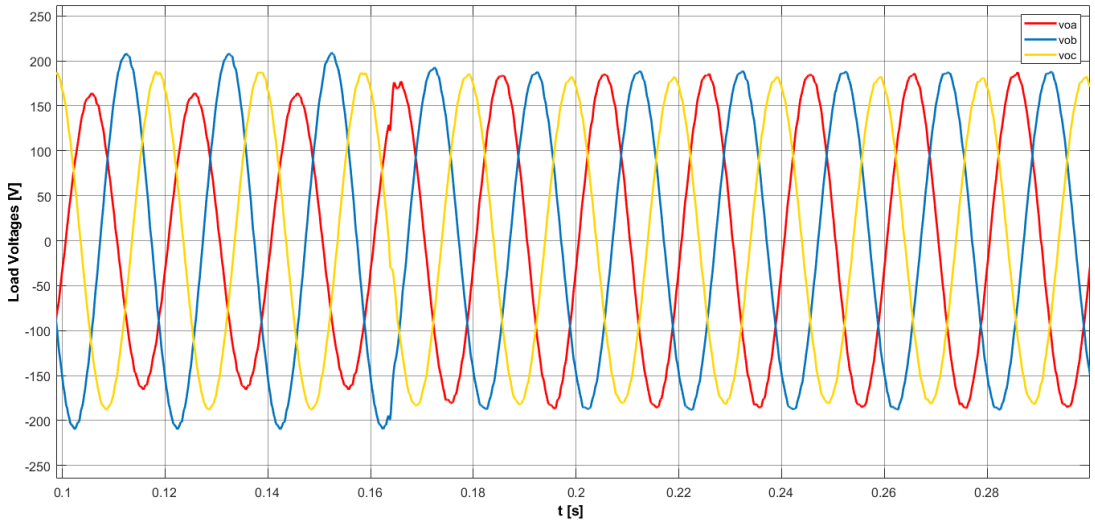

Figure 4.9 - Load voltages (Case 3)

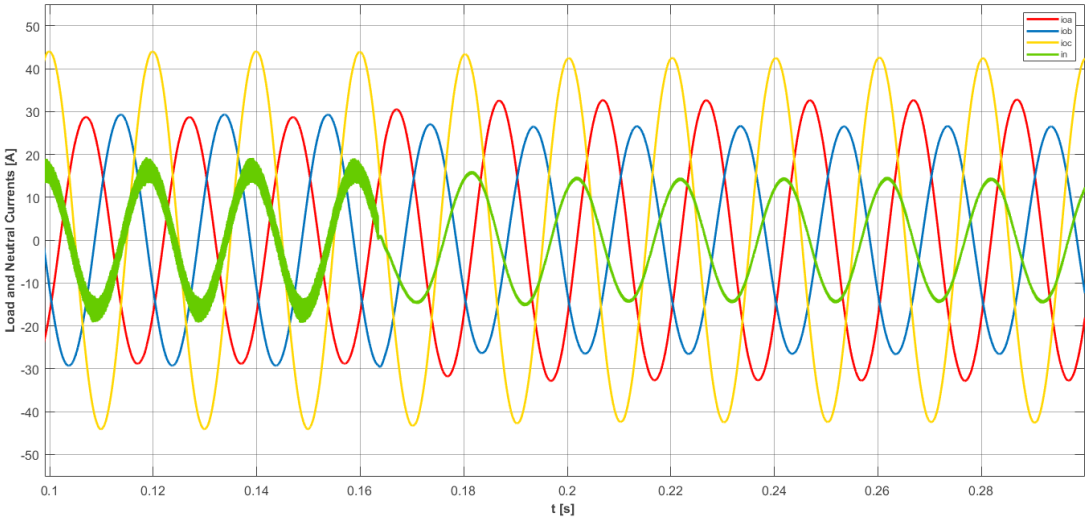

Figure 4.10 – Load and neutral currents (Case 2)

From Figure 4.9 and 4.10 it is even more clear the advantage of putting an inductor on the neutral wire, passing from an unbalanced load voltage system to a balanced one.

4.2 Three-phase four-leg Inverter

In this section, simulations in Simulink of the system presented in Chapter 2 are described. The model of the physical system is depicted in Figure 4.11.

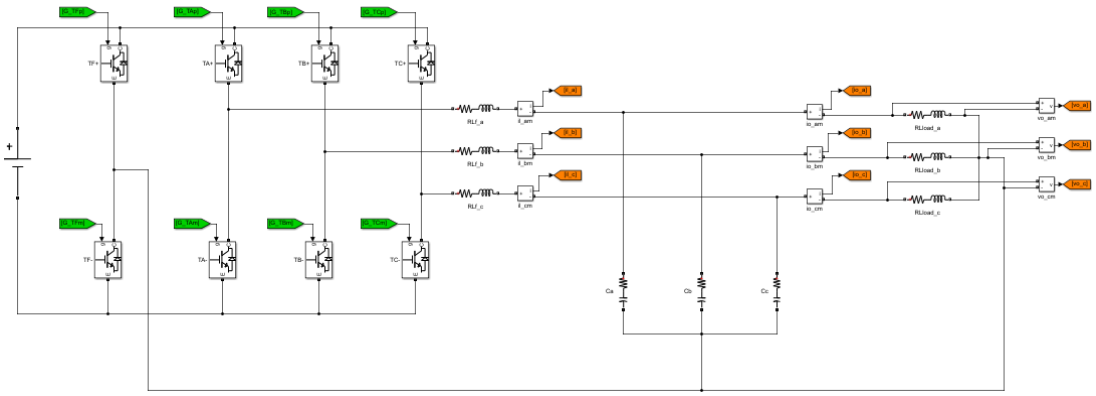

Figure 4.11 – Three-phase four-leg inverter configuration system's model in Simulink

The details of the control and modulation systems implemented are reported in Appendix A.

The three-phase unbalanced load is characterized by the following parameters:

$R_l = 14.3\ \Omega$

$L_l = 22\ mH$

which are load resistance and inductance values corresponding to an absorbed active power $P_l = 3\ kW$ with $\cos\varphi = 0.9$.

Phase a:

$R_{la} = R_l$

Phase b:

$R_{lb} = 0.8 * R_l$

Phase c:

$R_{la} = 0.6 * R_l$

Case 1:

In this case the design method for PI regulators is the traditional one for SISO systems, described in section 3.2.

The results of simulation are the following:

- *Load phase voltages v_{oa}, v_{ob}, v_{oc}*

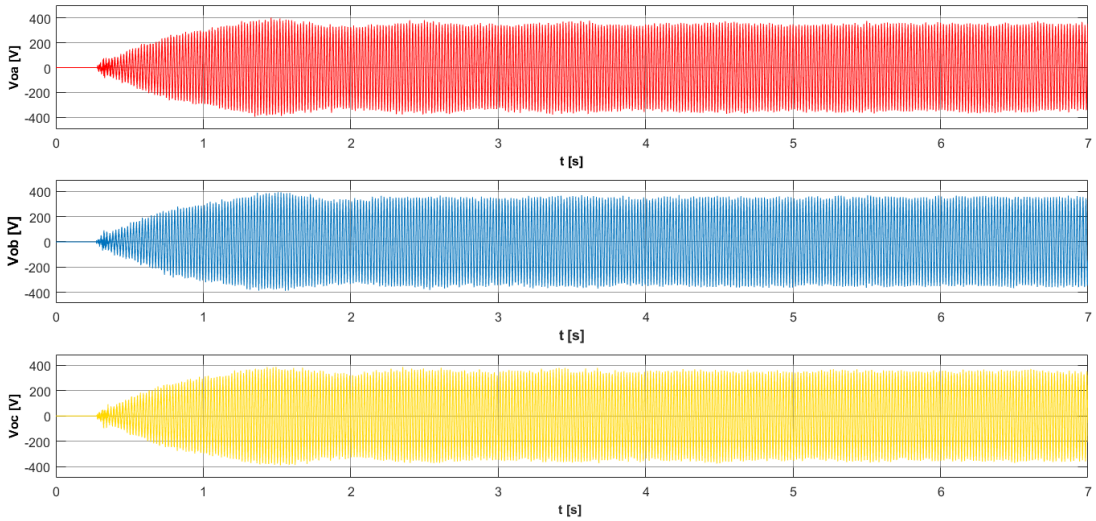

Figure 4.12 – Load phase voltages v_{oa}, v_{ob}, v_{oc} (a) - (Case 1)

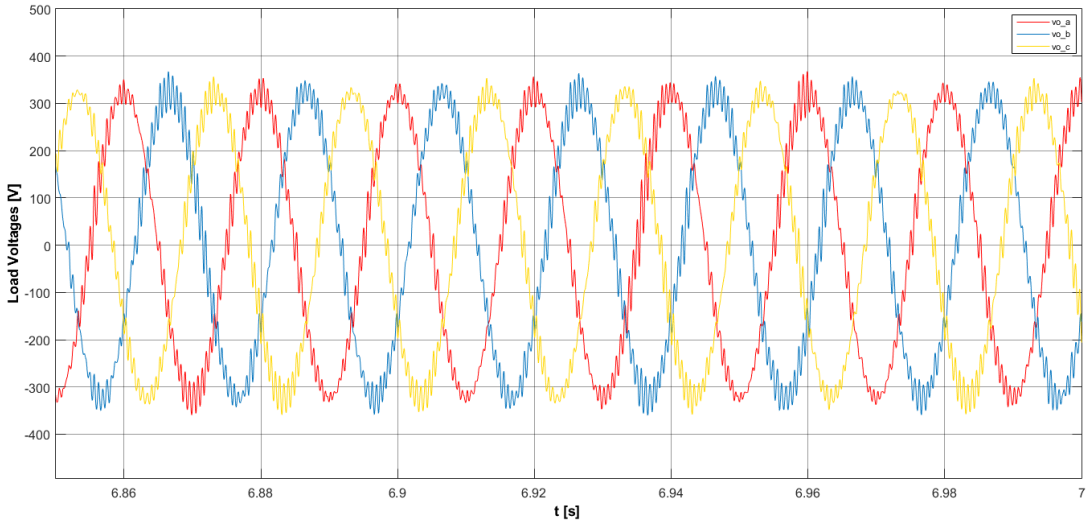

Figure 4.13 – Load phase voltages v_{oa}, v_{ob}, v_{oc} (b) - (Case 1)

- *Load phase currents i_{oa}, i_{ob}, i_{oc}*

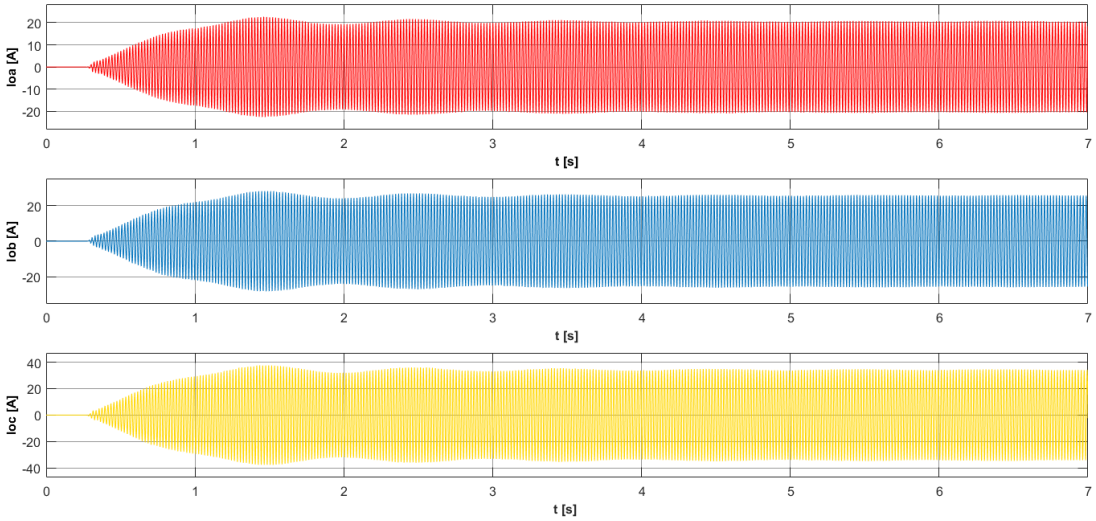

Figure 4.14 – Load phase currents i_{oa}, i_{ob}, i_{oc} (a) - (Case 1)

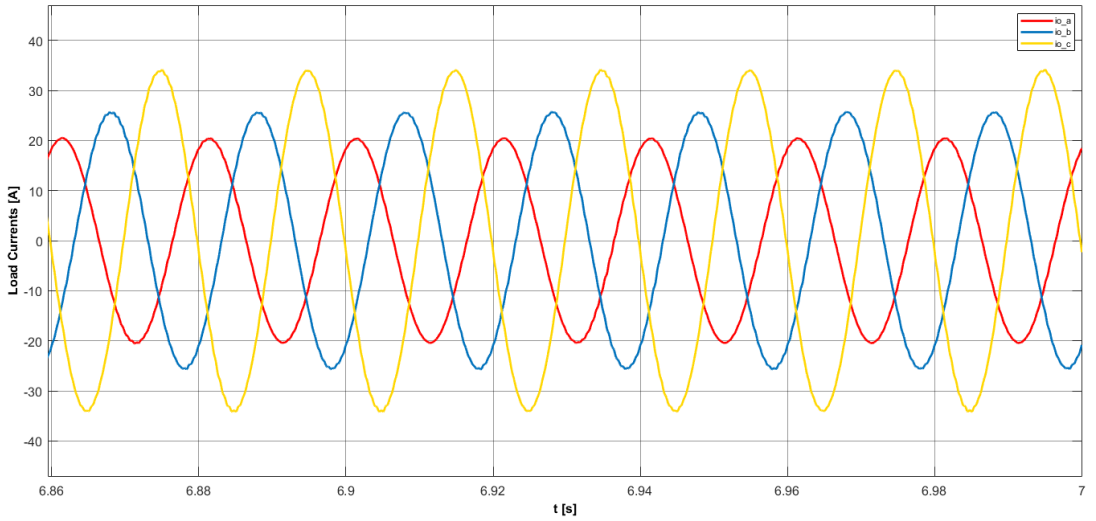

Figure 4.15 – Load phase currents i_{oa}, i_{ob}, i_{oc} (b) - (Case 1)

Looking at Figure 4.12 and 4.13, it is possible to note that the waveforms of voltages and currents are characterized by an oscillatory profile in the first instants of the simulation; these oscillatory trends finish after 5 seconds, reaching stable final conditions.

Figure 4.13 and 4.15 show the detailed profiles of voltages and currents when oscillations are passed; note that, despite the unbalanced load configuration,

the three-phase load voltage system is symmetric and balanced, validating the correct operation of the control and modulation system described in theory. Below, the waveforms of load voltages and currents on *αβ* axes for phase *a* are shown:

- *Load phase voltages on αβ axes* v_{oa_α}, v_{oa_β}

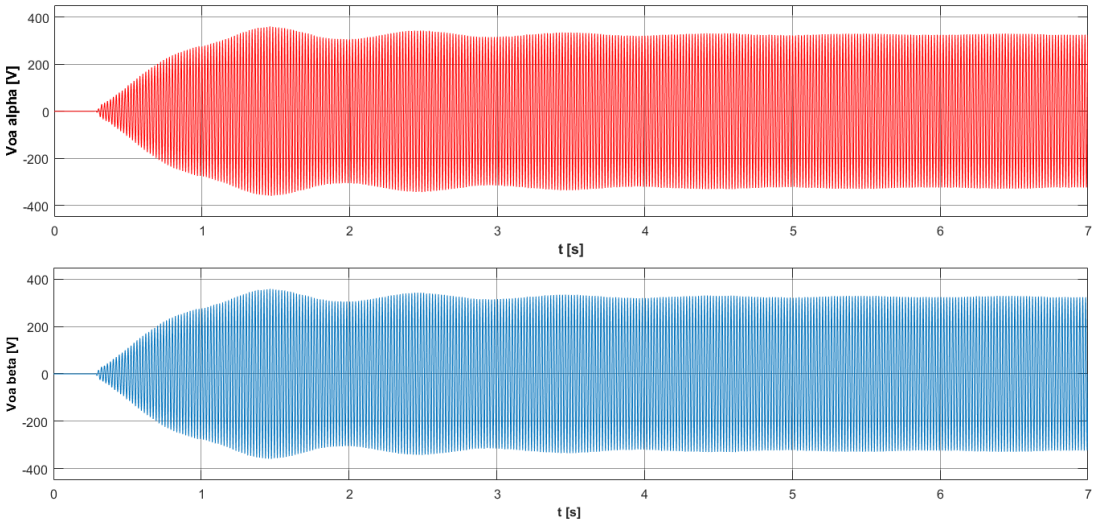

Figure 4.16 – Load phase voltages on αβ axes v_{oa_α}, v_{oa_β} (a) - (Case 1)

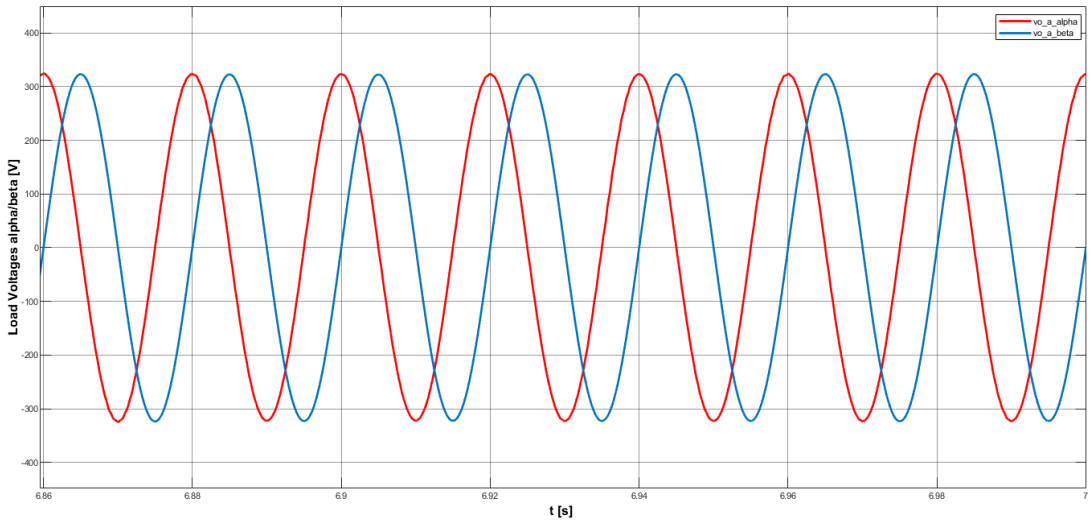

Figure 4.17 – Load phase voltages on αβ axes v_{oa_α}, v_{oa_β} (b) - (Case 1)

- *Load phase currents on αβ axes i_{oa_α}, i_{oa_β}*

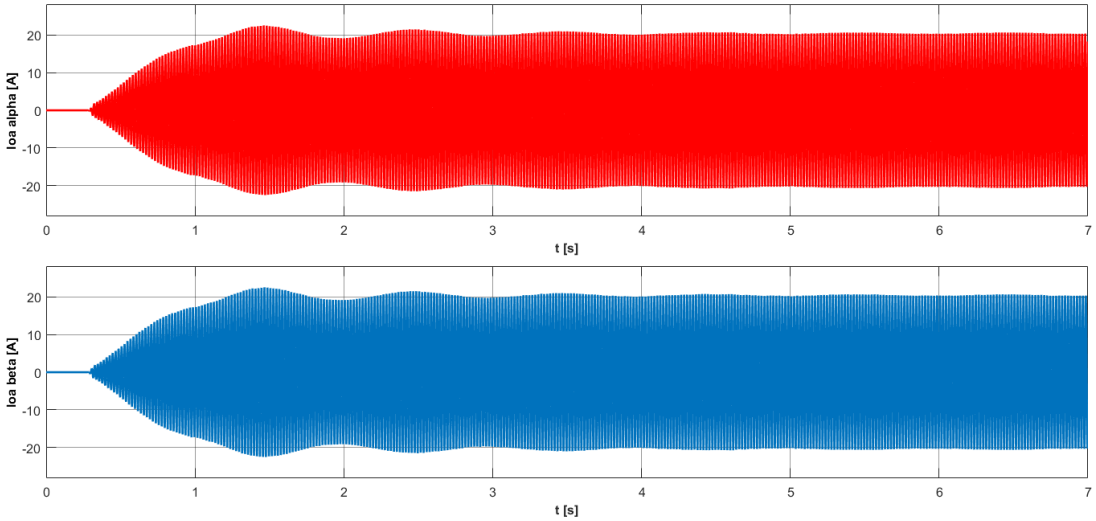

Figure 4.18 – Load phase currents on αβ axes i_{oa_α}, i_{oa_β} (a) - (Case 1)

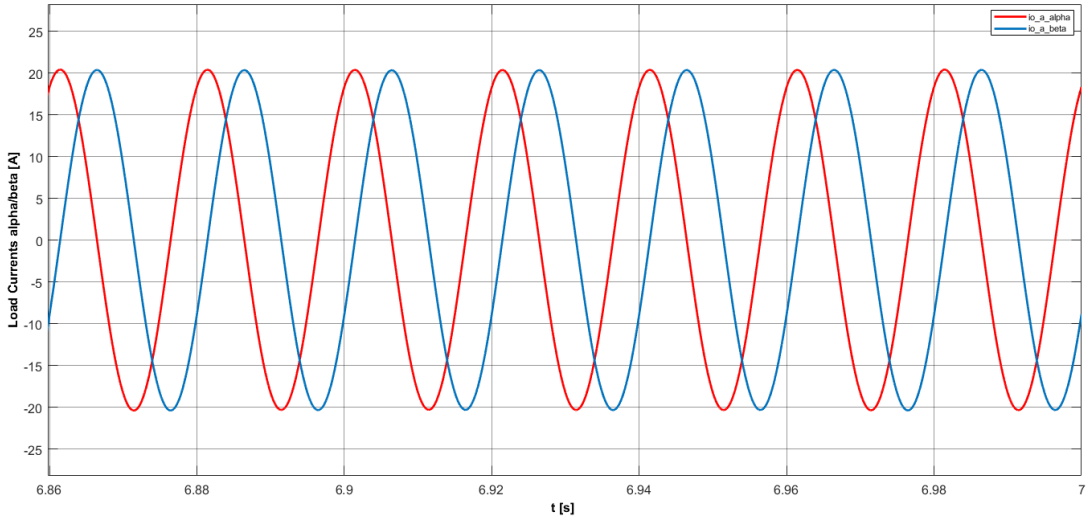

Figure 4.19 – Load phase currents on αβ axes i_{oa_α}, i_{oa_β} (b) - (Case 1)

The same observations about the initial oscillatory responses can be done.

Finally, in Figure 4.20 and 4.21 it is possible to see the load voltage and current profiles on *dq* axes for phase *a*, confirming what is shown on *abc* and *αβ* components:

- *Load phase voltages on dq axes* v_{oa_d}, v_{oa_q}

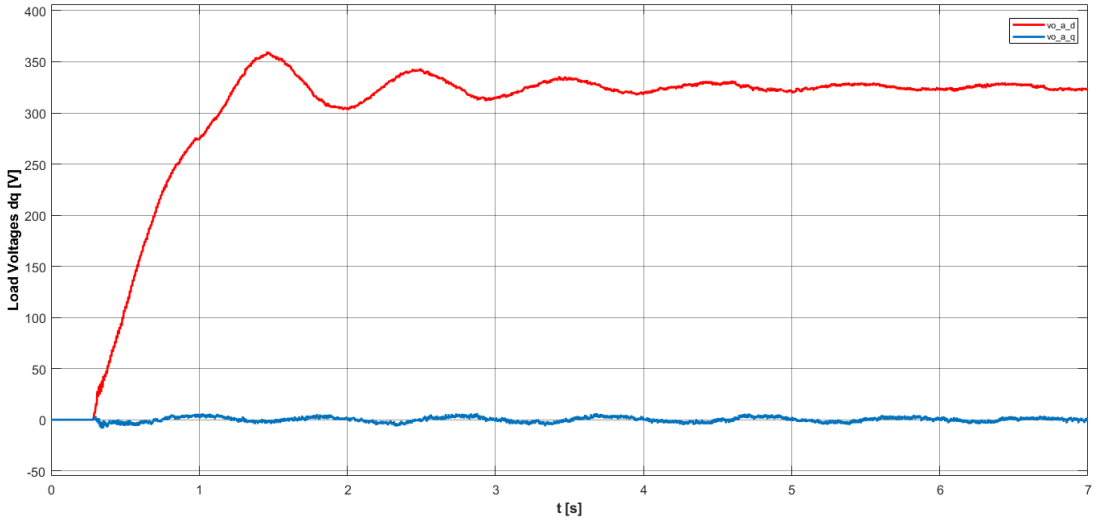

Figure 4.20 – Load phase voltages on dq axes v_{oa_d}, v_{oa_q} (Case 1)

- *Load phase currents on dq axes* i_{oa_d}, i_{oa_q}

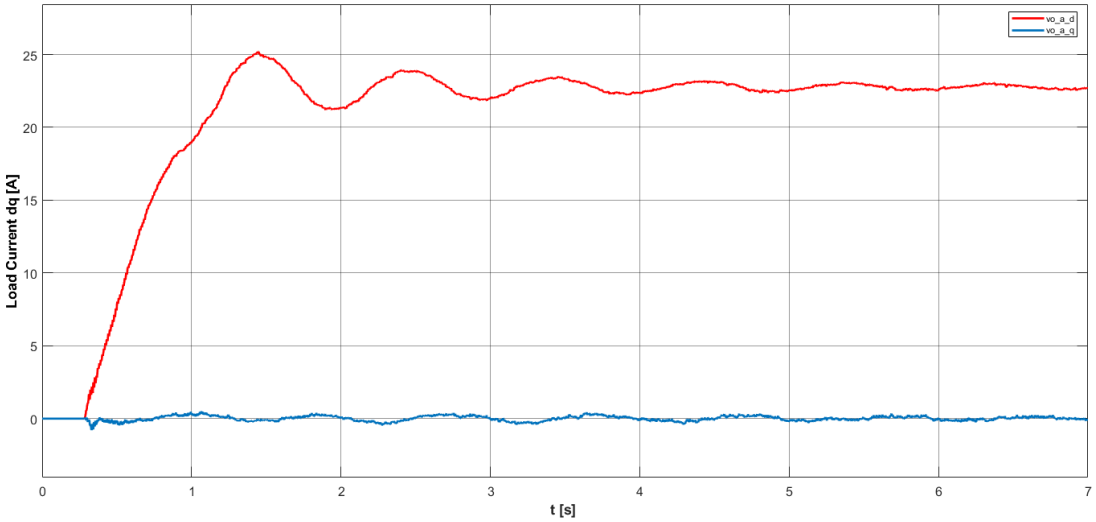

Figure 4.21 – Load phase currents on dq axes i_{oa_d}, u_{oa_q} (Case 1)

The initial oscillatory profile stands out more when the voltage and current signals on direct axis are compared with their reference signal in the voltage/current control loop:

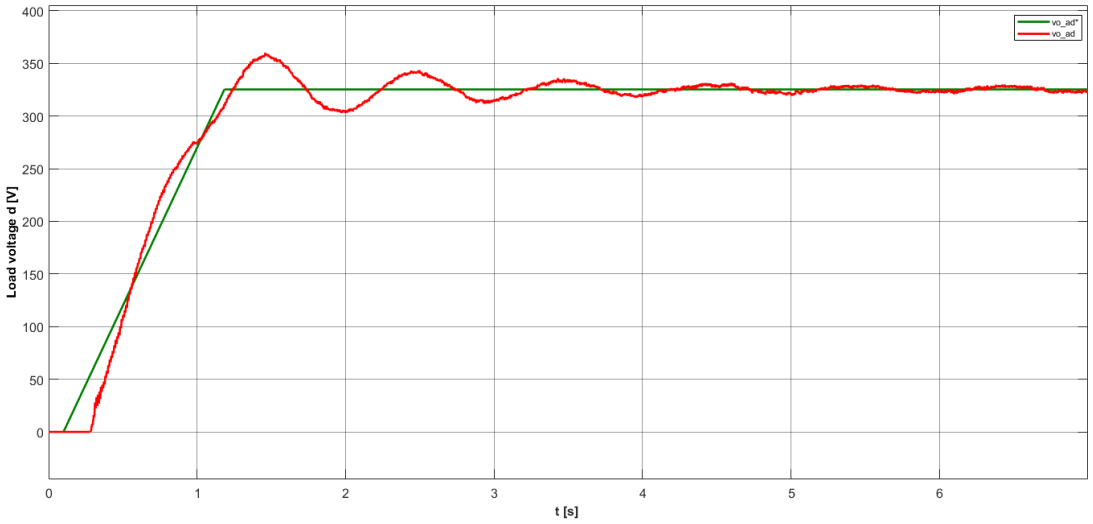

Figure 4.22 – Load voltage on direct axis compared with the reference signal (Case 1)

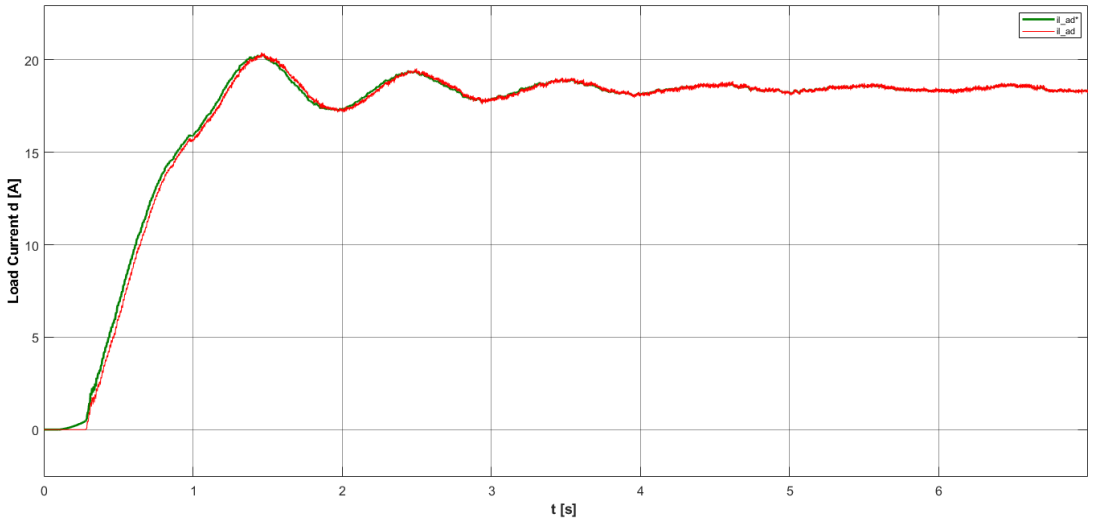

Figure 4.23 – Load current on direct axis compared with the reference signal (Case 1)

Case 2:

In this case the design method for PI regulators is the one adopted for MIMO systems, described in section 3.3.

The results obtained are not satisfactory, as expected from the observations done in the previous chapter. It is sufficient to see the voltage and current profile on *d* axis compared with their reference signals:

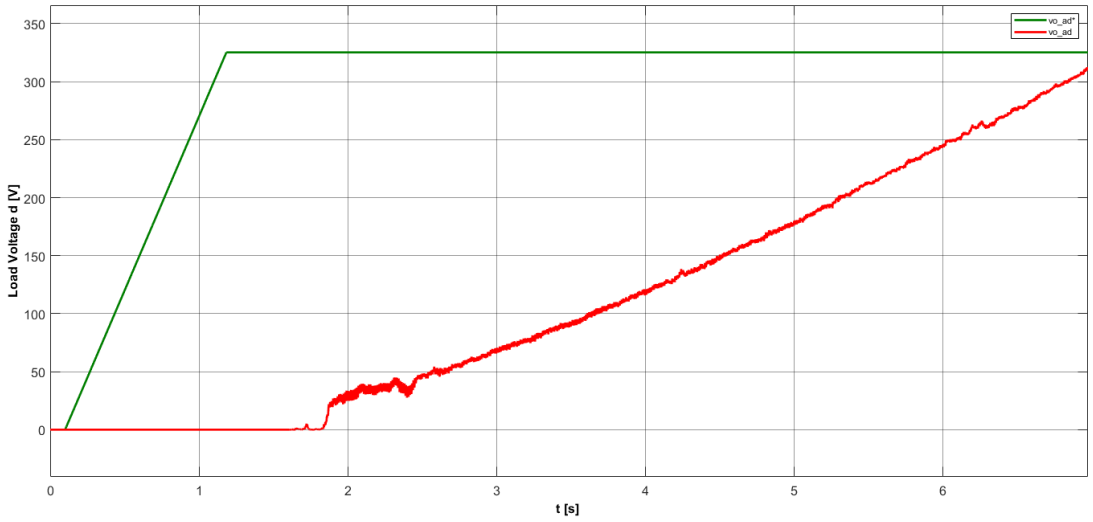

Figure 4.24 – Load voltage on direct axis compared with the reference signal (Case 2)

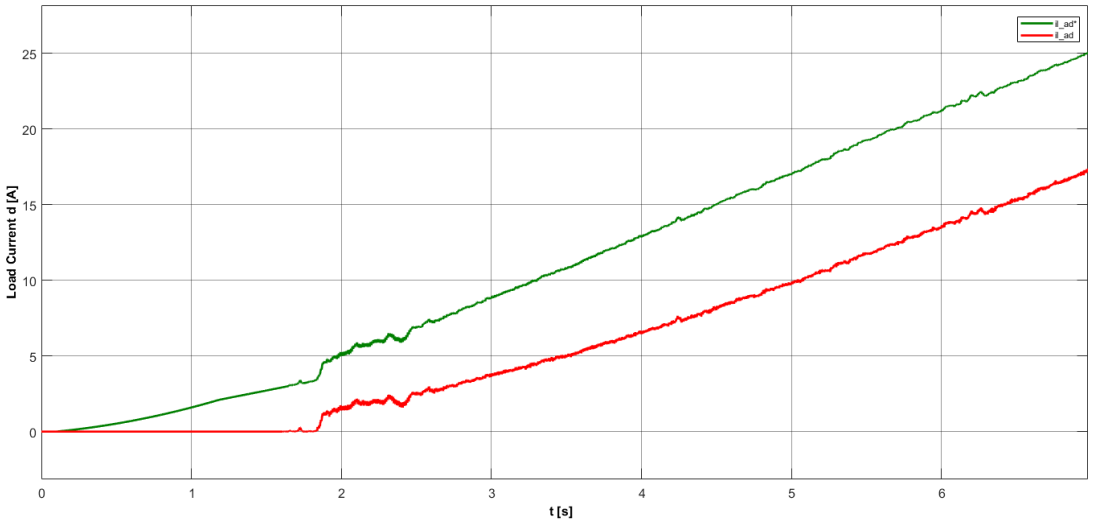

Figure 4.25 – Load current on direct axis compared with the reference signal (Case 2)

Although there are no oscillations with respect to Case 1, which was the goal fixed with the MIMO systems analysis, the system response is considerably

delayed; moreover, looking at Figure 4.25, the error between current and its reference signal is not zero.

Re-examining the analysis done for MIMO systems in section 3.3, the reasons for these results is imputable to the reduction of the bandwidth for the regulators: indeed, changing the regulators' parameters in order to obtain the desired phase margins, the bandwidth of the inner regulators is reduced of 5 times passing from the first design method to the new one, inevitably delaying the response of the system. In addition, it is supposed that the gain of the closed loop transfer matrix $K_{i_{\alpha\beta}}(s)$ is unitary for simplification: this statement is valid if the bandwidth of the outer loop is considerably lower than the inner loop's one, but it is found that they are more or less similar ($\omega_{c_i} \approx \omega_{c_v} = 300 \div 400\, rad/s$); a steady-state error different than zero in Figure 4.25 is justified by the analysis of the singular values.

CHAPTER 5
CONCLUSIONS

In this thesis, an analysis on three-phase inverters feeding unbalanced loads has been conducted, starting from the study of the possible converters' topologies employable for such a scenario up to the analysis of their critical issues in operating conditions.
The goal was to find a solution to the unbalance, which constitutes an undesired condition for the grid and loads themselves.

Two kind of inverters have been identified: the three-phase four-wire inverter and the three-phase four-leg inverter.

The study of the four-wire configuration has put the attention to the role of an inductors on the neutral wire, able to compensate the behaviour of the fourth leg 's capacitors and guaranteeing the rise of symmetric and balanced voltages across the loads.

The analysis of the four-leg topology has been focused on the control scheme of the system, and particularly on the PI regulators design. A per-phase *dq* control has been adopted, employing a Second Order Generalized Integrator for passing from single-phase to the fixed reference frame $\alpha\beta$; the control loops have been realized on *dq* axes, characterized by an inner current and an outer

voltage loop. A substantial part of the study has been covered by the design methods adopted for the regulators.

The first technique employed was the traditional one, used for the majority of the controllers; the oscillatory behaviour of the voltage and current profiles pushed to search for an alternative analysis, considering the system no more as SISO but as MIMO, considering the presence of the complex transfer function represented by the SOGI.

This change has brought to analyse definitions, theorems and criterions referred to multivariable systems, which are more complex with respect to all that is associated to single variable systems.

After dimensioning the controllers with the new methods, the results obtained in simulations have not been satisfactory: the improvements obtained in certain directions have been followed by degradations under other perspectives. These observations lay the foundation for further deeper analyses and developments.

Bibliography

[1] **N.A. Ninad, L.A.C. Lopes** – "Per-phase vector control strategy for a four-leg voltage source inverter operating with highly unbalanced loads in stand-alone hybrid systems" – Electrical Power and Energy Systems 55 (2014): 449-459.

[2] **E. Ortjohann, A. Mohd, N. Hamsic, M. Lingemann** – "Design and experimental investigation of space vector modulation for three-leg four-wire voltage source inverters" – Proceding of 13th IEEE European Conference on Power Electronics and Applications (EPE '09), 8-10 September 2009, pp. 1-6.

[3] **M. Monfared, H. Rastegar** – "Design and experimental verification of a dead beat power control strategy for low cost three phase PWM converters" – International Journal of Electrical Power & Energy Systems, Volume 42, Issue 1, November 2012, Pages 418-425.

[4] **M.N. Marwali, A. Keyhani** – "Control of distributed generation systems – Part I: Voltages and currents control" – IEEE Trans Power Electron 2004;19(6):1541–50.

[5] **P. Li, B. Dan, K. Yong, C. Jian** – "Research on three-phase inverter with unbalanced load" – Proceeding of IEEE Applied Power Electronics Conference and Exposition (APEC '04), vol. 1, 2004, pp. 128–133.

[6] **D. Soto, C. Edrington, S. Balathandayuthapani, S. Ryster** – "Voltage balancing of islanded microgrids using a time-domain technique" – Electr Power Syst Res 2012;84(1):214–23.

[7] **N.A. Ninad, L.A.C. Lopes** – "Per-phase vector (dq) controlled three-phase grid-forming inverter for stand-alone systems" – Proceeding of 2011 IEEE International Symposium on Industrial Electronics (ISIE 2011), 27–30 June 2011, pp. 1626–1631.

[8] **M. G. Ubaldini** – "Reattori per la formazione del neutro" – Appunti del corso di Macchine Elettriche, Politecnico di Milano.

[9] **J.-H. Kim, S.-K. Sul** – "A carrier-based PWM method for three-phase four-leg voltage source converters – IEEE Transaction on Power Electronics, Volume 19, No. 1;19(1):66–75, January 2004.

[10] **F. Iliceto** – "Impianti Elettrici", Volume I – Pàtron Editore Bologna.

[11] **A. Bellini, S. Bifaretti** – "A simple control technique for three-phase four-leg inverters" – International Symposium on Power Electronics, Electrical Drives, Automation and Motion, 2006. SPEEDAM 2006.

[12] **E. Ozsoy, S. Padmanaban, P. Siano, F. Ahmad, R. Akhtar, A. Sabanovic, V. Loia** – "Instantaneous symmetrical component estimator using second order generalized integrator under distorted voltage conditions" – Preprints (www.preprints.org), May 2017.

[13] **M. Ciobotaru, R. Teodorescu, F. Blaabjerg** – "A new single-phase PLL structure based on second order generalized integrator" – 2006 37th IEEE Power Electronics Specialists Conference, 18-22 June 2006.

[14] **N.A. Ninad, L.A.C. Lopes** – "A vector controlled single-phase voltage source inverter with enhanced dynamic response" – 2010 IEEE International Symposium on Industrial Electronics, 4-7 July 2010.

[15] **B. Bahrani, A. Rufer, S. Kenzelmann, L.A.C. Lopes** – "Vector control of single-phase voltage-source converters based on fictive-axis emulation" – IEEE Transactions on Industry Applications, Volume 47, Issue 2, March-April 2011.

[16] **D.N. Zmood, D.G. Holems, G.H. Bode** – "Frequency-domain analysis of three-phase linear current regulators" – IEEE Transaction on Industry Application, Vol. 37, No. 2, March/April 2001.

[17] **J.M. Maciejowski** – "Multivariable Feedback Design" – Addison-Wesley, 1989.

[18] **Lennart Harnefors** – "Modeling of three-phase dynamic systems using complex transfer functions and transfer matrices" – IEEE Transactions on Industrial Electronics, Vol. 54, No. 4, August 2007.

[19] **L. Magni, R. Scattolini** – "Complementi di controlli automatici" – Pitagora Editrice Bologna, 2006.

[20] **M.H. Albadi, A.S. Al Hinai, A.H. Al-Badi, M.S. Al Riyami, S.M. Al Hinai, R.S. Al Abri** – "Unbalance in Power Systems - Case Study" – Researchgate, June 2015.

[20] www.mathworks.com, Documentation.

APPENDIX A
FOUR-LEG INVERTER IMPLEMENTED SYSTEM

In this Appendix the models developed in MATLAB/Simulink environment for the four-leg inverter configuration are illustrated and described, for the purposes of the tests and simulations presented in Chapter 4.

A.1 Overview

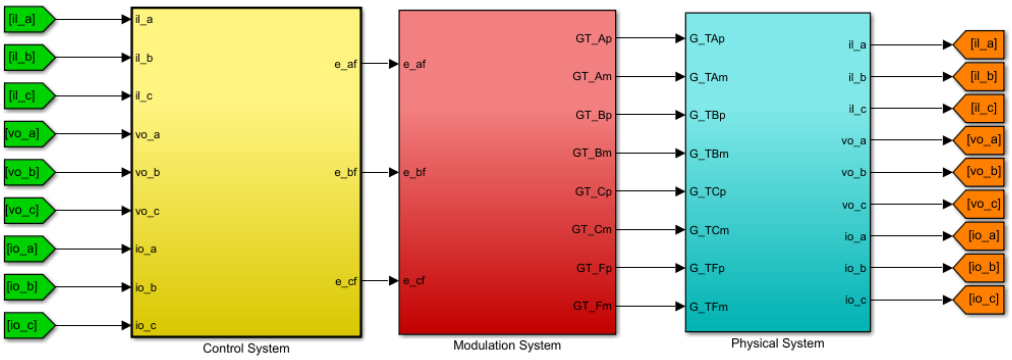

Figure A. 1 – Implemented system's structure overview

Figure A.1 provides an overview of how the implemented system is structured:

- **Physical System:** it is the block that contains all the physical elements; here there are the voltage source, the inverter, the LC filter

and the loads. Indeed, all the voltages and currents involved in the control are measured and sent to the Control System itself;

- **Control System:** in this part of the system, the quantities received from the physical system are processed and involved into the control loops; the output is represented by the three inverter's voltages, which are sent to the modulation system's block;
- **Modulation System:** here the modulation technique described in the paragraph 2.3 is implemented, generating the signal to control the opening and closing of the inverter's IGBTs.

A.2 Physical System

As already anticipated, the Physical System contains all the physical elements. Figure A.2 illustrates the scheme created in Simulink:

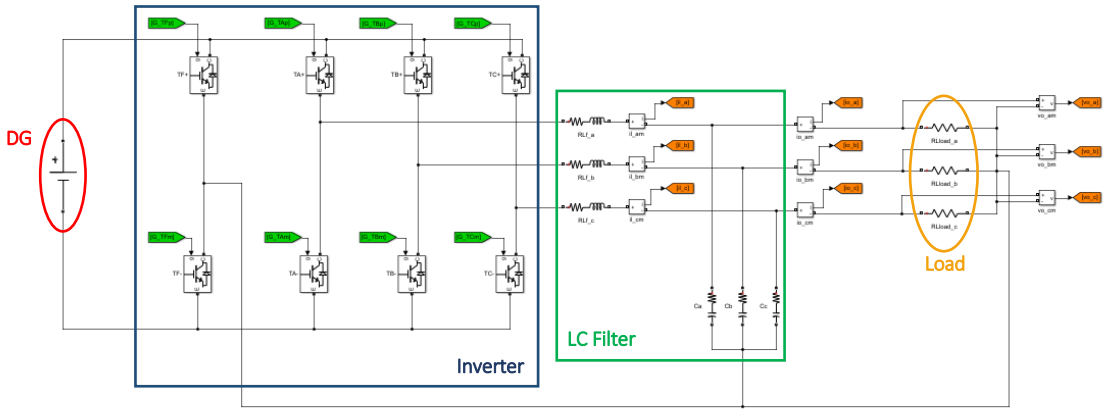

Figure A. 2 – Physical System implemented

From left to right we find:

- **DC Voltage Source:** it represents a DG unit (Distributed Generator);
- **Inverter:** it is the DC/AC interface converter, which connects the DG unit to the AC electrical grid;
- **LC Filter:** it is the filter necessary to face harmonics problem due to the inverter's output;

- **Load:** it represents some hypothetic users connected to the grid and fed by the DG.

It is possible to observe the presence of different Voltage and Current Measurement blocks, necessary in order to extrapolate the quantities needed in the control system.

The quantities measured are:

- **Inverter inductor currents:** *il_a, il_b, il_c;*
- **Load output currents:** *io_a, io_b, io_c;*
- **Load output voltages:** *vo_a, vo_b, vo_c;*

Note that the load output voltages coincide with the inverter capacitor voltages.

In the following paragraphs, each element is described in detail.

A.2.1 DC Voltage Source

The DC Voltage Source represents a DG unit that, in this specific case study, symbolizes a PV source, which supply the IGBT three-phase full bridge inverter.
Scrupulously, the DC Voltage Source implemented is a simplification of a wider conversion scheme. Indeed, usually the PV source supplies the inverter through a first DC/DC converter (or an AC/DC rectifier in case of AC sources) which stabilizes the voltage, whose terminals are connected to a **DC Link** constituted by a large capacitor. This allows to prevent a quick discharge of the capacitor and to make the voltage to the DC Link almost constant. The voltage across the DC Link is $V_{DC} = 800\ V$.

Despite this facilitation, the simplification adopted is acceptable for the purposes of tests and simulations to be carried out.

A.2.2 Inverter

The DC/AC converter is a **three-phase four-leg inverter**. The fourth leg is constituted by two additional power switches and provides the connection point for the neutral conductor, allowing the controllability of the neutral point also in case of high unbalanced loads.
The full bridge configuration is composed by four couple of IGBTs, one for each leg.

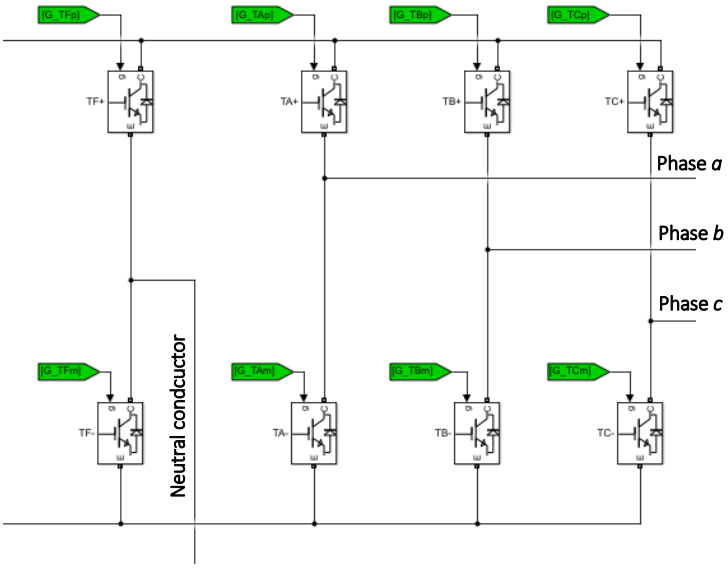

Figure A. 3 – Inverter's scheme implemented

The gate port of each IGBT receives a control signal from the Modulation System, which controls the opening and closing of the IGBT itself.
Below there is the table that summarizes the choices for the design of the converter.

Table A. 1 – Inverter's nominal data

Inverter type	IGBT/Diode 3-phase 4-leg inverter
Modulation	Carrier-based PWM
Switching Frequency f_{sw}	10 kHz
Rated Power A_n	10 kVA
Maximum Active Power P_n	10 kW
Maximum Reactive Power Q_n	10 kVar
DC side Voltage V_{DC}	800 V
Rated AC side Voltage V_n [rms]	230 V
Rated AC side Current I_n [rms]	14.5 A
Rated AC side angular Frequency ω_n	2π*50 rad/s

A.2.3 LC Filter

At the output of the inverter, a LC filter is placed in order to filter the high harmonic content due to the converter. Inductances and capacitances are modelled with their internal resistances, as computed in paragraph 2.1.2.

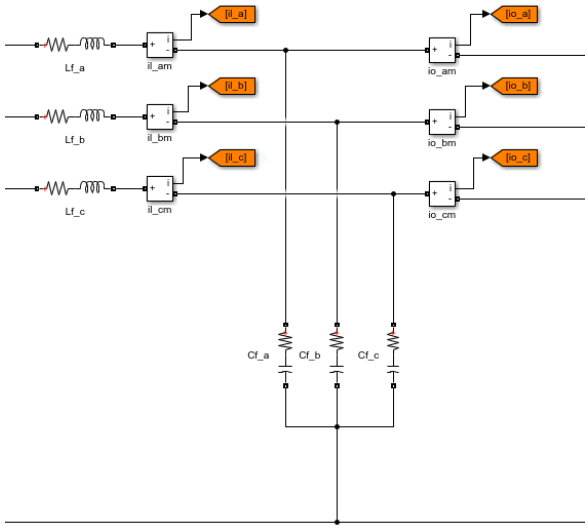

Figure A. 4 – LC Filter implemented

The filter is designed according to the following data:

Table A. 2 – LC Filter's design parameter

Filter inductance L_f	1 mH
Equivalent series resistance of the filter inductance R_f	5 mΩ
Voltage drop on L_f [p.u.]	0.02
Quality factor Q	20
Filter capacitance C_f	10 μF
Reactive power associated to filter capacitance	500 Var
Equivalent series resistance of the filter capacitance R_d	0.53 Ω

A.2.4 Load

The last element of the physical system is represented by a three-phase load, which is ohmic-inductive.

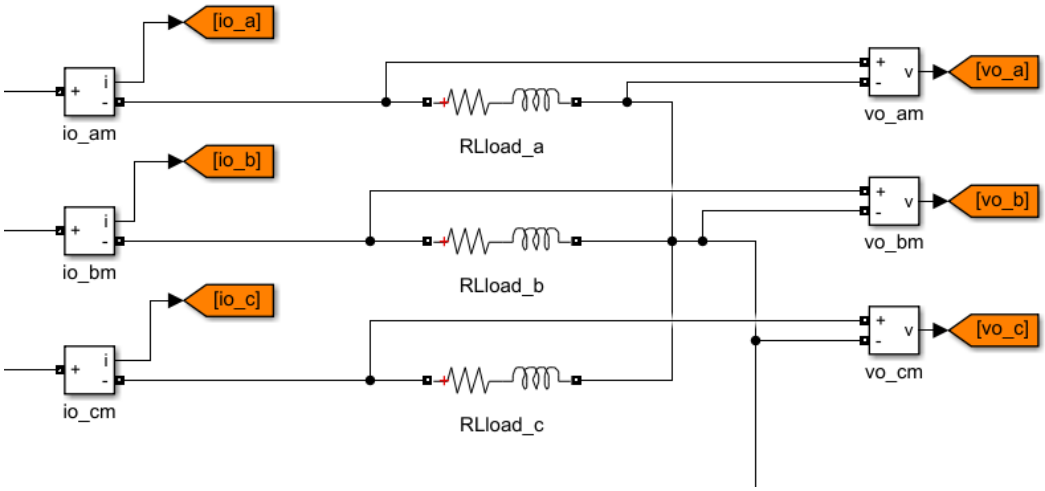

Figure A. 5 – Load implemented

A.3 Control System

The control system is the place where the physical quantities, voltages and current measured in the physical system, are subjected to various transformation to move from one reference system to another one in and processed through the control loops, applying the aforementioned **per-phase *dq* control.**

A.3.1 From single-phase to *dq* components

The first step in the control's process is characterized by the passage from the **single-phase quantities** to **rotating vectors** in the $\alpha\beta$ fixed reference frames, which lead to the determination of the two components α and β. This transformation is done by the **SOGI** which has been already explained in Chapter 2.

The α component coincides with the real single-phase input, while the β component is the relative orthogonal signal with the same magnitude as α.

In the system implemented in this work, each current and voltage passes through the transfer functions (2.16) and (2.17), generating the output pairs of signals.

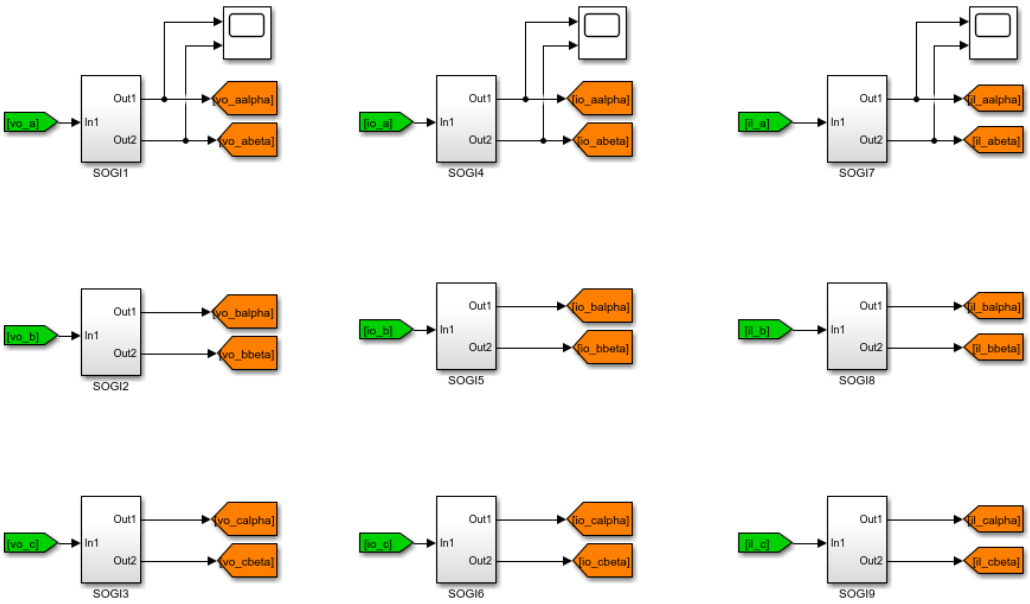

Figure A. 6 – SOGI systems implemented

In Figure A.6 it is possible to notice that also the inductor's currents are transformed into α and β components through the SOGI, in addition to the load's voltages and currents, differently from what is written in paragraph 2.2.4 where these currents are computed in $\alpha\beta$ frame through the FAE. This is because the simulation of the Fictive Axis Emulation technique in Simulink environment has bring the entire control system to unstable conditions. For these reasons, it has been chosen to apply the Second Order Generalized Integrator also to the output inverter inductor currents, that in any case give an acceptable response.

Below the characteristic parameters of the SOGI implemented are listed:

Table A. 3 – Parameters of the SOGI

Gain k_{SOGI}	1
Resonance angular Frequency ω_{SOGI}	2π*50 rad/s

The transition from the fixed reference frame $\alpha\beta$ to the rotating dq one and vice versa passes through the determination of the angle $\hat{\theta}$ between themselves, that allows to apply the Park and inverse Park transformations.

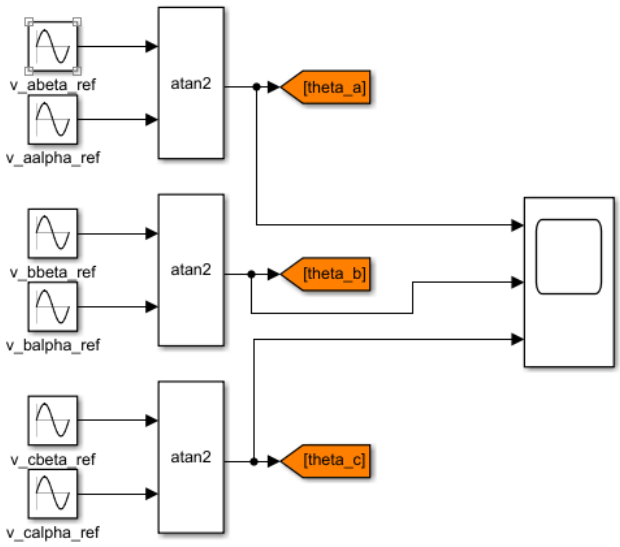

Figure A. 7 – Determination of θ angle for each phase

In our system this angle is computed through equation (2.27), which is exactly calculated as in Figure A.7: the input signal α and β are the reference voltage values of each phase, generating the angle as output using the "*atan2*" function [21].

Applying the Park transformation, the dq output quantities are finally computed and ready to be involved in the control loops.

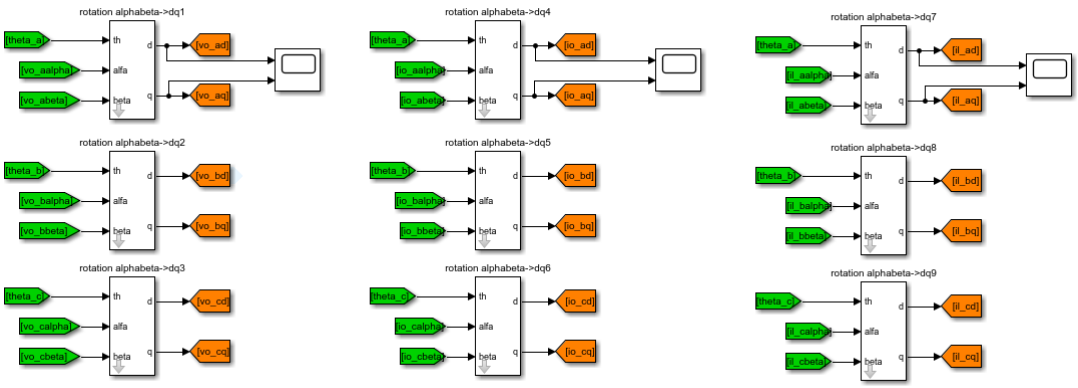

Figure A. 8 – Park transformation implemented

A.3.2 Control loops

Once obtained the *dq* components of voltages and currents, which in the rotating reference frame are seen as constants, they are sent to the control loops. In figure A.9, which illustrates the control implemented on *d* axis for phase *a*, it is possible to distinguish the **inner current control loop** *"PI_I"* in yellow, and the **outer voltage control loop** *"PI_V"* in blue.

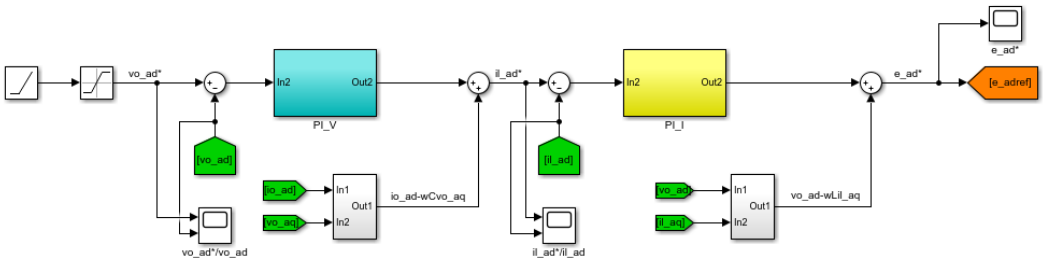

Figure A. 9 – Control loop implemented on *d* axes

The input of this system is constituted by the reference voltage *vo_ad**, which is generated by a ramp signal that saturates at the desired value, that in this case is the peak value of 325 V. The error coming out from the comparison between the reference voltage signal and its relative real value is then processed by the voltage PI regulator.

The same process happens for the inverter inductor current *il_ad** through the current PI regulator. The **anti-windup** schemes adopted for the regulators are depicted in Figure A.10 and Figure A.11.

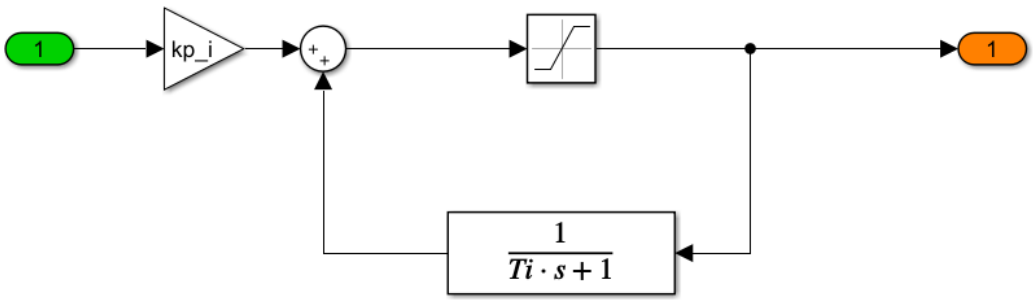

Figure A. 10 – Inner current control loop scheme

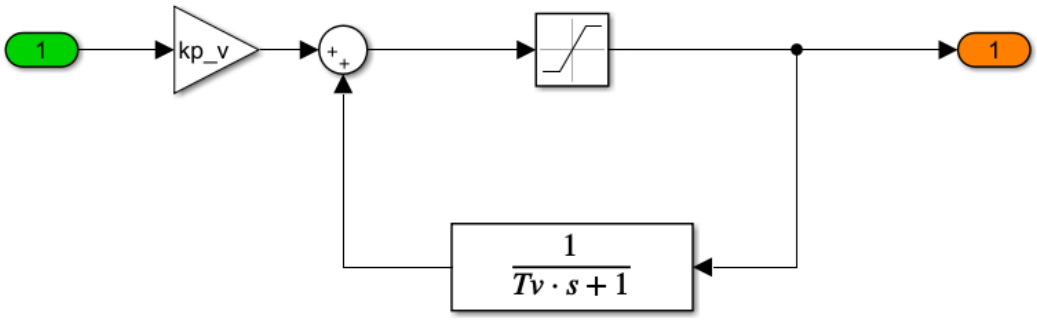

Figure A. 11 – Outer voltage control loop scheme

The green blocks in Figure A.9 contain all the quantities necessary to generate the compensation terms mentioned in Chapter 2 in equation (2.13) and (2.14). Finally, the inverter voltage *e_adref* is obtained. This scheme is the same implemented for the phases *b* and *c*.

The scheme implemented on *q* axes is the same of Figure A.9; the only difference is that the input reference voltage signal for this control loop is zero, for the choice of orientation of the *dq* axis made.

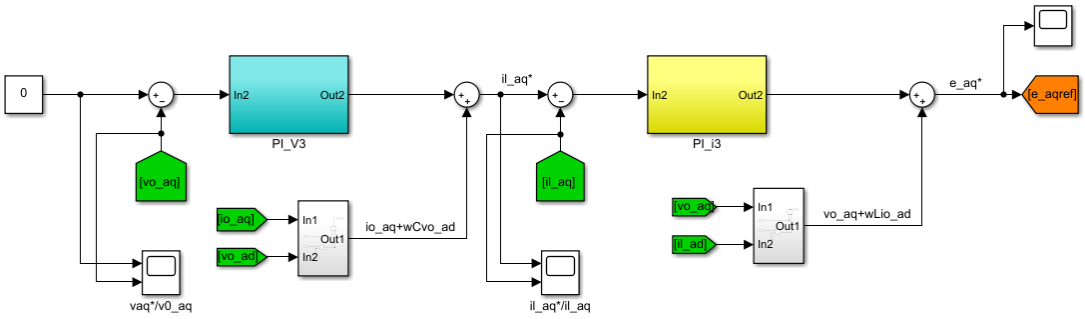

Figure A. 12 – Control loop implemented on *q* axes

At the end, the set of voltages obtained:

- *e_adref, e_bdref, e_cdref*
- *e_aqref, e_bqref, e_cqref*

Is converted back to α and β components through the inverse Park transformation:

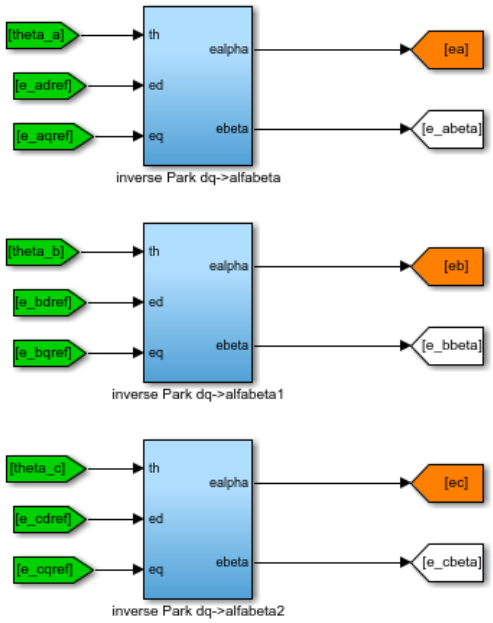

Figure A. 13 – Inverse Park transformation

The β components are discarded, while the α ones, which coincide with the real single-phase quantities, are extracted and sent to the modulation system.

A.4 Modulation System

In the Modulation System the modulation technique that finally generates the control signals for the inverter's operation takes place, that is the **Carrier-based Pulse Width Modulation** explained in paragraph 2.3.

A.4.1 Modulating Signals

As depicted in Figure 2.16, the modulating voltage signals involved in the Carrier-based PWM are generated by adding an **offset voltage** signal to the input voltages (e_{af}, e_{bf}, e_{cf}). Recalling (2.28):

$$\begin{cases} e_{ao} = e_{af} + e_{fo} \\ e_{bo} = e_{bf} + e_{fo} \\ e_{co} = e_{cf} + e_{fo} \end{cases} \quad (2.28)$$

The system was implemented as illustrated below:

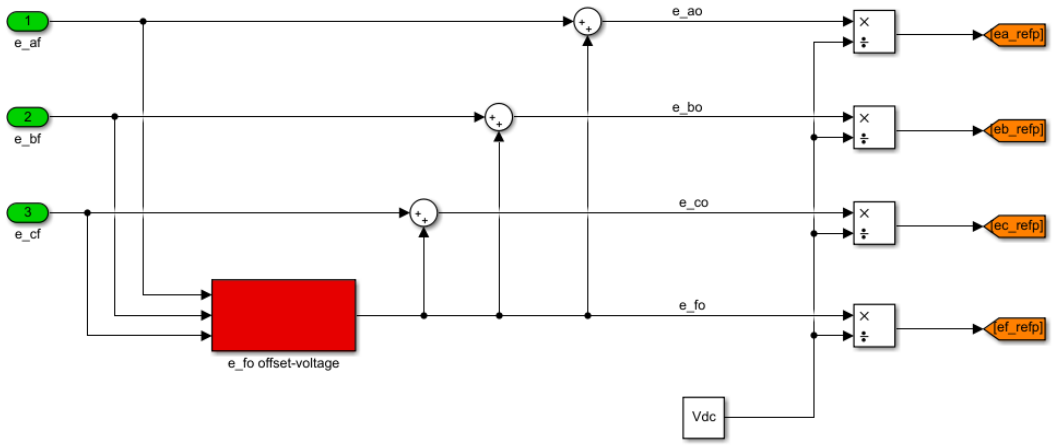

Figure A. 14 – Modulating and offset voltage signals generation

Looking at Figure A.14, it is necessary to note that the modulating and the offset voltage signals are divided by the DC Link voltage V_{DC} in order to operate with per unit quantities during the modulation.

A.4.2 Offset voltage

In the red block there is the algorithm implemented to generate the **offset voltage** e_{fo}, which is the modulating signal for the 4th leg, recalled by (2.30) and reported in Figure A.15:

$$e_{fo} = \begin{cases} -\dfrac{e_{max}}{2} & e_{min} > 0 \\ -\dfrac{e_{min}}{2} & e_{max} < 0 \\ -\dfrac{e_{max} + e_{min}}{2} & Otherwise \end{cases} \quad , \quad That\ is$$

$$e_{fo} = mid\left(-\frac{e_{max}}{2}, \quad -\frac{e_{min}}{2}, \quad -\frac{e_{max} + e_{min}}{2}\right) \qquad (2.30)$$

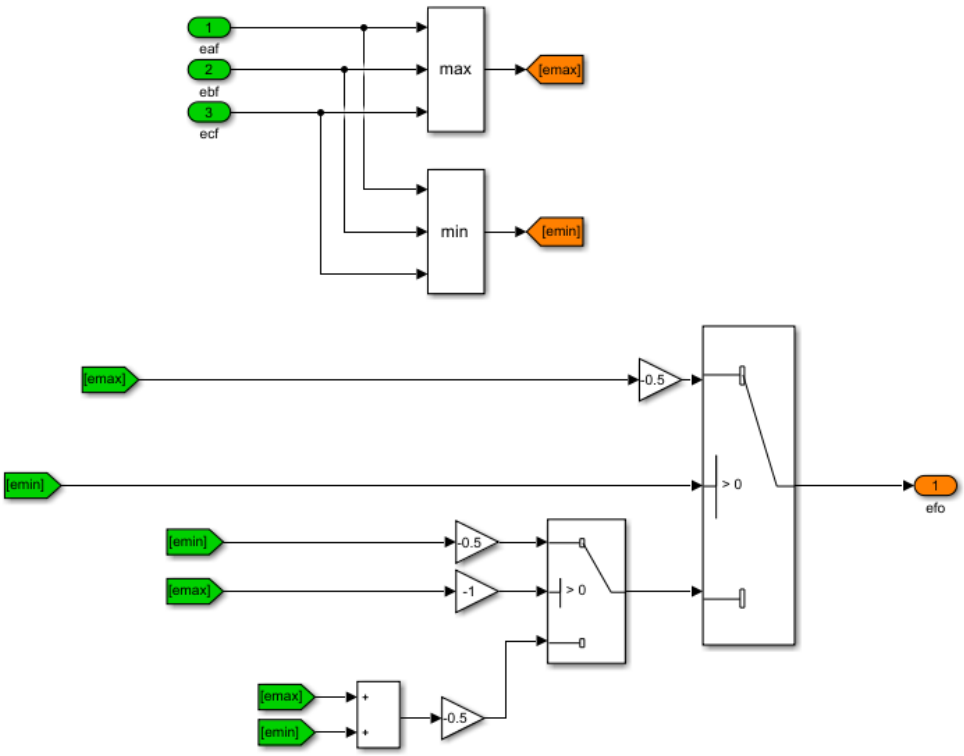

Figure A. 15 – Offset voltage signal calculation

A.4.3 Modulation

Finally, comparing the modulating signals with the carrier triangular signal characterized by a switching frequency $f_{sw} = 10\ kHz$, the control signals for the couple of IGBT for each of the inverter's leg are generated.

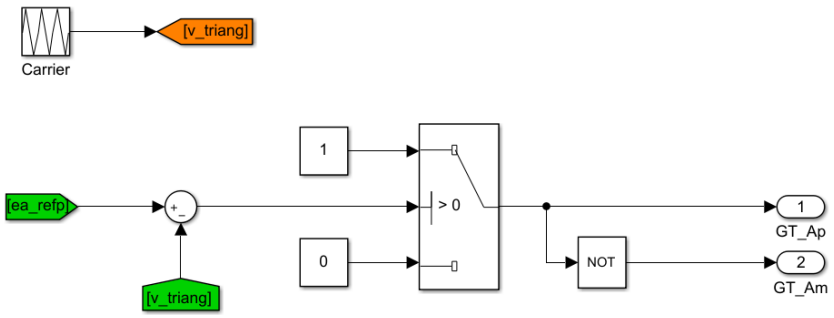

Figure A. 16 – Modulation scheme implemented

The scheme of Figure A.16 is replicated for all the other phases, included the 4th leg.

APPENDIX B
DESIGN OF PI REGULATORS IN MATLAB

In this Appendix the Matlab code for dimensioning the PI controllers as in Chapter 3, section 3.1, is reported.

B.1 Matlab code for SISO system

```
% Design of PI controllers in current and voltage loops

s = tf('s');                                    % complex frequency
Rf=5*3e-3 ; Lf=1e-3 ; Cf=10e-6 ; Rd=0.53;    % (R-)LC filter Rf
[ohm], Lf [H], Cf [F]
fn=50;                          % rated frequency [Hz]
wn=2*pi*fn;                     % rated angular frequency [rad/s]
wfilt=2*pi*5000;                % Butterworth filter frequency [rad/s]

% 1) Current Loop

fsw=10e3;                       % switching frequency
Tsw=1/fsw;
F = 1 / (Rf + s*Lf);            % (R-)L filter transfer function (tf)
Fsw = 1 / (1 + s*Tsw);          % inverter transfer function (tf)


Ffilt = 1 / ( (s/wfilt)^2 + (0.765*s/wfilt) + 1 ) / ( (s/wfilt)^2 +
(1.848*s/wfilt) + 1 );          % Butterworth filter (tf)
GI = Fsw*F*Ffilt;               % tf of the process to be controlled
figure(1);
w = logspace(-1,6,600);         % w varies between 1E-1 and 1E6 rad/s
with 600 points
bode(GI,'b',w);   grid;
title('Transfer function of the process GI(s)');
legend('GI(s)');
```

```
% Design of kpI and kiI as a function of the phase margine phiI

wcI = 2*pi*350;              % cut-off angular frequency
[mag,csi] = bode(GI,wcI);    % gain and phase at wcI
phiI = 10:1:90;              % phase margin [deg]
thetaV = -180 + phiI - csi;
kpI = cos(thetaV*pi/180)/mag; kiI = -wcI*sin(thetaV*pi/180)/mag;
figure(2);
subplot(2,1,1); plot(phiI,kpI); grid; xlabel('phiI [deg]');
ylabel('kpI');
title('kpI [p.u.] and kiI [1/s] with variation of phase phi [deg]');
subplot(2,1,2); plot(phiI,kiI); grid; xlabel('phiI [deg]');
ylabel('kiI');

% Frequency response of the open loop and closed loop transfer
functions

phimI = 60;                  % the phase margin [deg]
[mag,csi] = bode(GI,wcI);    % magnitude and phase of GI at wcI
magdb=20*log10(mag); thetaV = -180 + phimI - csi;
thetaV = -180 + phimI - csi;
kpI = cos(thetaV*pi/180)/mag; kiI = -wcI*sin(pi*thetaV/180)/mag;
PID_I = kpI + kiI/s;         % current PI controller
LI = PID_I*GI;               % open loop transfer function
KI = LI/(1 + LI);            % closed loop transfer function
figure(3);
bode(LI,'b',KI,'r',w); grid;
title('Open loop LI(s) and closed loop KI(s) transfer functions');
legend('LI(s)','KI(s)');


% 2) Voltage Loop

G = (1 + Rd*Cf*s) / (s*Cf); % C filter transfer function
GV = G*KI*Ffilt;             % process to be controlled (KI: current
loop)
figure(4);

w = logspace(-1,6,100);      % w ranges between 1E-1 and 1E6 rad/s,
with 100 points
bode(GV,'b',w); grid;
title('Transfer function of the process GV(s)');

% Design of kpV and kiV with the variation of phase margin phiV

wcV = 2*pi*50;               % cut off frequency [rad/s]
[magV,csv] = bode(GV,wcV);   % amplitude and phase corresponding to
wc
phiV = 10:1:90;              % phase margin [deg]
thetaV = -180 + phiV - csv;
kpV = cos(thetaV*pi/180)/magV; kiV = -wcV*sin(thetaV*pi/180)/magV;
figure(5);
subplot(2,1,1); plot(phiV,kpV); grid; xlabel('phiW [deg]');
ylabel('kpW');
```

```
title('kpW [p.u.] and kiW [1/s] varying with the phase margin phi
[deg]');
subplot(2,1,2); plot(phiV,kiV); grid; xlabel('phiW [deg]');
ylabel('kiW');

% Frequency response of the open loop and closed loop transfer
functions

phimV = 80;                  % the phase margin [deg]
[magV,csv] = bode(GV,wcV);   % magnitude and phase at wcV
magdb=20*log10(magV); thetaV = -180 + phimV - csv;
kpV = cos(thetaV*pi/180)/magV; kiV = -wcV*sin(pi*thetaV/180)/magV;
PID_V = kpV + kiV/s;         % voltage PI controller
LV = PID_V*GV;               % open loop transfer function
KV = LV/(1 + LV);            % closed loop transfer function
figure(6); bode(LV,'b',KV,'r',w); grid;
title('Open loop LV(s) and closed loop KV(s) transfer functions');
legend('LV(s)','KV(s)');
a=1;
```

B.2 Matlab code for MIMO system

```
% Nyquist diagram for MIMO systems  (inner control loop)

eps=0.01;
Rf=5*3e-3 ; Lf=1e-3 ; %filter parameters
fn=50;                  %rated frequency [Hz]
wn=2*pi*fn;
wo=wn;
ksogi=1; %k_sogi
kpI=2.23; % from the tradiotional designing of PI
kiI=646; %       "                    "

w1=linspace(-3000,3000,1001);

    F11=kpI+(((kiI*(i.*w1 + eps))./((i.*w1 + eps).^2+wo^2)));
    F12=(kiI*wo)./((i.*w1 + eps).^2 + (wo^2));
    F21=-F12;
    F22=F11;
    F=[F11,F12;F21,F22]; %PI transfer matrix (alpha/beta axes)

    Tf=1./(Rf + (i.*w1 + eps)*Lf); %filter transfer function

    D=(ksogi*wn*(i.*w1 + eps))./(((i.*w1 + eps).^2) +
((ksogi*wn)*(i.*w1 + eps)) + (wn^2));
    Q=(ksogi*(wn^2))./(((i.*w1 + eps).^2) +( (ksogi*wn)*(i.*w1 +
eps)) + (wn^2));

    SOGI=[D,0;Q,0]; %SOGI transfer matrix;
```

```
    L11=Tf.*D.*F11;
    L12=Tf.*D.*F12;
    L21=Tf.*Q.*F11;
    L22=Tf.*Q.*F12;
    L=[L11,L12;L21,L22];

    lambda1=0.5*(L11+L22) - sqrt((0.25*((L11-L22).^2) +
(L21.*L12))); %eigenvalues of Li
    lambda2=0.5*(L11+L22) + sqrt((0.25*((L11-L22).^2) +
(L21.*L12)));

   figure(1);
    subplot(2,1,1); plot(lambda1,'b'); grid;
    xlabel('Re'); ylabel('Im');
    title('Nyquist curve of lambda_1(jw)');


    subplot(2,1,2); plot(lambda2,'r'); grid;
    xlabel('Re'); ylabel('Im');
    title('Nyquist curve of lambda_2(jw)');


  figure(2);
    plot(1,1); plot(lambda1,'b'); grid;
    hold on
    plot(1,1); plot(lambda2,'r');
    hold on
    plot(1,1); t=0:0.01:2*pi;
    x=cos(t);
    y=sin(t);
    plot(x,y,'g')

    xlabel('Re'); ylabel('Im');
    title('Nyquist curves of lambda_1_,_2(jw)');

    for n=1:length(lambda1)
        num=lambda1(n);
        if real(num)<=0 & imag(num)>=0
            if (real(num))^2 + (imag(num))^2 >=1-0.1 & (real(num))^2
+ (imag(num))^2 <=1+0.1
                phi_m=atan((imag(num))/(abs(real(num))))*180/pi
            end
        end
    end
```

```
% Nyquist diagram for MIMO systems (outer control loop)

eps=0.01;
Rf=5*3e-3 ; Lf=1e-3 ; Rd=0.53; Cf=10e-6; %filter parameters
fn=50; %rated frequency [Hz]
wn=2*pi*fn;
wo=wn;
ksogi=1; %k_sogi
kpI=0.5;
kiI=8.85;
kpV=0.0029;
kiV=0.0634;


for kk=1:1:2000
    ww1=(-1000+kk)*2;
    w(kk)=ww1;
    Fi11=kpI+(((kiI*(i.*ww1 + eps))./((i.*ww1 + eps).^2+wo^2)));
    Fi12=(kiI*wo)./((i.*ww1 + eps).^2 + (wo^2));
    Fi21=-Fi12;
    Fi22=Fi11;
    Fi=[Fi11,Fi12;Fi21,Fi22]; %PIi transfer matrix (alpha/beta axes)

    Tfi=1./(Rf + (i.*ww1 + eps)*Lf); %filter transfer function

    D=(ksogi*wn*(i.*ww1 + eps))./(((i.*ww1 + eps).^2) +
((ksogi*wn)*(i.*ww1 + eps)) + (wn^2));
    Q=(ksogi*(wn^2))./(((i.*ww1 + eps).^2) +( (ksogi*wn)*(i.*ww1 +
eps)) + (wn^2));

    SOGI=[D,0;Q,0]; %SOGI transfer matrix;


    Li11=Tfi.*D.*Fi11;
    Li12=Tfi.*D.*Fi12;
    Li21=Tfi.*Q.*Fi11;
    Li22=Tfi.*Q.*Fi12;
    Li=[Li11,Li12;Li21,Li22]; % open loop transfer matrix

    I=[1,0;0,1];

    Ki=inv(I+Li)*Li; % closed loop transfer matrix
    Ki11=Ki(1,1);
    Ki12=Ki(1,2);
    Ki21=Ki(2,1);
    Ki22=Ki(2,2);

    Tfv=(1+(i.*ww1)*Rd*Cf)./(Cf*(i.*ww1)); %filter transfer function

    Fv11=kpV+(((kiV*(i.*ww1 + eps))./((i.*ww1 + eps).^2+wo^2)));
    Fv12=(kiV*wo)./((i.*ww1 + eps).^2 + (wo^2));
    Fv21=-Fv12;
    Fv22=Fv11;
    Fv=[Fv11,Fv12;Fv21,Fv22]; %PIv transfer matrix (alpha/beta axes)
```

```
    Lv11=Tfv.*(Ki11.*Fv11+Ki12.*Fv21);
    Lv12=Tfv.*(Ki11.*Fv12+Ki12.*Fv22);
    Lv21=Tfv.*(Ki21.*Fv11+Ki22.*Fv21);
    Lv22=Tfv.*(Ki21.*Fv12+Ki21.*Fv22);
    Lv=[Lv11,Lv12;Lv21,Lv22]; % open loop transfer matrix

    lambda3(kk)=0.5*(Lv11+Lv22) - sqrt((0.25*((Lv11-Lv22).^2) +
(Lv21.*Lv12))); %eigenvalues of Lv
    lambda4(kk)=0.5*(Lv11+Lv22) + sqrt((0.25*((Lv11-Lv22).^2) +
(Lv21.*Lv12)));
end

   figure(1);
    subplot(2,1,1); plot(lambda3,'b'); grid;
    xlabel('Re'); ylabel('Im');
    title('Nyquist curve of lambda_3(jw)');

    subplot(2,1,2); plot(lambda4,'r'); grid;
    xlabel('Re'); ylabel('Im');
    title('Nyquist curve of lambda_4(jw)');

    figure(2);
    plot(1,1); plot(lambda3,'b'); grid;
    hold on
    plot(1,1); plot(lambda4,'r');
    hold on
    plot(1,1); t=0:0.01:2*pi;
    x=cos(t);
    y=sin(t);
    plot(x,y,'g')


    xlabel('Re'); ylabel('Im');
    title('Nyquist curves of lambda_3_,_4(jw)');
```

APPENDIX C
SINGULAR VALUES

Definition [19]:
The singular values of the matrix $\Phi \in C^{p,m}$ are the $k = \min(p, m)$ roots of the eigenvalues of $\Phi\Phi^*$ or $\Phi^*\Phi$:

$$\sigma_i(\Phi) \quad := \sqrt{\lambda_i(\Phi\Phi^*)} = \sqrt{\lambda_i(\Phi^*\Phi)}, \quad m = p$$
$$\sigma_i(\Phi) \quad := \sqrt{\lambda_i(\Phi^*\Phi)}, \quad m > p$$
$$\sigma_i(\Phi) \quad := \sqrt{\lambda_i(\Phi\Phi^*)}, \quad m < p$$

where Φ^* is the conjugate matrix of Φ.

Definition [19]:
Any matrix $\Phi \in C^{p,m}$ can be factorized in a decomposition of singular values:

$$\Phi = U\Sigma V^*$$

where matrix $U \in C^{pxp}$ and matrix $V \in C^{mxm}$ are unitary, while matrix Σ is defined as:

$$\Sigma = \begin{bmatrix} \Sigma_1 \\ 0 \end{bmatrix} \in R^{pxm}, \quad p \geq m$$
$$\Sigma = [\Sigma_1 \quad 0] \in R^{pxm}, \quad p \leq m$$

with:

$$\Sigma_1 = diag\{\sigma_1, \sigma_2, \dots, \sigma_k\}; \quad k = \min(p, m)$$

and

$$\overline{\sigma} \equiv \sigma_1 \geq \sigma_2 \geq \cdots \geq \sigma_k \equiv \underline{\sigma}$$

Definition [19]:
Defining:

$$b = tr(\Phi^*\Phi) = \sum_{i,j} |\varphi_{i,j}|^2$$

$$c = \det(\Phi^*\Phi) = \det(\Phi)^2$$

The sum of the eigenvalues of $\Phi^*\Phi$ is $b = \lambda_1 + \lambda_2$ while the product is $c = \lambda_1\lambda_2$.
Since:

$$\sigma_i(\Phi) \quad := \sqrt{\lambda_i(\Phi^*\Phi)}$$

It results that:

$$\overline{\sigma}(\Phi) = \sqrt{\frac{b + \sqrt{b^2 - 4c}}{2}}$$

$$\underline{\sigma}(\Phi) = \sqrt{\frac{b - \sqrt{b^2 - 4c}}{2}}$$

The MATLAB code implemented for the evaluation of the singular values is reported below:

```
% singular values

eps=0.01;
Rf=5*3e-3 ; Lf=1e-3 ; %filter parameters
fn=50; %rated frequency [Hz]
wn=2*pi*fn;
wo=wn;
ksogi=1; %k_sogi
kpI=0.5;
kiI=8.85;
```

```
for kk=1:1:10000
    ww1=kk*2;
    w(kk)=ww1;
    F11=kpI+(((kiI*(i.*ww1 + eps))./((i.*ww1 + eps).^2+wo^2)));
    F12=(kiI*wo)./((i.*ww1 + eps).^2 + (wo^2));
    F21=-F12;
    F22=F11;
    F=[F11,F12;F21,F22]; %PIi transfer matrix (alpha/beta axes)

    Tf=1./(Rf + (i.*ww1 + eps)*Lf); %filter transfer function

    D=(ksogi*wn*(i.*ww1 + eps))./(((i.*ww1 + eps).^2) +
((ksogi*wn)*(i.*ww1 + eps)) + (wn^2));
    Q=(ksogi*(wn^2))./(((i.*ww1 + eps).^2) +( (ksogi*wn)*(i.*ww1 +
eps)) + (wn^2));

    SOGI=[D,0;Q,0]; %SOGI transfer matrix;


    L11=Tf.*D.*F11;
    L12=Tf.*D.*F12;
    L21=Tf.*Q.*F11;
    L22=Tf.*Q.*F12;
    L=[L11,L12;L21,L22]; % open loop transfer matrix


    b=abs(L11.^2)+ abs(L12.^2)+ abs(L21.^2)+ abs(L22.^2);

    Ltc=(L');
    c=det(Ltc*L);

    sigma1=sqrt(0.5*(b+sqrt(b.^2 -4*c))); % singular values
    sigma2=sqrt(0.5*(b-sqrt(b.^2 -4*c)));
    s1(kk)=abs(sigma1);
    s2(kk)=abs(sigma2);

   end

    s1dB=20*log10(s1);
    s2dB=20*log10(s2);

    figure(1);
    plot(w,s1dB,'b'); grid;

     xlabel('Frequency (rad/s)'); ylabel('Magnitude (dB)');
    title('sigma_1');

   figure(2);
    plot(w,s2dB,'r'); grid;

     xlabel('Frequency (rad/s)'); ylabel('Magnitude (dB)');
    title('sigma_2');
```